


Doctoral Dissertation
Doctoral Program in Metrology (30.th cycle)

Realization of advanced ^{171}Yb optical lattice frequency standard

Gianmaria Milani

* * * * * *

Supervisors
Dr. Davide Calonico, Istituto Nazionale di Ricerca Metrologica, Supervisor
Ing. Giovanni A. Costanzo, Politecnico di Torino, Co-Supervisor

Doctoral Examination Committee:
Dr. Gianluca Galzerano, Referee, Politecnico di Milano and Istituto di Fotonica e Nanotecnologie
Dr. Rachel Godun, Referee, National Physical Laboratory
Dr. Massimo Ortolano, Politecnico di Torino
Ing. Giovanni A. Costanzo, Politecnico di Torino
Prof. Elena Botta, Università di Torino

Politecnico di Torino
02/05/2018

I hereby declare that, the contents and organisation of this dissertation constitute my own original work and does not compromise in any way the rights of third parties, including those relating to the security of personal data.

.....

Gianmaria Milani
Turin, 02/05/2018

Summary

Atomic clocks constitute a fundamental tool for time and frequency metrology and their application is widespread in many technological fields. In particular, the International System of units (SI) defines the second on a microwave transition of Caesium atoms. The realization is made by clocks reaching uncertainties of few parts in 10^{-16}, making the second to be the quantity realized with the smallest uncertainty in the SI. However, a new generation of atomic clocks, called optical clocks, have already demonstrated to surpass Caesium standards both in accuracy and stability.

The research performed during my PhD activity has been focused on the development and characterization of Ytterbium (Yb) optical lattice clocks. These systems operate with a large number of ultra-cold neutral atoms having a clock transition in the visible region of the electromagnetic spectrum. The atomic sample is trapped in an periodical optical potential called optical lattice that gives the advantage to interrogate many quantum absorbers for an extended time, with small perturbations, allowing to achieve an unprecedented stability and accuracy.

The main experimental work has been carried out in the laboratories of the Istituto Nazionale di Ricerca Metrologica (INRIM) in Turin, where several atomic clocks are present including the Italian primary frequency standard, the Caesium fountain ITCsF2, and where an Yb optical lattice clock is currently being developed. This thesis describes the functioning of the system along with the full characterization of systematic effects, the complete uncertainty budget and its first absolute frequency measurement against the primary frequency standard. The clock exhibited an accuracy of 1.6×10^{-16} and the comparison with the Cs fountain resulted in a frequency of $f_{^{171}\mathrm{Yb}} = 518\,295\,836\,590\,863.59(31)\,\mathrm{Hz}$, limited by the fountain uncertainty. This measurement is in agreement with the ytterbium frequency recommended as a secondary representation of the second in the SI and constitutes the first measurement of a Yb clock in Europe and the second one in the world against a primary frequency standard.

Several upgrades have been applied after the absolute measurement. In particular, the design and realization a system capable to frequency stabilize several lasers on a single optical cavity is illustrated. This cavity has been implemented to lock the lasers used to cool and trap the atomic sample at 399, 556 and 759 nm using

the offset sideband locking technique, a modified version of the Pound–Drever–Hall method that gives an extended frequency tunability. The system proved to be an easy-to-use and reliable tool for the experimental activity showing a linewidth below 300 Hz at 556 nm, which is the wavelength that requires the most stringent performance, and a long term drift below 20 kHz per day at 759 nm. That is suitable for operating the lattice laser with a light shift uncertainty below 1×10^{-18}.

During my PhD I have been guest researcher at the National Institute of Standards and Technology (NIST) of Boulder, Colorado, for nine months in 2016. In these laboratories two Yb optical lattice clocks are operative. I worked on the instability measurement of a composite system exploiting the two clocks to suppress the Dick effect, called zero-dead-time (ZDT) clock, which demonstrated a fractional instability of 3×10^{-17} at 1 s. The two clocks can also be operated to extend the interrogation time obtaining a spectroscopic feature after 4 s of 120(20) mHz corresponding to a quality factor $Q > 4 \times 10^{15}$. I also worked on the characterization of several systematic shifts that allowed to complete the uncertainty budget of the clocks at 1.6×10^{-18}. In particular, I contributed to the characterization of lattice light shifts considering the effect of atomic sample temperature and the identification of a metrological regime called operational magic frequency where frequency shifts are insensitive to changes in trap depth.

Acknowledgements

I warmly thank all the INRIM folks for the guide, the help, the suggestions and the support you gave me. It has been a pleasure working with all of you: Davide, Filippo, Giovanni, Salvatore, Alberto, Elio, Marco, Pierre, Cecilia, Matteo, Claudio and Marco.

Thanks to my PhD mates whith whom I shared many scientific and burocratic issues: Giacomo, Benjamin, Filippo, Anna, Piero, Michele, Matteo, Carolina and Carmen.

I would also like to express my sincere thanks to the NIST guys for welcoming me in Boulder, such a great place to work and live: Chris Oates, Andrew Ludlow, Richard Fox, Will McGrew, Roger Brown, Daniele Nicolodi, Kyle Beloy, Marco Schioppo, Jeff Sherman, Robbie Fasano, Nathan Hinkley, Holly Leopardi and Judith Olson.

Empty your mind
be formless, shapeless
like water

B. Lee

Contents

List of Tables

List of Figures

Chapter 1

Introduction

Since antiquity, the measurement of time has always been a fundamental matter for the human being. The observation of the sun position during the day or the stars position in the night sky as well as the course of the seasons were indeed a first approach adopted by ancient peoples to quantify the passing of time. This knowledge was helpful to make decisions and predictions about agriculture and many aspects of everyday life. Historical fundamental progresses, either civil, scientific or military, were made possible thanks to a better measurement of time. The prediction of Nile floods, the precise measurement of the longitude during navigation or the synchronization of trains are only few examples of that. Under the spur of this increasing demand of "precision", instruments used to measure time, namely the clocks, became more and more sophisticated: from the first sundials to the hourglasses, from the mechanical clocks to quartz oscillators and then to the ultimate atomic clocks. Nowadays the precise and reliable time measurement plays a fundamental role both in science and technology as well as civil society and defence.

The importance of precise measurements resulted in the constitution of international agreements about common definitions of the fundamental and derived unit of measurement that then gave birth to to the International System of Units (or SI). The agency designated to maintain the SI is the International Bureau of Weights and Measures (BIPM), constituted in 1875 after the sign of the Metre Convention and is located in Sèvres, France.

1.1 Time and frequency metrology and the definition of the second

Time and frequency metrology is the science that studies the definition and the measurement of the unit of time (the second), the realization of the international timescale, the dissemination and comparison of different realizations of the

standard. Historically, the second has been measured by means of astronomical arguments and its first definition was a fraction (1/86 400) of the Earth mean solar day. At the end of XIX century, the fluctuation and increment of the Earth's period of rotation became a scientific evidence and, as a consequence, the definition was no longer satisfactory. A new definition based on the motion of the Earth on its orbit around the Sun (*tropical year*) came along and was adopted in 1960. This, however, was found to be quite cumbersome to realize as well as difficult to disseminate given its annual periodicity. At the time of this redefinition scientists had already demonstrated that an atomic standard of frequency, based on a transition between two energy levels of an atoms or a molecule, could be realized.

1.2 Atomic clocks

The basic concept behind the realization of atomic clocks comes from the fundamental principles of quantum mechanics [1] namely that electrons in an atom can assume only certain, discrete, energy levels. These levels, apart from external perturbations, are universally determined by quantum mechanics equations and fundamental constants, which are considered valid in the entire universe. The intrinsic properties of the atomic structure, together with the universality assumed here, make 'the atoms' a better reference for the definition of the second than the Earth motion.

Following quantum mechanics arguments, the electron transition between two energy levels E_1 and E_2 causes the exchange of a photon of frequency $\nu_0 = |E_2 - E_1|/h$, where h is the Plank constant. The transition, or resonance, can be driven providing the atom a radiation at the frequency of the atomic transition ν_0. This oscillation constitutes a convenient basis to define the second as number of periods of a certain reference transition frequency called clock transition. The first atomic clock saw the light in 1955 by Essen and Parry [2]. It consisted in a device where a microwave oscillator (also called local oscillator) is used to probe the hyper-fine transition between the two ground state levels of ^{133}Cs atoms. The frequency of this oscillator is tuned to match the atomic transition of interest and is kept on resonance using a feedback loop. The result is a frequency standard where the intrinsic stability of the atom sample is transferred to a microwave radiation. In other words, an intrinsic quantum property is picked up by a macroscopic object, the oscillator.

Different atomic species were used to realize atomic clocks like, for example, caesium $\left(^{133}\mathrm{Cs}\right)$, rubidium $\left(^{87}\mathrm{Rb}\right)$ and thallium $\left(^{205}\mathrm{Tl}\right)$. The frequency of the Cs transition was measured with respect of the ephemeris time in 1958 [3] resulting in $\nu_0 = 9\,192\,631\,770(20)\,\mathrm{Hz}$. It was in 1967 that the International System of Units (SI) [4] defined the second in terms of an atomic property, more precisely it is equal to the duration of 9 192 631 770 periods of the ground state hyperfine transition

of ^{133}Cs. This definition of the second is still valid today and it is realized by the caesium microwave frequency standards which measure this transition in continuity with the measurement done in 1958.

To quantify the clock performances, two estimators, or figures of merit, are used: *accuracy* and *instability*. Accuracy quantifies the deviation of the frequency realized by the standard from the nominal value given by unperturbed atoms. In fact, the energy levels, therefore the transition frequency, are perturbed by many environmental effects like, for instance, their motion (Doppler effect), collisions, electric and magnetic fields or relativistic effects (second order Doppler effects). In a frequency standard these effects have to be well controlled and quantified with a related uncertainty. This characterization is usually reported in the so called *uncertainty budget* (see chap. 5.3), a table which summarizes each effect with its corresponding uncertainty and the final total value. It worth mention that, because of systematic effects, the definition of the second was updated in 1990 considering atoms at rest at a temperature of 0 K.

Instability, on the other hand, quantifies the dispersion of frequency around the mean value realized by the frequency standard over the measurement time. It is a statistical quantity and it is commonly evaluated using the Allan Deviation (or two-samples deviation) [5] that expresses a statistical uncertainty as a function of the measurement (averaging) time. The instability also limits the accuracy determination as it is not possible to resolve a frequency shift smaller than the statistical uncertainty of the frequency measure.

In general[1], an atomic clock operates preparing the atomic sample in the proper quantum state for the spectroscopic interrogation, $|1\rangle$. After the interrogation, made by the clock radiation, atoms can be either excited to the level $|2\rangle$ or not depending on the frequency of the local oscillator with respect to the atomic transition. By counting the number of excited atoms, the excitation fraction is extracted and it is used to tune the clock radiation frequency and keep in on resonance. The fundamental limit of this approach comes from the inherent quantum nature of the system. Considering a linear superposition between the two states:

$$|\psi\rangle = \alpha\,|1\rangle + \beta\,|2\rangle \tag{1.1}$$

having α and β complex numbers such that $|\alpha|^2 + |\beta|^2 = 1$. When α and β are diverse from 0, the outcome of a measure on this system is uncertain, resulting in the collapse of the wave function either in the state $|1\rangle$ with a probability $p_1 = |\alpha|^2$ or in $|2\rangle$ with a probability $p_2 = |\beta|^2$. In the same way, atoms interacting with the probing radiation can be excited or not depending only by the statistical quantum nature of the system, which eventually results in a fluctuation on the signal collected from the atoms. This effect is called quantum projection noise

[1] Assuming a simple two level atom.

(QPN) [6] and constitutes the fundamental limit to the instability of an atomic frequency standard. The basic formulation of fractional frequency instability for an atomic clock, without any additional noise but the QPN, can be expressed as [7]:

$$\sigma_y(\tau) = \frac{\Delta\nu}{\nu_0}\frac{\eta}{S/N\sqrt{\tau}} = \frac{1}{Q}\frac{\eta}{S/N\sqrt{\tau}} \tag{1.2}$$

with τ being the averaging time and η is a parameter close to 1 which depends on the spectroscopic technique adopted. The main parameters affecting instability are the spectroscopic line quality factor $Q = \frac{\nu_0}{\Delta\nu}$ and the signal-to-noise ratio S/N. Intuitively increasing Q means having a narrower transition or a higher frequency transition while S/N increasing the number of atoms probed.

The first generation of atomic clocks were based on a thermal atomic beam passing through a microwave cavity for the interrogation whose duration sets the linewidth of the measured spectroscopic feature, as described by the Rabi method [8]. Increasing the interrogation time requires the construction of larger cavities which brings in many technical complications. A convenient spectroscopic technique was introduced by Ramsey in 1950 [9] then awarded by the Nobel Prize in Physics in 1989, which consists in two short microwave interactions separated by a free evolution time T (or dark time), where atoms travel from one cavity to the other and are not illuminated. The resulting linewidth scales as $\Delta\nu = 1/T$. This allowed to increase the interrogation time reaching an instability of about 5×10^{-15} at 12 hours of integration time and an accuracy of few parts in 10^{15} for caesium standards [10].

After this generation different type of clocks were introduced like the hydrogen maser [11] or atomic cell standards [12], where the atomic sample (commonly alkali metal such as ^{87}Rb) consists in a gas contained in a glass sealed container and probed by microwaves. The next major step toward a better realization of the second was the discover of laser cooling by Chu, Choen-Tannoudji and Phillips in 1995 [8], for which they won the Nobel Prize in Physics in 1997. This mechanism permits to slow the atoms down to velocities of few cm/s, that can be related to a temperature of few µK, thus further extending the interaction time as well as significantly suppressing Doppler effects. This brought the invention of a completely new device called atomic fountain, in which the atoms are cooled and trapped using laser beams to form ultra-cold atomic aggregates at a temperature of the order of 1 µK. These cold atoms ensembles are launched vertically passing twice through the same microwave cavity, once on the way up and then when they fall down under the gravity action, thus realizing a Ramsey interrogation. The latest version of cryogenic caesium fountains reached an accuracy of $\sim 1 \times 10^{-16}$ of and an instability of about $\sigma_y = 1 \times 10^{-13}/\sqrt{\tau/\mathrm{s}}$ [13] and are the current primary frequency standard for the realization of the second.

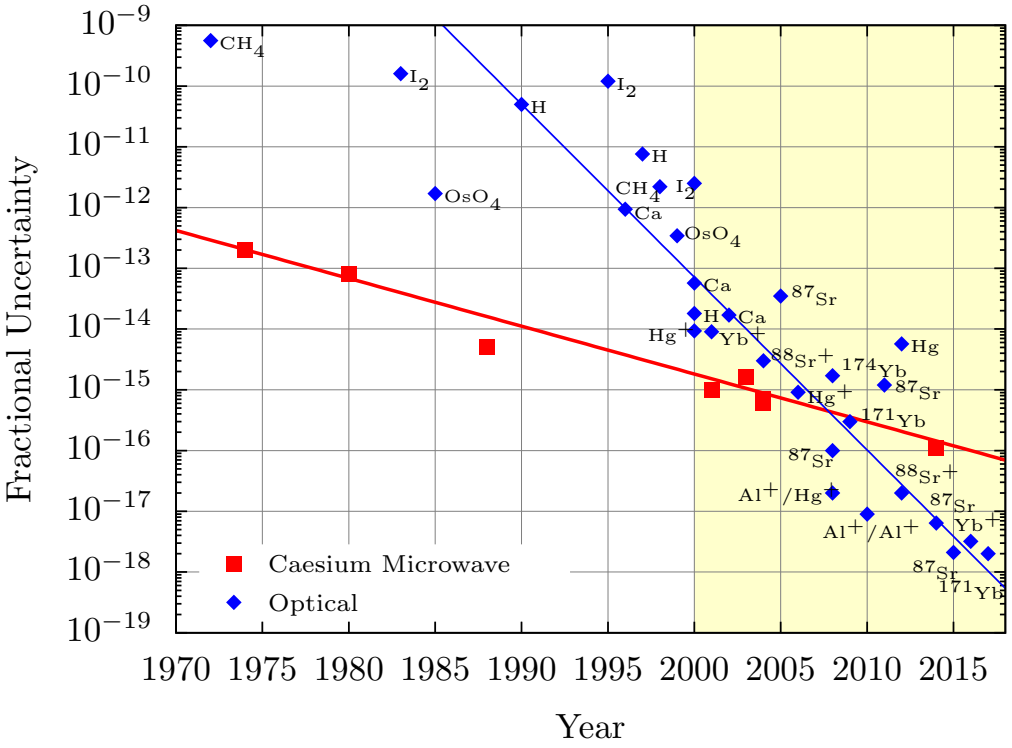

Figure 1.1: Fractional uncertainty of microwave and optical clocks over the years. The yellow shaded region expresses the introduction of optical frequency comb

1.3 Optical frequency standards and the optical frequency comb

So far we introduced atomic clocks based on a reference transition with frequency in the microwave domain ($\sim 10^{10}$ Hz). According to eq.(1.2), moving toward higher transition frequency leads to a better instability. This pushed the research on frequency standards having a clock transition frequency in the visible region of the electromagnetic spectrum ($\sim 5 \times 10^{14}$ Hz). Intuitively, higher frequency means a finer division of the time unit, like measuring a length using a ruler with a mm scale rather than a cm scale. Researchers started to develop such devices during the 1980s, after the spread of lasers, invented in 1960, which constitute the local oscillator for these frequency standard.

The fist realization of optical clocks were based on a laser stabilized on atomic or molecular transition like methane (CH_4) or iodine (I_2). The research on optical clocks gained a strong momentum during the second half of 1990s after the development of atomic manipulation techniques like laser cooling and trapping, together with the improvement of laser sources and non linear optics to generate lasers with frequency not directly available. Two principal approaches arose: optical clocks

based on single trapped ions and optical clocks using many neutral atoms trapped in an optical lattice. Both methods shares the idea to suppress Doppler and recoil shifts by tightly trapping the atoms for an extended time, allowing, also, a long interrogation of the sample which results in high precision spectroscopy.

The former type exploits the forbidden optical transition of single ions which can be trapped and cooled using electric fields (both static and oscillating) and laser radiations. The simplicity of the quantum systems gives the advantage of an accurate manipulation and control the ion that, therefore, can be interrogated continuously for extended periods keeping systematic effects under control and providing very good accuracy. On the other hand, the signal-to noise ratio, and hence the instability, is lower compared to the neutral atoms counterpart as lower is the number of quantum absorber involved in the measurement. Ion clocks have been realized by many research institutes using different atomic species like Yb^+ [14], Sr^+ [15], Al^+ [16], Hg^+ [17]. The best reported fractional accuracies of these type of clocks are about few parts in 10^{-18} and a fractional instability of $5 \times 10^{-15}/\sqrt{\tau/\mathrm{s}}$ [14]. The development of these systems brought two Nobel prizes in Physics, one to Wolfgang Paul and Hans Dehmelt in 1989 for the advances in Ion traps [18] and a second one to David Wineland in 2012 for his work on individual quantum systems [19].

Unlike ions, neutral atoms can not be trapped using electric fields without modifying the electronic structure. This require the implementation of a different confinement technique, based on the dipole force exerted on the atoms by a non-uniform light field (AC Stark effect), where the atoms are trapped inside an optical potential called *optical lattice*. In this way many atoms can be trapped at the same time for an extended period, enhancing the signal coming from the atomic sample and improving the clock stability. The optical lattice consists in a periodical potential made by making interfere different laser beams in order to generate a standing wave. The interference can be designed to have a trapping potential either along a single axis (1D) or multiple dimensions (2D-3D). As already mentioned, the tight confinement 'freezes' the atomic motion along the lattice direction, thus Doppler and recoil effects are strongly suppressed. Moreover, the long lifetime of the trapped atoms permits an extended interrogation of the sample giving a high transition quality factor. Besides the confinement, the optical lattice light field induces also a strong perturbation in the atomic levels. By tuning the frequency of the lattice laser at the *magic frequency* [20] this effect can be suppressed leaving an unperturbed clock transition (at first order). Optical frequency standards currently operating worldwide are based on different alkaline-earth(-like) atomic species: strontium, ytterbium, mercury and magnesium. The best performances reported so far for optical lattice clock are accuracy of few parts in 10^{-18} (presented by NIST at EFTF-IFCS 2017) and instability of $6 \times 10^{-17}/\sqrt{\tau/\mathrm{s}}$ in the case of zero-dead-time clock [21].

Optical frequency measurements Microwaves can be generated and measured by electronic devices. On the contrary, the absolute frequency measurement of an optical radiation is not straightforward as the electronics is not fast enough to count a THz oscillation. Starting from 1970, measurements were done by means of complex frequency chains capable to fill the frequency gap [22, 23]. These devices were based on a combination of several intermediate transfer oscillators that generated a progressively higher frequency, always related to the reference microwave that, in turn, was referenced to the primary frequency standard. The chain necessitate to be designed for a certain limited frequency range and its complexity required many to operate and maintain the system.

Optical frequency measurements were revolutionized by the invention of the *optical frequency comb* in the late 1990s that also worth the Nobel prize in physics to J. L. Hall and T. W. Hänsh in 2006 [24]. In this kind of devices a pulsed laser generates a train of short wave-packets that, in the frequency domain, correspond to a series of discrete sharp lines (or 'teeth') spaced evenly. The frequency of the N^{th} line follows a well defined relation:

$$f_N = N f_{\text{R}} + f_{\text{o}} \tag{1.3}$$

where N indicates the tooth number, f_{R} is the repetition rate of the laser pulse which regulates the separation among the comb lines and f_{o} is the offset frequency. Both f_{R} and f_{o} are radiofrequency and can be easily referenced to a primary frequency standard. An absolute optical frequency measurement can be promptly done by measuring three radiofrequencies namely f_{o}, f_{R} and the beatnote among the radiation under test and the closest comb tooth. In practice, the comb spectrum can be thought as a tunable frequency ruler in the optical domain linked to radiofrequency quantities that are easy to measure.

1.4 Ytterbium optical lattice clock

Among the others alkaline-heart(-like) atoms, Ytterbium emerged as an ideal tool for optical lattice clocks. It has atomic number $Z = 70$ and offers seven stable isotopes, both bosonic and fermionic, that can be used to make different physics experiments. The most external electronic shell contains two electrons that can be arranged in singlet ($S = 0$, where S is the total spin quantum number) and triplet states ($S = 1$). The electronic structure and the relevant atomic transitions are reported in figure 1.2 using the spectroscopic notation $^{2\text{S}+1}\text{L}_{\text{J}}$ where L is the orbital quantum number and J is the total angular momentum.

In a pure fine-structure description a dipole transition from a singlet to a triplet state would be completely forbidden as the spin changes, making lifetimes of the $^3\text{P}_j$ triplet extremely long and vanishingly small transition linewidths. This is even more emphasized in the case of the metastable $^3\text{P}_0$ state for which an electronic

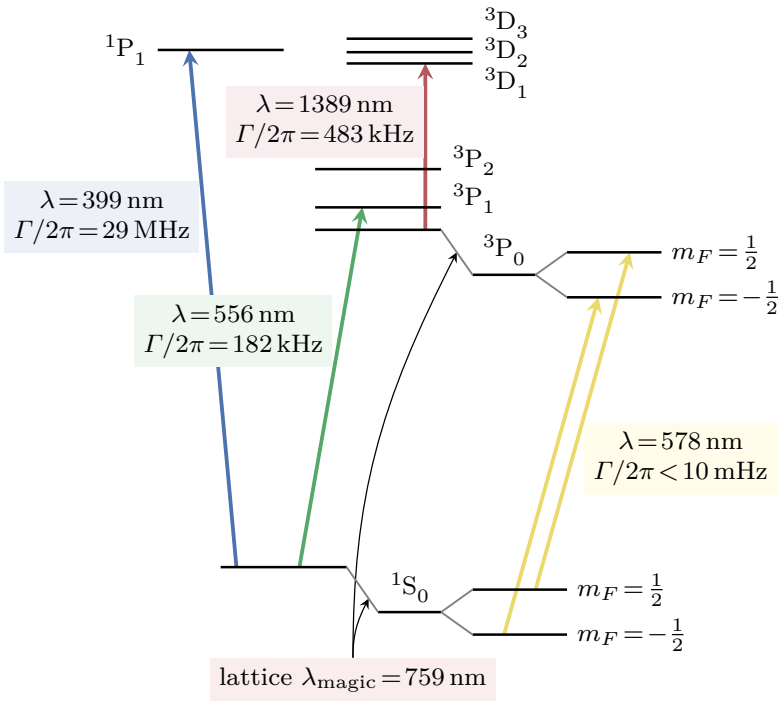

Figure 1.2: Relevant energy levels for ^{171}Yb including the hyperfine splitting of the clock transition. From [25].

dipole transition from the ground state (^{1}S$_0$) would be double forbidden as $\Delta S = 1$ and $J = 0 \rightarrow J = 0$.

Of particular interest, in the case of optical clocks, is the fermionic isotope ^{171}Yb which has a nuclear spin $I = 1/2$ that provides a hyperfine structure (see fig. 1.2). The hyperfine mixing of the ^{3}P$_0$ state with ^{1}P$_1$ and ^{3}P$_1$ states quenches the lifetime in the excited state yelding to ultra narrow, non zero and laser accessible transition at 578 nm (yellow region of the visible spectrum) with a linewidth of about 10 mHz [26]. The narrow linewidth together with its low sensitivity to external perturbations poses the ^{1}S$_0 \rightarrow {}^3$P$_0$ as the natural choice for the clock transition.

However, the optical lattice demands atomic samples with temperature below its trap depth, typically at the level of tens of micro kelvin. With Yb laser cooling techniques are quite straightforward to implement using two auxiliary atomic transitions. These are a strong ^{1}S$_0 \rightarrow {}^1$P$_1$ dipole transition at 399 nm (violet-near UV region), 29 MHz wide, and the inter-combination line ^{1}S$_0 \rightarrow {}^3$P$_1$ at 556 nm (green) with 182 kHz of linewidth. Experimentally, atoms are slowed and trapped in a two stage magneto optical trap (MOT, see next chapter) reaching temperatures of tens of microkelvin. On the top of that, ^{171}Yb exhibits a magic wavelength (see next chapter) at 759 nm [26] and a transition at 1389 nm which is used to move atoms from the metastable ^{3}P$_0$ state to the ground state during the detection phase.

Several optical lattice clocks based on Ytterbium atoms have been developed in different national metrological institutes like the National Institute of Standards and Technology (NIST) [27, 21] in USA, the National Metrological Institute of Japan (NMIJ-AIST) and RIKEN in Japan [28], the Korea Research Institute of Standards and Science (KRISS) [29] and the Istituto Nazionale di Ricerca Metrologica (INRIM) [25].

Currently, the unperturbed clock transition of ^{171}Yb has been considered by the CIPM as a secondary representation of the SI second with a recommended frequency of 518 295 836 590 864.0 Hz with a relative standard uncertainty of 2×10^{-15} [30] (2015).

1.5 Applications

As we have seen so far, optical clocks have demonstrated their capability to perform measurements with a fractional uncertainty of few parts in 10^{-18}. This remarkable performances make their use appealing in many different contexts, opening the doors to innovative scientific and metrological perspectives.

By means of precise time measurements is possible to test General Relativity [31]. In particular, these tests can be carried out in the Earth's gravitational field, looking for deviation from the geoid theory (*Relativistic Geodesy*), by making remote clock comparisons. The gravitational red-shift caused by tens of centimetre height difference is at the level of $\sim 10^{-17}$ and can be resolved by the best optical lattice clocks in few minutes of measurements. This offers an appealing alternative to the classical levelling methods based on terrestrial and satellite techniques that lead to discrepancies at the decimetre level [32].

Optical clocks can be used to test theories beyond the Standard Model of particle physics by measuring the variation of fundamental constants over time [33] or perform fundamental physics measurements at low energy regime [34].

High precision timekeeping can be useful to synchronize radio telescope arrays for very-long-baseline interferometry experiment as well as for global navigation system (GNSS) [35, 36].

Finally, from the metrological point of view, optical lattice clocks are considered as candidates for the future redefinition of the SI second. In fact, currently their performances surpass the Cs primary frequency standards which realizes the definition of the second [25, 37]. The *Comité international des poids et mesures* (CIPM), which is the BIPM committee devoted to assure uniformity among the realizations of units of measurement worldwide, recognized several optical transition as secondary representation of the second.

1.6 Thesis overview

The work presented in this dissertation deals with the development and the characterization of optical frequency standards based on ytterbium (^{171}Yb) atoms. The main part of the experimental work has been carried out in the laboratories of the Time and Frequency division of the Istituto Nazionale di Ricerca Metrologica (INRIM) in Turin. Part of my PhD was spent at the National Institute of Standards and Technology (NIST) in Boulder Colorado, where I contributed to the characterization of an ensemble of two Yb clocks as well as to perform instability measurement. The thesis is arranged as follows.

In chapter 2 are reported the fundamental physical principles regulating the interaction between light and matter used to manipulate the atoms for operate the optical lattice clock along with the details of the spectroscopy techniques and the fundamental aspects of ultra stable lasers and optical cavities .

The experimental details of the INRIM Yb clock are in chapter 3 together with the generation of the lasers used in the experiment as well as the description of the ultra-stable cavity used to stabilize the clock laser.

The description of a new system designed to stabilize many lasers at the same time, the multi wavelength cavity, is in chapter 4. The details of the characterization of the INRIM Yb clock as well as the absolute frequency measurement of the Yb clock transition are given in chapter 5.

The description of the two optical lattice clock present at NIST, the details of the characterization of some systematic effects and the results of the instability measurement done with the zero-dead-time clock are in chapter 6.

Chapter 2

Fundamental principles behind the realization of Yb optical lattice clock

The design of an optical lattice clock is founded on two main elements namely the realization of high resolution spectroscopy and the use of a large ensemble of atoms. Atomic motion, and its induced Doppler effect, represents the major disturbance when measuring an atomic transition. The use of cold atoms trapped in an optical lattice [20] makes possible the simultaneous interrogation of a large number of quantum absorbers for an extended period of time. The tight trapping strongly suppresses Doppler and recoil shifts leading to an ultra-high resolution spectroscopy of the clock transition while the large number of quantum absorbers gives a high signal-to-noise ratio thus improving stability and accuracy of the standard. The induced lattice light shift on the spectroscopic feature are strongly suppressed by tuning the lattice at the so called *magic frequency*, where the perturbation is equal on both ground and exited state of the clock resonance, thus leaving an unperturbed clock transition (at the first order).

Nevertheless, several experimental steps are necessary to bring atoms in the lattice and they all involve the use of coherent light. Atomic manipulation is necessary to cool and trap atoms, prepare them in the right quantum state, probe the clock transition and detect the outcome of the measurement. In this chapter the atomic cooling and trapping techniques are presented in the first part while the second part is dedicated to the optical lattice along with the induced light shifts.

The light source that probes the atomic sample, the local oscillator, plays a key role in the performance achieved by the standard. The use of an ultra-stable laser is necessary to measure narrow transitions such as the double forbidden $^1S_0$ – $^3P_0$ clock transition in Yb. To stabilize the frequency of laser sources the intrinsic mechanical stability of an artefact is typically exploited. This is implemented by the use of ultra-stable optical cavities. Spectroscopy techniques are reported in section

2.4 then, afterwards, the fundamental principles on the realization of ultra-stable lasers are given. In the last section the limits of the clock stability are described.

2.1 Laser cooling and trapping

The optical lattice can trap several neutral atoms only with a kinetic energy below a certain threshold set by the trap depth. Sample atoms, typically provided by a hot atomic beam, are at a temperature (or speed) much higher than the typical threshold (some tens of microkelvin) and thus need to be cooled down to few hundreds of microkelvin. This is accomplished by a careful designed interaction with coherent light.

Examining the interaction between a two-level atom, with a resonance frequency ω_0, and a monochromatic plane wave light field $\vec{E_0}$, the strength of the interaction is given by the so called Rabi frequency Ω which can be expressed as [38]:

$$\Omega \equiv \frac{\vec{\mu}_{eg} \cdot \vec{E}_0}{\hbar} \tag{2.1}$$

where $\vec{\mu}_{eg}$ is the dipole moment of the transition between the ground and the excited levels and e is the electron charge. This interaction induces a radiative force that, if the atoms is at rest, can be expressed as [39]:

$$\vec{F} = \vec{F}_{\mathrm{rp}} + \vec{F}_{\mathrm{react}} \tag{2.2}$$

that is the sum of two components namely a dissipative force $\vec{F}_{\mathrm{rp}}$ and a conservative, reactive force $\vec{F}_{\mathrm{react}}$. If we consider the components of the dipole vector coming from the steady state solution of optical block equations we have:

$$u_{\mathrm{st}} = \frac{\delta}{\Omega}\frac{s}{1+s} \quad v_{\mathrm{st}} = \frac{\Gamma}{2\Omega}\frac{s}{1+s} \quad \omega_{\mathrm{st}} = \frac{1}{2(1+s)} \tag{2.3}$$

where $\delta = \omega - \omega_0$ is the frequency detuning from the atomic resonance, Γ is the natural with of the atomic resonance and $s = \frac{\Omega^2}{2}\frac{1}{\delta^2+\Gamma^2/4}$ is the saturation parameter. Using eq.(2.3) the two forces are:

$$\vec{F}_{\mathrm{rp}} = -\hbar\Omega v_{\mathrm{st}}\vec{\nabla}\phi \quad \text{and} \quad \vec{F}_{\mathrm{react}} = -\hbar\Omega u_{\mathrm{st}}\frac{\vec{\nabla}\Omega}{\Omega} \tag{2.4}$$

with $\vec{\nabla}\phi$ as the phase gradient of the laser field. The dissipative term is also known as radiation pressure and, given its non-conservative nature, it is exploited to perform laser cooling. On the other hand, the reactive force, also called dipole force, is conservative and can be used to confine atoms and generate atomic traps.

2.1.1 Laser Cooling

We now concentrate on the radiation pressure term which, combining eq.(2.4) and (2.3), is [8]:

$$\vec{F}_{\text{rp}} = \hbar\vec{k}\frac{\Gamma}{2}\frac{s}{1+s+(\frac{\delta}{\Gamma})^2} \tag{2.5}$$

where $\vec{k}$ is the wave-vector of the incident light field. The physical interpretation of this phenomenon comes from the multiple stimulated absorption and the subsequent spontaneous emission of photons by the atom. In fact, the photon carries a momentum $\hbar\vec{k}$ which excites the atom that subsequently spontaneously decays to the ground state, re-emitting a photon with a momentum of the same magnitude but random direction. This difference in the direction of the photons' momenta, after averaging many interactions, gives rise to a force exerted on the atom with the same direction of the laser's photon momentum. This force is maximized when the light is resonant with the atomic transition ($\delta = 0$) and it saturates to a limiting value $F = \hbar\vec{k}\Gamma/2$ if $s \gg 1$. This limit is posed by the spontaneous emission rate Γ, or excited state lifetime$1/\Gamma$, which regulates the number of scattered photons per units of time. Since after every absorption/emission cycle the atom gains a fraction of momentum along $\vec{k}$, this eventually sets the resulting force. The factor $1/2$ is a consequence of the saturation regime where the laser intensity is so high, thus also the number of photons, that as soon as the atom decays is immediately re-excited. In the case of many atoms this means that the populations of ground and excited states atoms approaches to $1/2$. For high intensity laser beams the stimulated emission is also present but, since it generates a photon collinear to the incoming light, it does not contribute to the net force.

To quantify this force we can consider Yb ($m \simeq 2.87 \times 10^{-25}\,\text{Kg}$) atoms with the transition ${}^1\text{S}_0 - {}^1\text{P}_1$ at $\lambda = 2\pi/k = 399\,\text{nm}$ and $\Gamma/2 = \pi \times 29\,\text{MHz} \simeq 9 \times 10^7$ photons scattered per second at saturation. The resulting force is $F \simeq 1.5 \times 10^{-19}\,\text{N}$ and hence the acceleration is $a = F/m \simeq 5 \times 10^5\,\text{m/s}^2$ which is about 50 000 times larger the gravitational Earth acceleration. This represents the core mechanism exploited to manipulate atomic motion which gave birth to laser cooling in 1995 [40, 41, 42].

If we consider now many atoms in motion, the radiation pressure can be used to reduce their velocity. In this case the laser frequency seen by the atoms is shifted by Doppler effect as $\omega' = \omega\left(1 + \frac{v}{c}\right)$. As a consequence, when atoms speed changes, so does the laser frequency (in the atom reference frame), making them out of resonance condition and quickly stopping the deceleration process. This problem can be addressed in two ways: either by sweeping the laser frequency or by inducing variation on the atomic resonance by Zeeman effect [8]. In the latter case an atomic beam can be slowed by using a counter-propagating laser beam at fixed frequency together with a space-varying magnetic field making the so called Zeeman slower.

The use of pairs of counter propagating laser beams with same intensity and

frequency tuned below resonance ($\delta < 0$) allows to generate a reduction of the velocity dispersion of the atoms along the lasers' propagation axis, thus realizing a laser cooling process. From eq.(2.5), including the Doppler shift, the force exerted on the atoms in this configuration is:

$$\vec{F}_{\mathrm{rp}} \simeq \hbar\vec{k}\frac{\Gamma}{2}\left[\frac{s}{1+\frac{4(\omega-\omega_0-kv)^2}{\Gamma^2}} - \frac{s}{1+\frac{4(\omega-\omega_0+kv)^2}{\Gamma^2}}\right] \tag{2.6}$$

which shows how on an atom at rest there is no force applied while, if an atom moves toward one of the two beams, it became resonant with the light and experiences a force against its motion. Expanding this force for small velocities and small laser intensity ($s \ll 1$) gives:

$$F_{\mathrm{sp}} \simeq -\alpha v + \mathcal{O}(v^3) \tag{2.7}$$

which corresponds to a friction force with damping coefficient:

$$\alpha = -8\hbar k^2 s \frac{\delta/\Gamma}{\left(1+(\frac{2\delta}{\Gamma})^2\right)}. \tag{2.8}$$

That is indeed positive for $\delta < 0$ and it is maximized for $\delta = -\Gamma/2$. This kind of arrangement is called *optical molasses*.

The concept of laser cooling implicitly refers to the temperature of the atomic sample. Since the system is non in thermal equilibrium, but rather in a steady-state regime where the atoms are continuously interacting with light, the temperature is not trivially defined. From the equipartition theorem we can express an effective temperature from the averaged squared velocity $\langle v^2\rangle$ of the atomic ensemble in the optical molasses as:

$$\frac{1}{2}k_{\mathrm{B}}T = \frac{1}{2}m\langle v^2\rangle. \tag{2.9}$$

The steady state is reached when the radiation pressure force equals the heating effects that are the atom recoil after spontaneous emissions together with the fluctuation of the intensity of laser beams. This sets a lower limit temperature called Doppler temperature[38]:

$$T_D = \frac{\hbar\Gamma}{4k_{\mathrm{B}}}\frac{1+(\frac{2\delta}{\Gamma})^2}{(\frac{2\delta}{\Gamma})} \tag{2.10}$$

that is minimized for $|\delta| = \Gamma/2$ (which equivalent to maximize the damping force):

$$T_D^{\mathrm{min}} = \frac{\hbar\Gamma}{2k_{\mathrm{B}}}. \tag{2.11}$$

From the last equation we can appreciate how the lowest temperature obtainable with laser cooling is limited by the linewidth of the atomic transition (or spontaneous decay rate) exploited to cool the atoms. Getting back to the Yb

atom example, using the $^1S_0 - {}^1P_1$ transition we have $\Gamma = 2\pi \times 29\,\mathrm{MHz}$, obtaining $T_D^{\min} \simeq 700\,\mu\mathrm{K}$.

Nevertheless, it has to be stressed that previous results were obtained in the two level atom approximation that, for real atoms, does not lead to an accurate description. In fact, in a multi-level atom sub-Doppler cooling mechanisms play a significative role allowing to reach lower limit temperatures [8]. However, during the operation of and optical lattice clock temperatures are typically close to the Doppler limit without surpassing it.

2.1.2 Magneto Optical Trap

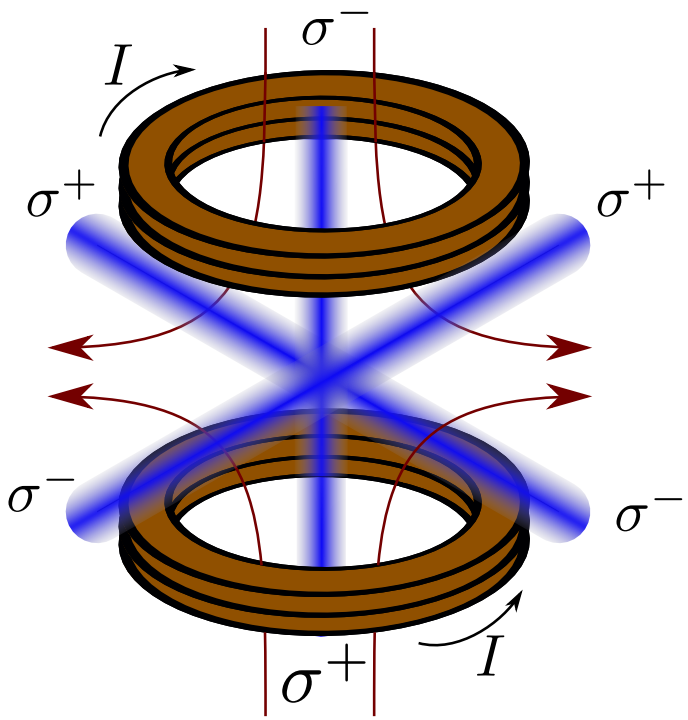

Figure 2.1: Example of a three dimensional MOT with anti-Helmoltz coils. I indicates the current flow in the coils while in dark red are the magnetic field lines.

Optical molasses bring a huge reduction in the atomic temperature but they do not provide any spatial confinement, leading to a diffusive expansion of the atomic cloud. To implement spatial confinement, in addition to the viscous term in eq.(2.7), is required a position dependent force. This is fulfilled by a magneto-optical trap (MOT), which exploits the combined effect of optical molasses, magnetic fields and polarized light (see figs. 2.1 and 2.2).

Considering a simple 1D case, the presence of an inhomogeneous magnetic field of the form $B_x = bx$ induces a space dependent Zeeman splitting of atomic levels

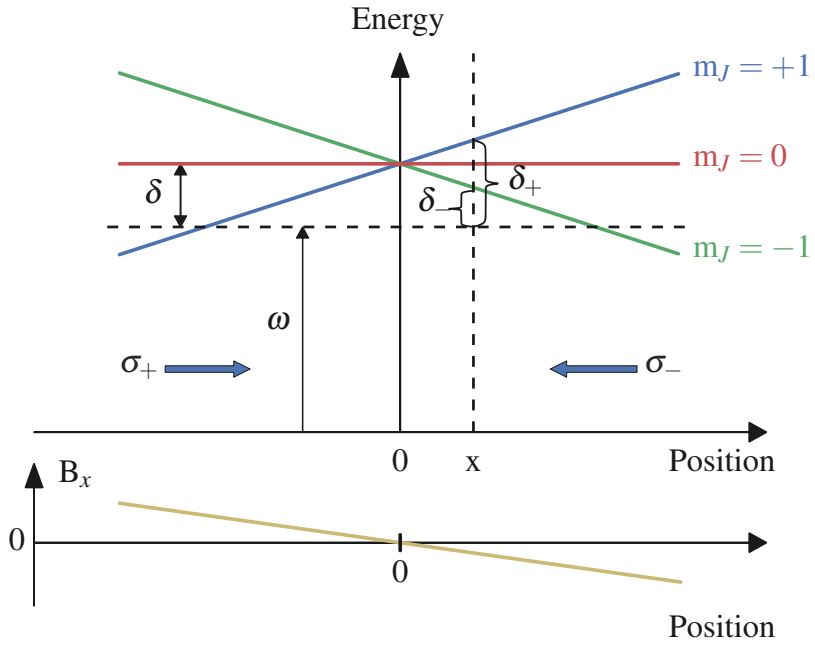

Figure 2.2: Scheme of functioning of a 1D MOT.

that nulls at $x = 0$. Considering the case of an atom with total angular momentum for the ground and excited state of $J_g = 0$ and $J_e = 1$ respectively, the magnetic field splits the excited state in three by:

$$\Delta E(x) = g_{J_e} \mu_B m_{J_e} b x \tag{2.12}$$

where g_{J_e} is the Landé factor for the excited state, μ_B is the Bohr magneton and $m_{J_e} = 0, \pm 1$ is the projection of the total angular momentum along the magnetic field axis. The Zeeman splitting makes the atomic resonance space-dependent but also dependent on m_{J_e}. The use of red detuned counter propagating laser beams with opposite circular polarization guarantees the right selection rules. In fact, to conserve the total angular momentum, a laser σ^+ polarized drives the transition with $m_{J_g} = 0 \rightarrow m_{J_g} = +1$ while σ^- the opposite $m_{J_g} = 0 \rightarrow m_{J_g} = -1$ giving rise to a preferential absorption of photons from one of the two beams, depending on the position.

From fig. 2.2 we can see how at $x = 0$ the magnetic field vanishes and also the Zeeman splitting while, moving away from the origin, the constant gradient linearly splits the Zeeman threefold. The two counter propagating laser beams have opposite circular polarization (σ_+ and σ_-) and are both red detuned from the unperturbed transition by δ. This results in a space dependent resonance frequency which also depend on the light polarization. Therefore, an atom situated at $x = 0$ does not experience any net force whereas if it is placed, for instance, at $x > 0$ it will be closer to resonance with the σ^- ($\delta_+ > \delta_-$) light while at $x < 0$ with σ^+

($\delta_+ < \delta_-$) generating a radiation pressure force always pointing toward the centre of the trap. More quantitatively it can be expressed as[38]:

$$\vec{F} \simeq \hbar\vec{k}\frac{\Gamma}{2}\left[\frac{s}{1+\frac{4(\omega-\omega_0-kv-g_{J_e}\mu_B bx/\hbar)^2}{\Gamma^2}} - \frac{s}{1+\frac{4(\omega-\omega_0+kv+g_{J_e}\mu_B bx/\hbar)^2}{\Gamma^2}}\right] \tag{2.13}$$

that comes from eq.(2.6) with the addition of the Zeeman splitting. Expanding this equation for small x and v we obtain:

$$F_x \simeq -\alpha v - \kappa x \quad \text{with} \quad \kappa = \frac{g_{J_e} m_{J_e} \mu_B b}{\hbar k}\alpha \tag{2.14}$$

which is the equation of a damped harmonic oscillator with spring constant κ.

The method can be extended in the 3D case by using three pairs of counter propagating polarized laser beams, along the three orthogonal axis, and a spherical quadrupole magnetic field generated by a pair of anti-Helmoltz coils (see fig. 2.1). The atoms, usually manipulated in ultra-high vacuum chambers (pressure $< 10^{-9}$ mbar), can be cooled and trapped for extended time (up to several minutes), limited only by collisions with residual gas particles

2.2 Optical Lattice

Taking back eq. (2.4) it can be seen how the conservative component of the radiative force depends on a spatial variation of the laser field intensity. The use of focused far detuned laser light is fundamental to realize optical trap for neutral atoms.

Expanding the expression for dipole force we have [39]:

$$\vec{F}_{\text{react}} = -\frac{\hbar\delta}{4}\frac{\vec{\nabla}\Omega^2}{\delta^2 + (\Gamma^2/4) + (\Omega^2/2)} \tag{2.15}$$

this depends both on the frequency detuning and, through the Rabi frequency, on the laser intensity. It vanishes in absence of an intensity gradient in the laser field. The sign of the frequency detuning determines the sign of the force: a blue-detuned laser beam ($\delta > 0$) impresses a force that repels atoms away from high intensity regions while a red-detuned laser ($\delta < 0$) attracts them.

The physical origin of this force can be seen as a consequence of a coherent absorption and stimulated emission of photons. In the case of plane waves there is a single wave vector $\vec{k}$ and no amplitude gradient, thus the stimulated absorption-emission can happen only along $\vec{k}$ resulting in a zero net force. On the other hand, a non-zero laser amplitude gradient can be thought as generated by the superimposition of several plane waves with equal frequency but different wave vectors ($\vec{k}_i \neq \vec{k}_j$). The force arises from the stimulated absorption of photons

from a wave i and a subsequent stimulated emission in a different one j. This sort of "redistribution" of photons does not exchange energy ($\hbar\omega_i = \hbar\omega_j$) but the momentum changes by $\hbar(\vec{k}_i - \vec{k}_j)$ giving e conservative force. Given the fact that the effect involves a coherent process, the force is not limited by the spontaneous emission rate and can increase indefinitely with Ω.

The easiest way to generate an optical lattice is by making interfere two focused counter propagating laser beams at the same, red-detuned, frequency. This creates a standing wave along the propagation axis of the lasers (1 dimensional lattice) with an intensity modulation of the laser field with maxima spaced by $\lambda/2$ along the propagation axis (lattice longitudinal dimension). The focused lasers Gaussian shape provides an intensity gradient also along the transverse direction. The dipole force can be expressed as function of a trapping potential U that in this configuration, and with red detuned lasers (attractive force toward maxima of intensity), is:

$$U(r,z) = -U_0 \cos^2(2\pi z/\lambda) e^{-2r^2/\omega_0^2} \tag{2.16}$$

where z and r are the longitudinal and radial coordinates respectively while U_0 is the trap depth and ω_0 is the beam waist radius. From this equation the periodical modulation of the lattice appears in the cosine term while the transverse confinement is expressed by the exponential. The trap depth can be deduced from the (one way) optical power P as[43]:

$$U_0 = \frac{4\alpha_i P}{c\epsilon_0 \pi \omega_0^2} \tag{2.17}$$

with α_i being the polarizability of state $|i\rangle$.

In presence of a deep lattice we can assume the trapping potential to be harmonic ($V(x) = 1/2m\omega^2 x^2$) in the proximity of the minima:

$$U(z,r) \simeq U_0 \left[\left(\frac{2\pi z}{\lambda}\right)^2 + \frac{2r^2}{\omega_0^2} \right] = \frac{1}{2} m\omega_z^2 z^2 + \frac{1}{2} m\omega_r^2 r^2 \tag{2.18}$$

where m is the atom mass. The longitudinal and radial frequencies are:

$$\begin{aligned} f_z &= \frac{\omega_z}{2\pi} = \frac{1}{\lambda}\sqrt{\frac{2U_0}{m}} \\ f_r &= \frac{\omega_r}{2\pi} = \frac{1}{\omega_0}\sqrt{\frac{2U_0}{m}} = \frac{1}{\omega_0}\lambda f_z. \end{aligned} \tag{2.19}$$

2.2.1 Tight confinement - Lamb Dicke regime

The confinement of many atoms inside the optical lattice potential gives the big advantage to suppress the atomic motion and allows an extended spectroscopic

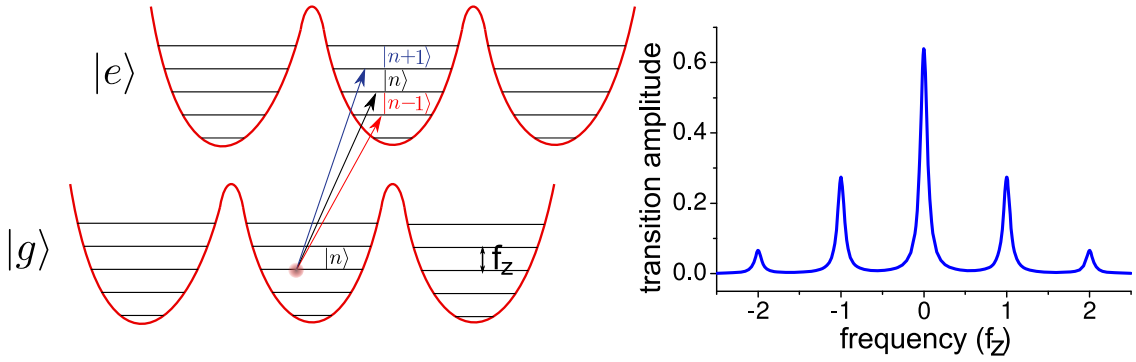

Figure 2.3: Left: harmonic trapping sites of the optical lattice with motional sidebands. The transition between ground and excited state with the exchange of quantum of motion. In black there is the carrier which is a pure electronic transition while in red is the first red sideband and in blue the first blue sideband. Right: Spectrum generated by the Lamb-Dicke regime showing the motional sidebands and the unperturbed pure electronic transition. From [7].

interrogation. Following the harmonic approximation, we can see that longitudinal trapping gives the well known energy spectrum of a harmonic oscillator (see fig. 2.3):

$$E_n = hf_z(n + 1/2) \tag{2.20}$$

where n is integer and called vibrational quantum number. The strength of the confinement along the lattice axis determines the separation of vibrational levels by f_z. The atomic state can be thus divided in two elements namely the electronic part (internal degree of freedom) and the motional part (external degree of freedom). The former gives the usual transition among ground and excited state while the motional term brings the vibrational quantum number n into play. As a consequence, when the trapped atoms are probed by a laser sent along the lattice axis, can make purely electronic transition $|g, n\rangle \rightarrow |e, n\rangle$ at frequency ω_0 or can exchange a quantum of motion $|g, n\rangle \rightarrow |e, m\rangle$ at frequency $\omega_0 + (m - n)2\pi f_z$.

The magnitude of confinement is expressed by the Lamb-Dicke parameter η, which compares the spatial extent of the confined atom to the transition wavelength:

$$\eta \equiv k\Delta x = k\sqrt{\frac{\hbar}{2m\omega_z}} = \sqrt{\frac{\omega_R}{\omega_z}} \tag{2.21}$$

where $\omega_R = \hbar k^2/(2m)$ is the recoil frequency of the atom exchanging a photon at ω_0 and $\omega_z = 2\pi f_z$ and k is the wave-vector of the probing light.

If $\eta \ll 1$ the atom is in the so called "Lab-Dicke regime" where it is trapped in a region smaller than the wavelength of the probing transition. In this regime, the lattice potential, which provides the confinement, takes the recoil momentum from the atoms leaving the pure electronic carrier transition not shifted or broadened

by motional effects and the sidebands, generated by the transitions with different motional levels, are well resolved.

The relative amplitude of the motional sidebands carries information about the average motional level occupied by the atomic sample. Intuitively, a lower red sideband is related to a lower $\langle n \rangle$ since an atom at $n = 0$ do not have the possibility to go to lower states and thus more atoms undertake a transition $|g, n\rangle \rightarrow |e, n+1\rangle$ than $|g, n-1\rangle \rightarrow |e, n\rangle$.

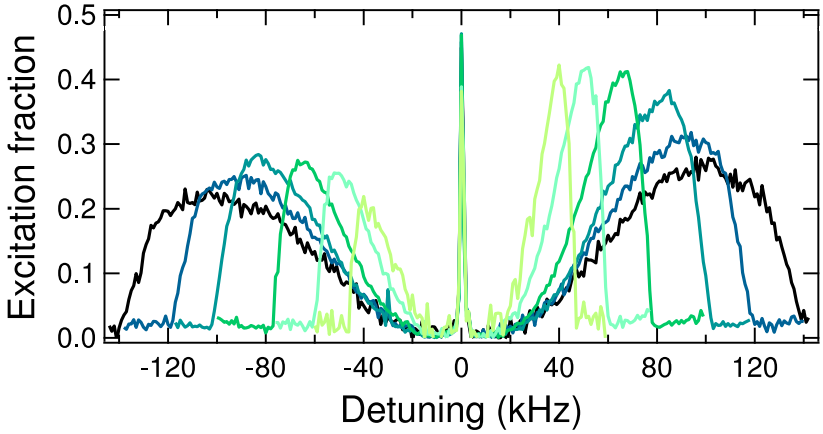

Figure 2.4: Sideband spectroscopy of the $^1S_0 - ^3P_0$ clock transition of ^{171}Yb atoms trapped in an optical lattice at different trap depth. Darker traces indicate stronger trap. From [44].

The typical way to assess informations about trapping condition, like trapping frequency and the sample temperature, is by performing motional sideband spectroscopy like reported in sec.5.1.6. Fig. 2.4 shows a typical sideband spectra taken at different trap depth. It can be noticed how the motional sidebands are smeared toward the central carrier. This results from the coupling of the radial confinement with the longitudinal trap. In fact, atoms are tightly trapped only along the lattice axis while, given the weaker transverse confinement, they can move across the entire transverse profile of the beam, particularly if they occupy a high transverse motional quantum number. When an atom is at a low intensity region of the Gaussian profile it senses a lower longitudinal confinement which reflects in a lower trap frequency. Moreover, for atoms with a high longitudinal motional level the harmonic approximation is not accurate, as they start to feel anharmonicity of the trapping sites, and this also gives lower trap frequencies.

2.2.2 Lattice light shift and magic frequency

Trapping of many atoms in optical lattice is the key feature to suppress Doppler and recoil effects and achieve a high resolution spectroscopy. The dipole force used

to confine the atoms is generated from the interaction with a strong light field and is a manifestation of the AC Stark effect [8]. This effect strongly perturbs the atoms' internal degrees of freedom thus affecting the clock transition and its frequency. To realize an accurate frequency standard this light shift has to be carefully compensated.

The interaction with a lattice laser field having electric component E_0 and frequency ω_L introduces a shift on the state $|i\rangle$:

$$\Delta\omega_i = -\frac{1}{4\hbar}\alpha_i(\omega_L, \vec{e})E_0^2 \tag{2.22}$$

where $\alpha_i(\omega_L, \vec{e})$ is the dipole polarizability of the state $|i\rangle$, which depends on the lattice frequency and its polarization $\vec{e}$. As a consequence, an atomic transition between ground (g) and excited (e) state is shifted (at first order) from the unperturbed value ω_{eg} according to:

$$\omega_{eg}^* = \omega_{eg} - \frac{1}{4\hbar}\Delta\alpha_{eg}(\omega_L, \vec{e})E_0^2 + \mathcal{O}(E_0^4) \tag{2.23}$$

where $\Delta\alpha_{eg} = \alpha_e - \alpha_g$ is the differential dipole polarizability between the two states.

The idea proposed by H. Katori in 2002 [45] was to cancel the first order light shift of $J = 0 \rightarrow J = 0$ clock transition of alkaline heart(-like) atoms by inducing the same AC Stark perturbation on both the ground and the excited states, therefore leaving the clock transition frequency unperturbed. This can be done by tuning the lattice laser frequency at the so called *magic frequency* where

$$\alpha_e(\omega_{\text{magic}}) = \alpha_g(\omega_{\text{magic}}) \quad \Rightarrow \quad \Delta\alpha_{eg}(\omega_{\text{magic}}) = 0. \tag{2.24}$$

Figure 2.5 shows the polarizabilities of the $^1\text{S}_0$ and $^3\text{P}_0$ atomic states in the case of ^{171}Yb atoms that are, respectively, the ground and excited states of the clock transition. It can be seen that, in this case, the magic wavelength at about 759 nm. In addition, it has been demonstrated [20] that the scalar nature of the clock states ($J = 0$) gives a negligible dependency on the polarization of the lattice light, thus we can drop the $\vec{e}$ dependency of the scalar polarizability.

The description given so far allows to realize an optical frequency standard with an accuracy at the 10^{-16} level [46]. When we approach to lower uncertainty, the concept of magic wavelength confinement breaks down and higher order correction needs to be taken into account. The first contribution comes from interactions different from the electric dipole (E1) that modify the scalar polarizability. Considering magnetic dipole (M1) and electric quadrupole (E2) transitions we can write [20]:

$$\alpha(\omega_L) = \alpha_{\text{E1}}(\omega_L) + \alpha_{\text{M1}}(\omega_L) + \alpha_{\text{E2}}(\omega_L) \tag{2.25}$$

where α_{E1} dominates and multipolar polarizabilities $\alpha_{\text{M1(E2)}}$ are calculated to be about 10^6 times smaller than α_{E1} [20, 46]. The effect of these correction is to slightly shift the magic wavelength obtained considering only E1 interactions.

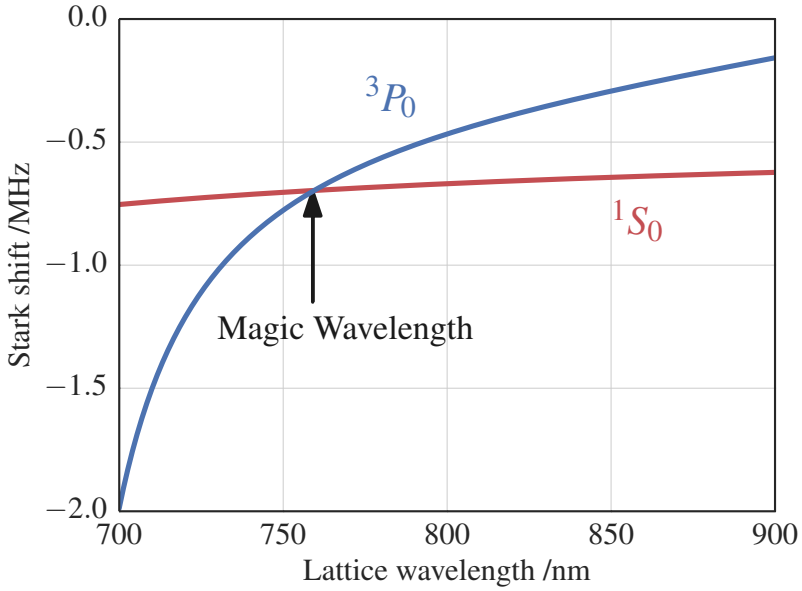

Figure 2.5: Light shift of the clock transition ground and excited states in ^{171}Yb as function of lattice laser wavelength. A crossing point is present which wavelength corresponds to the magic wavelength.

Another important factor to be taken into account is the $\mathcal{O}(E_0^4)$ term from eq. (2.23). If we consider the second order light shift we obtain:

$$\omega_{eg}^* = \omega_{eg} - \frac{1}{4\hbar}\Delta\alpha_{eg}(\omega_L)E_0^2 + \frac{1}{64\hbar}\Delta\gamma(\omega_L, \vec{e})E_0^4 - \dots \tag{2.26}$$

where is visible the second order shift characterized by the difference between *hyperpolarizabilities* of the upper and lower states $\Delta\gamma$ coming from two photons interactions closed to the magic wavelength. Even though the scalar term is nulled at the magic wavelength, the quadratic term still introduces a shift of $\approx 10^{-17}$ to the clock transition [47] which, if not properly controlled, can limit the accuracy of the standard.

On the top of that, the atomic trapping in the lattice potential at the Lamb-Dicke regime introduces quantized motion of the atoms that, consequently, experience different trapping conditions depending on n. This, in particular, has an impact on the spatial dependence of the multipolar couplings term, giving rise to a light shift $\propto \sqrt{E_0^2}$ [46].

When all these subtle effects are taken into account, together with anarmonic modifications of the trapping potential, the resulting light shift induced by a 1D optical lattice in the proximity of the E1 magic wavelength is [48]:

$$\Delta\nu_{ls}(I, n, \Delta\nu_L) = c_1(n, \Delta\nu_L)I + c_2(n, \Delta\nu_L)I^2 + c_{1/2}(n, \Delta\nu_L)I^{1/2} + c_{3/2}(n, \Delta\nu_L)I^{3/2} \tag{2.27}$$

where $I = \epsilon_0 c E_0^2$ is the single lattice laser beam intensity while c coefficients carry the dependency on the lattice frequency detuning from the magic frequency $\Delta\nu_L$ and the vibrational level occupied by the atoms n. The scalar part is cancelled at the magic wavelength, the quadratic part accounts for the hyperpolarizability while the last two terms take into account the multipolar effects.

The explicit version of the light shift formula together with the experimental evaluation of lattice light shift for the INRIM clock has been reported in chapter 5. The effect of different atomic temperatures, thus changing n, on the lattice light shift has been experimentally investigated by the NIST Yb optical lattice clock experiment and reported in chapter 6 along with a different theoretical derivation. In addition, the *operational magic frequency* is introduced to surpass the limits of the standard magic frequency by using the combined effect of the linear and quadratic shifts.

2.3 Magnetic field sensitivity

^{171}Yb is an odd isotope and possesses a nuclear spin of 1/2 which is responsible for the hyperfine structure. This makes possible the quenching of the metastable $^3\mathrm{P}_0$ state lifetime allowing an ultra narrow, but non zero, linewidth of the double forbidden clock transition $^1\mathrm{S}_0 - ^3\mathrm{P}_0$. This transition, in presence of a magnetic field that lifts the degeneracy, is splitted in two magnetic components. The spectroscopy of these components allows to experimentally remove the shift induced by magnetic fields while the preparation of the atomic sample in a single hyperfine ground state level permits to suppress cold collisions among atoms.

2.3.1 Zeeman coupling

The presence of a nuclear spin I gives rise to a hyperfine structure with $2F + 1$ substates, where $F = J + I$ is the total angular momentum. Since for both clock states $J = 0$, the hyperfine levels are $2I+1$ so the ground and excited states are both twofold ($m_F = \pm 1/2$, where m_F is the F component parallel to the quantization axis) and degenerate. The degeneracy is broken by the application of an external magnetic field $\vec{B}$, which also defines the quantization axis, through the Zeeman effect:

$$\Delta E_B = -(g_I + g_{HFI}) m_F \mu_\mathrm{B} B \tag{2.28}$$

where g_I is the Landè factor related to the nuclear spin while g_{HFI} comes from the hyperfine mixing of the $^3\mathrm{P}_0$ state, μ_B is the Bohr magneton and B is the magnitude of the magnetic field. For ^{171}Yb we have $g_I = 0.4919\mu_N$ and $g_{HFI} \simeq 2.9 \times 10^{-4}$ [26] where μ_N is the nuclear magneton which is smaller than μ_B by the ratio between the masses of electron and proton. The $^1\mathrm{S}_0$ is subjected to the Zeeman shift caused only by the nuclear spin while $^3\mathrm{P}_0$ is perturbed by both contributions.

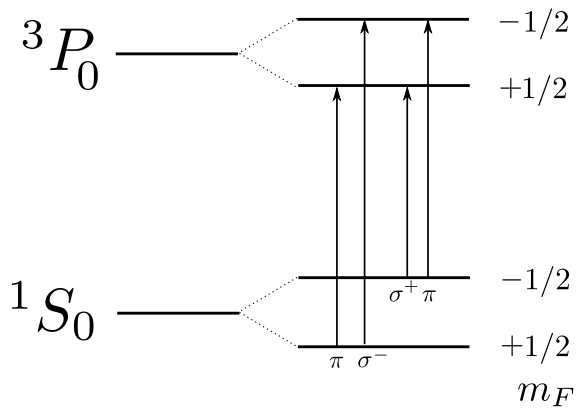

Figure 2.6: Diagram of the hyperfine structure of the clock transition for ^{171}Yb in presence of Zeeman splitting.

The scheme of the hyperfine levels of the clock transition is reported in fig. 2.6. The selection of the transition of interest is done using polarized light, in fact circular polarized light ($\sigma^{\pm}$) makes $\Delta m_F = \pm 1$ while linear polarized (π) makes $\Delta m_F = 0$.

By measuring the frequency of the two π transitions it is possible to monitor in real time the magnetic field environment during the operation of the clock and subsequently cancel the the Zeeman shift. However, this requires the presence of a bias magnetic field during spectroscopy that introduces also a second order Zeeman shift that has to be characterized (see sec.5.3.3).

2.3.2 Scalar, vector and tensor light shift

A neutral atoms becomes polarized in presence of an electric field of a laser radiation and this is regulated by the polarizability term α. Given the scalar nature of the clock transition (both ground and excited states have $J = 0$) the scalar polarizability would be the only perturbation present. This can be zeroed by tuning the lattice laser at the magic wavelength. However, the nuclear structure introduces other perturbations to the clock transition. Indeed, the hyperfine mixing of the metastable ^{3}P$_0$ state brings in a non-zero vector and tensor polarizability of the excited state.

Considering the vector light shift, it is described by [49]:

$$\delta\nu_V = -\alpha_V \frac{m_F}{2F} \xi \frac{E_0^2}{2h} \tag{2.29}$$

where α_V is the vector polarizability and ξ indicates the ellipticity of the light namely $\xi = \pm 1$ for circular polarization and $\xi = 0$ for linear. Given the linear dependence with m_F, this effect can be seen as a pseudo magnetic field aligned with the propagation axis of the lattice and it vectorially sums with the bias magnetic

field. Calculations of α_V indicate that this term is about 1600 times smaller than the scalar one [26].

Even thought the effect can be ideally suppressed by using a linearly polarized lattice laser, the light seen by the atoms in a real experiment is polarized at a certain level and disturbances can be present (stress induced birefringence of the optics and view-ports). By measuring the two magnetic components of the clock transition ($m_F = \pm 1/2$), this residual shift can be experimentally reduced to a level that is negligible in the count of uncertainties.

As fa as the tensor light shift is concerned, for a transition with $\Delta m_F = 0$ the shift is [49]:

$$\delta\nu_T = \alpha_T U_0 [3m_f^2 - F(F+1)] \tag{2.30}$$

where α_T is the tensor polarizablity. It can immediately seen that in the case of ^{171}Yb its total angular momentum of $F = 1/2$ is not enough to sustain a tensor shift which in fact vanishes. This gives a significant advantage for ^{171}Yb compared to other atomic species with higher nuclear spin (like Cs which has $I = 9/2$).

2.3.3 Optical Pumping

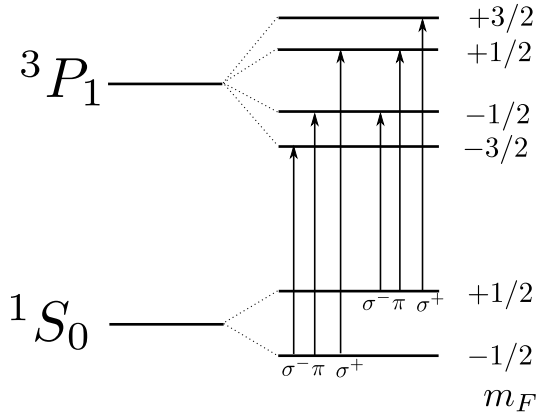

Figure 2.7: Hyperfine splitting of the $^1S_0 - ^3P_1$ levels, the relevant transitions with their polarizations are sketched.

Naturally, the atomic population is equally divided among the two ground state Zeeman levels. The splitting of the spectroscopic features causes a reduction by a half of the contrast and thus also does the signal-to-noise ratio. To avoid that, the atomic sample needs to be prepared in a single, specific Zeeman level. Moreover, having an atomic ensemble prepared in the same quantum state strongly suppresses the cold collisions [50], reducing the impact of the systematic shift.

The way to achieve that is to optically pump atoms in the Zeeman level of

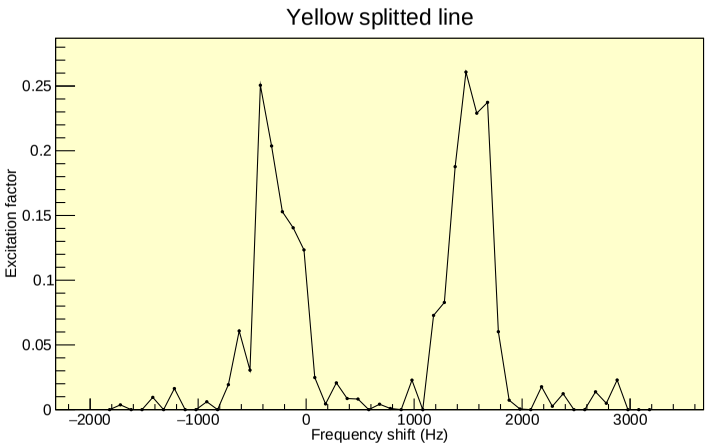

(a) Splitted line, no spin polarization.

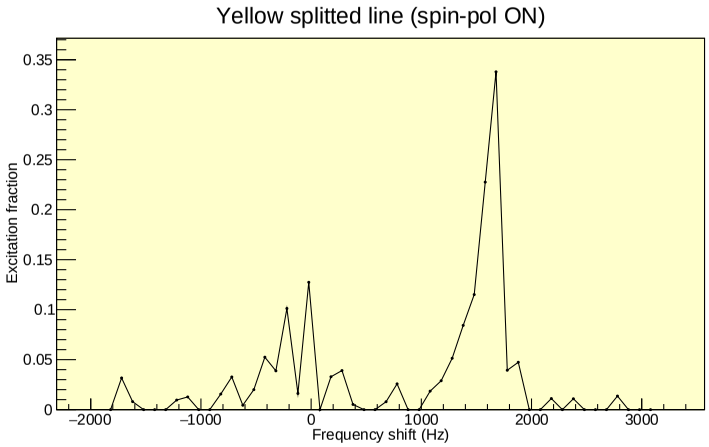

(b) Splitted line, spin polarization active - Partial pumping

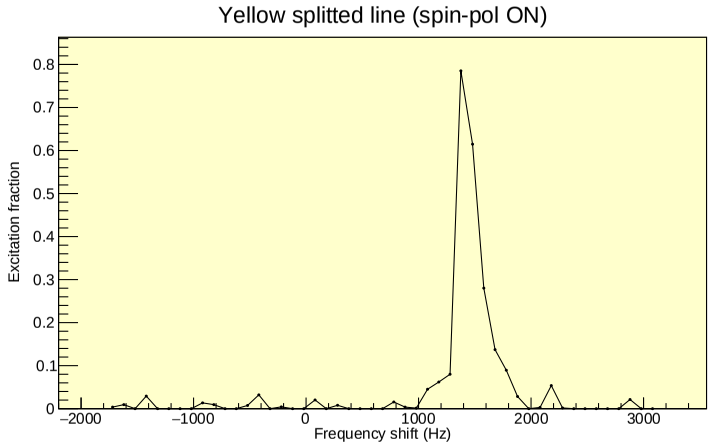

(c) Splitted line, spin polarization active

Figure 2.8: Example of the clock transition spectroscopy when the feature is splitted by the presence of a magnetic field and the atomic sample is gradually spin polarized.

interest, using the intercombination transition $^1S_0 - {}^3P_1$ at 556 nm. The hyperfine structure of the two levels is reported in fig.2.7. By selecting the proper frequency and polarization a single specific transition can be driven which can be either $m_F = 1/2 \rightarrow m_F = -1/2$ or $m_F = -1/2 \rightarrow m_F = 1/2$. Since the decay follows predominately (by a factor of two) the channel with no spin change ($\Delta m_F = 0$) a big fraction of the excited atoms falls in the "new" spin state (the opposite to the starting one) where they no longer interact with the light pulse. On the other hand, if atoms decay through a $\sigma_\pm$ transition ($\Delta m_F = \pm 1/2$),they return in their original state and can be excited again. By repeating this process several times the atoms are pumped in a specific spin state with an efficiency of more than 99 % (see fig. 2.8).

2.4 Spectroscopy techniques

In optical lattice clocks the interrogation of the ultra cold atomic ensemble held in the optical lattice is made by means of two different techniques namely the Rabi and Ramsey methods. Using these methods allows to measure narrow spectroscopic features that are used as frequency reference to tune the clock laser frequency.

The Rabi technique is used by the INRIM clock (presented in the following chapters) while the NIST experiment (presented in chapter 6) can operate using either methods.

Rabi scheme

This method is based on the coherent excitation of atoms by means of a single resonant probe laser pulse. This is regulated by the dipole interaction Hamiltonian $H_{\text{int}} = \vec{d} \cdot \vec{E}$ ($\vec{d}$ is the atomic dipole moment and $\vec{E}$ is the laser electric field) that leads to an atomic excitation called *Rabi Flopping*. The probability for an atom to be excited depends on both the intensity of the probe laser, the duration of the interrogation (t) and its frequency detuning from the resonance (δ). The population of the excited state can be expressed as [8, 38]:

$$P_e(t, \delta) = \frac{\Omega^2}{\Omega^2 + \delta^2} \sin^2\left(\frac{\sqrt{\Omega^2 + \delta^2}\, t}{2}\right) \tag{2.31}$$

where Ω is the Rabi frequency (eq. (2.1)). If a π-pulse is applied ($\Omega t = \pi$) the probability becomes a sinc^2 and it is maximized in the case of $\delta = 0$. The Fourier-limited full width half maximum of the resulting line-shape is $\Delta\nu_{\text{Rabi}} \simeq 0.8/t$ and points out the importance of an extended interrogation time (see fig. 2.9). Longer t gives narrower spectroscopic lines, limited only by the coherence time of the probing laser.

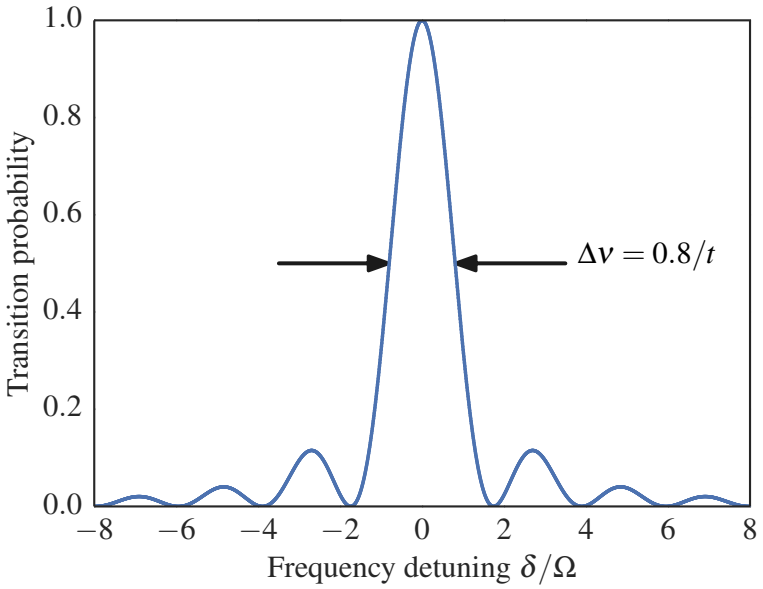

Figure 2.9: Typical Rabi spectrum obtained with $\Omega t = \pi$.

Ramsey scheme

A different spectroscopy technique, developed by N.F. Ramsey in 1950 [9], consists in the application of two probing pulses of duration τ_p spaced by a certain amount of *dark time* or *free-evolution time* T. Contrary to what happens in microwave frequency standards, in optical lattice clocks the atomic sample do not moves through two separate regions of interaction but remains trapped in the lattice where is sequentially probed by two laser pulses.

The interaction starts having the atom in the ground state. When the first pulse is applied it generates a coherent superposition of ground and excited states. During the free evolution time the state freely evolves oscillating at a frequency $\omega' = \omega_0 + \delta$ among the ground and excited state. The second pulse project the state in one of the two basis states. If we consider an atomic ensemble the excitation probability is expressed as [51]:

$$P_e(\delta, \Omega, \tau_p, T) = \frac{4\Omega^2}{\Omega'} \sin^2(\Omega'\tau_p/2) \times \left(\cos(\Omega'\tau_p/2)\cos(T\delta/2) - \frac{\delta}{\Omega'} \sin(\Omega'\tau_p/2)\sin(T\delta/2) \right)^2 \tag{2.32}$$

with $\Omega' = \sqrt{\Omega^2 + \delta^2}$. Figure 2.10 shows a typical Ramsey spectrum, where we can identify a broad envelope (width $\simeq 0.8/\tau_p$), called Rabi pedestal, with many fringes. The central one, if $T \gg \tau_p$, has a linewidth $\Delta\nu_{\text{Ramsey}} = \frac{1}{2T}$ and it is taken

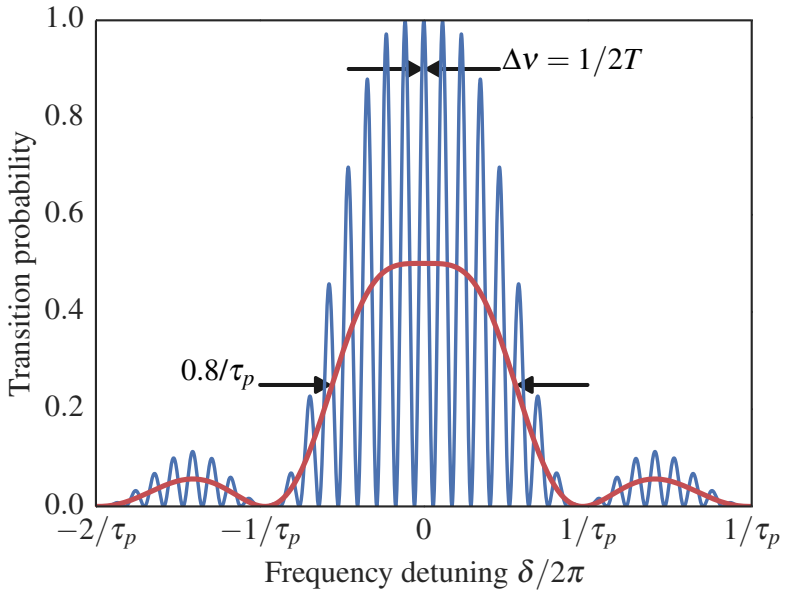

Figure 2.10: In blue, typical Ramsey spectum with two $\pi/2$ pulses of length τ_p separated by a free evolution time T. In red is represented the Rabi pedestal.

as frequency reference. To maximize the contrast the interaction time is tuned to be $\Omega\tau_p = \pi/2$ ($\pi/2$ pulse).

Comparing the linewidth obtained with the two methods, at the same interaction time (t=T), gives $\frac{\Delta\nu_{\text{Ramsey}}}{\Delta\nu_{\text{Rabi}}} \simeq 0.63$. Even if Ramsey spectroscopy gives narrower features on equal spectroscopy time, care must be taken to control the phase of probe laser between the two pulses.Indeed, a non perfect coherence results in a contrast reduction of the Ramsey fringes and, to assure this phase continuity, requires some caution in the experimental realization [21].

2.5 Clock laser stabilization

Performing high resolution spectroscopy on an ultra-narrow atomic transition poses strong requirements on the probe laser linewidth and its frequency stability The light driving the atomic transition must be highly coherent and frequency stable in order to probe the atoms for longer time, ultimately maximizing the line quality factor Q. This parameter is indeed present in the clock stability equation (1.2) while the local oscillator frequency noise is a critical factor in the Dick effect instability contribution (see par. 2.6.1).

Lasers are thought to be a coherent and monochromatic light source, however commercially the best available laser sources exhibit linewidths of about 10 kHz corresponding to a coherence time of about one hundred of microseconds. The

natural linewidth of the Yb clock transition ($^1S_0 \rightarrow {}^3P_0$) is less than 10 mHz thus requires the local oscillator to be pre-stabilized to a stable reference in order to be capable to perform spectroscopy on the atoms trapped in the lattice. This reference can be realized by an atomic transition or a physical device, like an optical cavity, that exhibit a better intrinsic stability than the free-running laser. Optical cavities are, in fact, the most common tool used to realize ultra-stable lasers around the world. These objects are fabricated with dimensional-stable materials allowing a reduction of the laser linewidth to a fraction of the cavity's narrow resonances as well as a control of the frequency drift. This approach basically transfers the mechanical stability of the resonator to the frequency of the laser. At the same time, the ability to modulate the laser frequency, that is the actual realization of laser lock the laser to the cavity, plays a fundamental role in the rejection of the noise.

Laser frequency can be tuned and referred to an external reference by means of a feedback mechanism which acts either directly on a laser parameter (piezo, grating, crystal temperature) or on an external modulator like an acusto-optic modulator (AOM). Several techniques have been developed to generate the adequate feedback signal (error signal) such as the Pound-Drever-Hall (PDH) or Hänsch-Couillaud methods [52, 53] in the case of cavities or, alternatively, side of fringe lock and spectral hole burning [54, 55] for spectroscopic features.

When designing an ultra-stable cavity two main aspect have to be addressed namely the optical properties of the cavity and the preservation of its mechanical stability

2.5.1 Ultra-stable cavities

An optical resonator, e.g. a Fabry-Perot cavity, act as an optical filter in the sense that only light with a certain wavelength can be stored inside it. The round-trip optical path length of the resonator $2L$ (L is the cavity length) must contain an integer number of wavelengths resulting in a series of discrete resonances separated in frequency by a *Free Spectral Range* ($\Delta\nu_{\mathrm{FSR}}$) that, for a 2 mirror cavity, is:

$$\Delta\nu_{\mathrm{fsr}} \equiv \frac{c}{2L}$$

where c is the speed of light. The resonance width $\delta\nu$ is described by the *Finesse*:

$$\mathcal{F} = \frac{\Delta\nu_{\mathrm{FSR}}}{\delta\nu}. \tag{2.33}$$

We can see that higher Finesse correspond to narrower and more spaced resonances. Intuitively this identify a more sensitive frequency discriminator. If we consider Lorentrzian cavity resonances, with only optical losses caused by the cavity mirrors,

the finesse can be expressed as [56]:

$$\mathcal{F} = \frac{2\pi}{-\ln(R_1 R_2)} \tag{2.34}$$

with $R_{1(2)}$ being the mirror reflectivity. From this equation it becomes clear that to make high finesse resonators the main focus is on the mirror optical losses. Currently the state of the art cavity mirrors are a fused silica substrate with a thin-film dielectric reflective coating with finesse that can go up to 877 000 [21], meaning a single mirror optical loss of few parts per million.

Big part of the work when designing an ultra-stable cavity is devoted to keep the mechanical stability of the optical cavity. Using an optical cavity as reference, in fact, directly links its length with the frequency of the lasers and, as a consequence, any variation of the distance between the two mirrors is reflected in a variation of the resonant frequency which is transferred to the laser.

Mechanical stability mainly depends on temperature and vibrations. Temperature changes induce length alterations in materials as well as mechanical vibrations cause deformations. To maintain a fixed cavity length, mirrors are attached on a special spacer via optical contact [57], which can have different shapes (cylindrical, square section, rugby-ball) and orientation (vertical or horizontal) to minimize the sensitivity to vibrations. Moreover, materials adopted to realize such a spacer are special type of glass, like Ultra Low Expansion (ULE) glass by Coroning or Zerodur by Shott AG, that exhibit a vanishing thermal expansion coefficient at a temperature of interest, usually close to room temperature (zero CTE). In particular, there is a quadratic dependency of the relative lenght variation, or the fractional frequency difference, with the temperature, close to the zero CTE temperature T_0:

$$\frac{\Delta L}{L} = \frac{\Delta \nu}{\nu} \simeq \alpha (T - T_0)^2 \tag{2.35}$$

where $\alpha \simeq 1 \times 10^{-9}\,\mathrm{K}^{-2}$ for ULE. Special care is also given to the holder of the cavity as the contact between the spacer glass and the support slightly bends and deform the materials. To this end finite element simulations are made to find the points which minimize the induced deformation and further reduce the vibrations sensitivity [58, 59].

All these actions ensures a minimal thermal and vibrational sensitivity of the cavity itself. On the other hand the environment where the optical cavity is positioned must be controlled as well to minimize disturbances. Typically the cavity is placed in a temperature stabilized vacuum chamber that, depending on the design, can give an insulation from the external environment with a time constant of days. Lastly the system is positioned on an anti-vibrational platform (passive or active) and enclosed in an anti acoustic chamber which minimizes the transmission of mechanical vibrations to the optical cavity.

Fundamental thermal limit After removing all the external disturbances, the ultimate fundamental limit for optical cavities comes from the thermal Brownian motion of the mirrors coating [60], which instability contribution can be expressed as:

$$\sigma_{\text{therm}} = \sqrt{\ln 2 \frac{8k_{\text{B}}T}{\pi^{3/2}} \frac{1-\sigma^2}{Ew_0L^2} \left(\phi_{\text{sub}} + \phi_{\text{coat}} \frac{2}{\sqrt{\pi}} \frac{1-2\sigma}{1-\sigma} \frac{d}{w_0}\right)} \tag{2.36}$$

where σ is the Poisson's ratio, E is the Young's modulus, ϕ_{sub} is the mechanical loss for the mirror substrate, w_0 is the laser beam radius on the mirror, T is the mirror temperature and L the length of the cavity. d and ϕ_{coat} are the thickness and the mechanical loss of the reflective coating, respectively.

State of the art ultra stable laser stabilized on optical cavity have a fractional frequency instability of some parts in 10^{17} [61], limited by Brownian thermal noise on the mirror surfaces.

To minimize the thermal limit one can operate on the optical parameter of the cavity, going for longer cavities with bigger beams, or acting on the temperature and build a cryogenic environment [62] or, also, change the mirror substrate and coating materials. This last option is at the basis of the development of the innovative crystalline coating [63] which could bring a significant reduction of the Brownian noise [64]. A test on the performances of crystalline coating mirrors is reported in section 6.4.

2.5.2 Locking technique

In this section we will introduce the PDH locking technique and an evolution of such a method called Offset-sideband locking. The former is commonly used for the stabilization of the laser on an ultra-stable cavity (see sec. 3.3.5) while the latter is used, in particular, on the multi-wavelength cavity system (see chapter 4). The PDH technique, as well as the Offset-sideband locking, exploits the reflected light from the cavity of a resonant beam to generate an electronic signal (error signal) proportional to the frequency difference between the laser and the cavity mode. This signal is thus used to apply a feedback to the laser in order to stabilize its frequency.

Standard Pound-Drever-Hall technique

The reflected light is described by the *reflection coefficient* [65]:

$$F(\omega) = \frac{E_{ref}}{E_{\text{inc}}} = \frac{\sqrt{R}\exp\left(i\frac{\omega}{\Delta\nu_{\text{fsr}}}\right) - 1]}{1 - R\exp\left(i\frac{\omega}{\Delta\nu_{\text{fsr}}}\right)} \tag{2.37}$$

where E_{ref} and E_{inc} are the reflected and incident electric field (complex) of the beam respectively, ω is the laser angular frequency and R is the single mirror

reflectivity (considering idenical mirrors). When the laser is resonant with the cavity ($\omega = n\ 2\pi\Delta\nu_{\text{fsr}}$, n integer positive number) the reflected light from the first mirror and the leakage beam from the standing wave inside the cavity interfere destructively (same amplitude but π relative phase), giving $F(\omega) = 0$. On the other hand, if the light is not exactly on resonance (but close enough to build a standing wave) the relative phase between the two beams is no longer exactly π and thus part of the light is reflected back $\Big(F(\omega) \neq 0\Big)$. The reflection coefficient express also the phase of the reflected light which encodes the information about on which side of the cavity resonance the frequency is detuned. In other words, changing side changes the phase sign. In order to extract this phase information the input beam is firstly phase modulated to generate two sidebands:

$$E_{\text{inc}} = \sqrt{P_0}\exp\{\{i[\omega t + \beta\sin(t\Omega_{\text{PDH}})]\}\}$$

where P_0 is the optical power, Ω_{PDH} is the phase modulation angular frequency and β is the modulation depth. If we expand this expression at first order of β three components can be found: a carrier at $\omega = \omega_c$ and two sidebands at $\omega = \omega_c \pm \Omega_{\text{PDH}}$. When the laser is not perfectly at the resonance frequency, part of the carrier will be reflected from the cavity causing interference with the sidebands which are off resonance. This yields to a modulation of the reflected light power signal which can be expressed as [66]:

$$\begin{aligned} P_{\text{ref},\Omega_{\text{PDH}}} &= 2P_0 J_0(\beta)J_1(\beta)\times \\ &\times Re[F(\omega_c)F^*(\omega_c+\Omega_{\text{PDH}}) - F^*(\omega_c)F(\omega_c-\Omega_{\text{PDH}})]\cos(t\Omega_{\text{PDH}})+ \\ &+ 2P_0 J_0(\beta)J_1(\beta)\times \\ &\times Im[F(\omega_c)F^*(\omega_c+\Omega_{\text{PDH}}) - F^*(\omega_c)F(\omega_c-\Omega_{\text{PDH}})]\sin(t\Omega_{\text{PDH}}), \end{aligned} \tag{2.38}$$

with $J_n(x)$ the Bessel function of the first kind of order n. If the carrier frequency is close to the cavity resonance and the modulation frequency (Ω_{PDH}) is high enough to make the sidebands out of resonance, the term in eq (2.38) is purely imaginary and only the sine term survives. As a consequence of that, the reflected light signal contains a beat pattern generated by the interference of the carrier and the sidebands which carries the information about the phase of the reflected carrier.

To generate an adequate error signal the reflected light is collected by a fast photodiode. Its signal is then fed to a mixer that also takes a modulation frequency in the other input. The output of the mixer gives a signal oscillating at the frequency sum and the difference of the two input signals. If we demodulate the photodiode signal with the modulating frequency at Ω_{PDH} the frequency difference output will be a dc signal that can be isolated using a low pass filter.

The obtained error signal is proportional to δf, the frequency difference between the cavity resonance and the laser carrier:

$$\xi = D_{\text{PDH}}\delta f \tag{2.39}$$

where the linear constant D_{PDH} is called *frequency discriminant* and is:

$$D_{\mathrm{PDH}} = -\frac{16\mathcal{F}LP_0}{c} J_0(\beta)J_1(\beta). \tag{2.40}$$

This linear dependence is the fundamental feature used to control the laser frequency using a feedback loop.

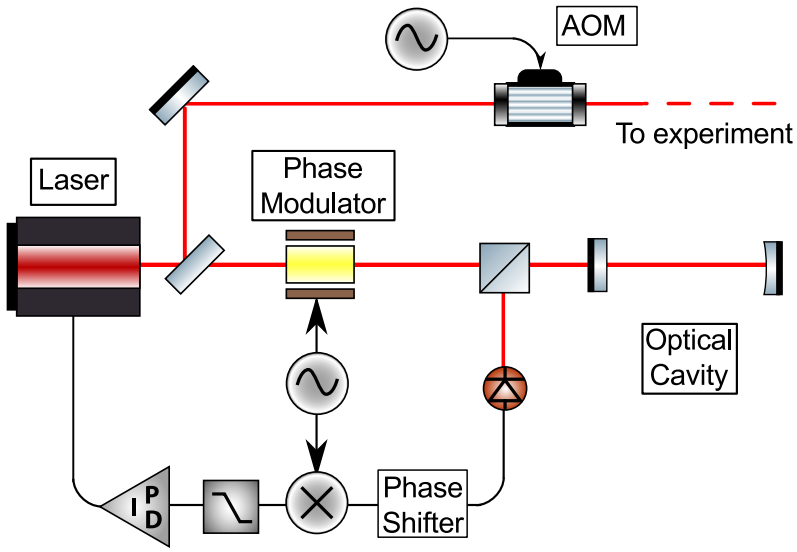

Figure 2.11: Sketch of the basic layout needed to implement the PDH techinque.

A typical experimental layout for implementing this technique is reported in fig. 2.11. The phase modulation is produced by an electro-optic phase modulator or a Pockels cell, while the reflected light is collected on a fast photodiode which measures the power $\left(\text{eq.}(2.38)\right)$. The electronic signal is demodulated at the modulation frequency $\left(\Omega_{\mathrm{PDH}}\right)$ using a frequency mixer and thus extracting the dc component with a low pass filter. A phase shifter ensures the right phase delay among the two signals to optimize the demodulation of the reflected light signal. A proportional-integral-derivative (PID) control loop takes the error signal and apply the correction to the laser frequency.

The cavity resonance frequency usually is different from the frequency actually needed by the experiment. To bring the stabilized laser frequency to the desired value a mirror of the cavity can be mounted on a piezo, thus varying the resonator length, at the cost of a reduced intrinsic stability. Alternatively, additional frequency modulators, such as AOMs, can be adopted. In this way the stability is not affected but the optical layout gets more complex along with a higher energy consumption.

Offset-sideband locking technique

The fundamental concept behind the offset-sideband locking technique is to lock a sideband of the modulated laser beam, instead of the carrier, to the cavity and thus being able to move its frequency in order to match the experimental value. To make this possible a broadband phase modulator is driven by a phase modulated RF signal:

$$E_{\mathrm{OSB}} = E_o \exp\{i[\omega_c t + \beta_1 \sin\left(\Omega_{\mathrm{gap}} t + \beta_2 \sin(\Omega_{\mathrm{PDH}} t)\right)]\}. \tag{2.41}$$

The main modulation has Ω_{gap} angular frequency and β_1 modulation depth, it generates a first set of sidebands at $\omega_c \pm \Omega_{\mathrm{gap}}$ with amplitude $J_0(\beta_1)J_1(\beta_1)$. Tuning Ω_{gap} allows to bring the sideband in resonance with the cavity while keeping the carrier ω_c at the required experimental frequency. Besides, the further phase modulation with angular frequency Ω_{PDH} and β_2 depth, gives an additional set of sidebands at $\omega_c \pm \Omega_{\mathrm{gap}} \pm \Omega_{\mathrm{PDH}}$ with amplitude of $J_1(\beta_2)J_1(\beta_1)$. When $\Omega_{\mathrm{gap}} >> \Omega_{\mathrm{PDH}}$ the PDH sidebands behaves like in the normal PDH case giving an error signal proportional to δf and with a frequency discriminant of:

$$D_{\mathrm{OSB}} = \frac{16\mathcal{F}LP_0}{c} J_1^2(\beta_1)J_0(\beta_2)J_1(\beta_2). \tag{2.42}$$

Experimentally the phase modulation is made by a broadband electro optic modulator piloted by a RF produced by a synthesiser capable of phase modulation. The EOM bandwidth have to be at least half of the $\Delta\nu_{\mathrm{FSR}}$ to cover continuously the frequency range interested by the experiment. Using this technique the additional modulators needed for bridging the resonance and the experimental frequency as well as a piezo cavity are no longer necessary resulting in a simpler and flexible experimental layout.

2.6 Stability limits of an optical lattice clock

The high frequency stability provided by the simultaneous interrogation of many quantum absorbers constitutes one of the main advantages of optical lattice clocks. However, several effects can limit this figure of merit far from reaching its fundamental limit represented by QPN.

Taking back eq. (1.2) and expanding the signal-to-noise ratio term (S/N) we obtain [67]:

$$\sigma_y(\tau) = \frac{1}{\pi Q}\sqrt{\frac{T_c}{\tau}}\left(\frac{1}{N} + \frac{1}{Nn_{\mathrm{ph}}} + \frac{2\sigma_N^2}{N^2} + \gamma\right)^{1/2}. \tag{2.43}$$

In this equation Q is the spectroscopy line quality factor, τ is the measurement duration, T_c is the clock cycle time, N is the number of atoms involved in the

measure while σ_N is its RMS fluctuations, n_{ph} is the number of photon detected and γ comes from the frequency noise of the clock laser.

The fist term in parenthesis in eq. (2.43) scales as $1/N$ and is the QPN. The second and third terms comes from the photon shot noise of the fluorescence and the fluctuation of number of atoms in each cycle, respectively. These two contribution are kept well below the QPN limit by operating the state readout saturating the $^1\mathrm{S}_0 - ^1\mathrm{P}_1$ transition and using the electron shelving technique (see sec. 5.1.5). In this way many photons per each atoms are collected and the signal is normalized on the total number of trapped atoms in each cycle. Finally, the last term is a technical noise coming from the clock laser frequency noise and represents the major limit to the clock stability. It is called Dick Effect [68].

2.6.1 The Dick Effect

In an optical lattice clock the frequency of the local oscillator, i.e. the clock laser, is referred to the atomic transition by cyclic interrogations (see. chapter 5). When the clock laser is locked to the atoms its long term instability is compensated and enhanced by the atoms, thus realizing a frequency standard. However, the sequential clock operation, composed by periods where the clock laser interrogates the atoms and periods needed to prepare them in the right quantum state, introduces a 'dead time' in the measurement. This gives rise to an aliasing effect where the high frequency noise of the local oscillator is down-converted at Fourier frequencies close to the inverse cycle time $1/T_c$ and is improperly compensated by the frequency tuning process thus limiting the long term instability.

The effect depends on the fraction of the dead time T_d in the cycle period T_c, where the clock is not referred to the atoms hence free running, as well as the frequency noise spectrum of the laser $S_\nu(f)$ and the spectroscopy technique used to interrogate the atoms (Rabi or Ramsey). The Dick noise instability component of an oscillator locked to the atoms reads [69]:

$$\sigma_y^2(\tau) = \frac{1}{\tau g_0^2} \sum_{m=1}^{\infty} |g_m|^2 S_\nu\Big(\frac{m}{T_c}\Big). \tag{2.44}$$

where $S_\nu\left(\frac{m}{T_c}\right)$ is the frequency noise power spectral density of the probe laser at Fourier frequencies corresponding to the harmonics of the inverse of the cycle time. The parameter g_m,

$$g_m = \frac{1}{T_c} \int_0^{T_c} g(t) e^{-2\pi i m t/T_c} dt \tag{2.45}$$

expresses the Fourier coefficients of the sensitivity function $g(t)$, which encodes the impulse response of the atomic system to a frequency change occurring at time t. g_0 is the mean value of $g(t)$ over a cycle time. The sensitivity function is the fundamental parameter that can be used to minimize the aliasing effect, it

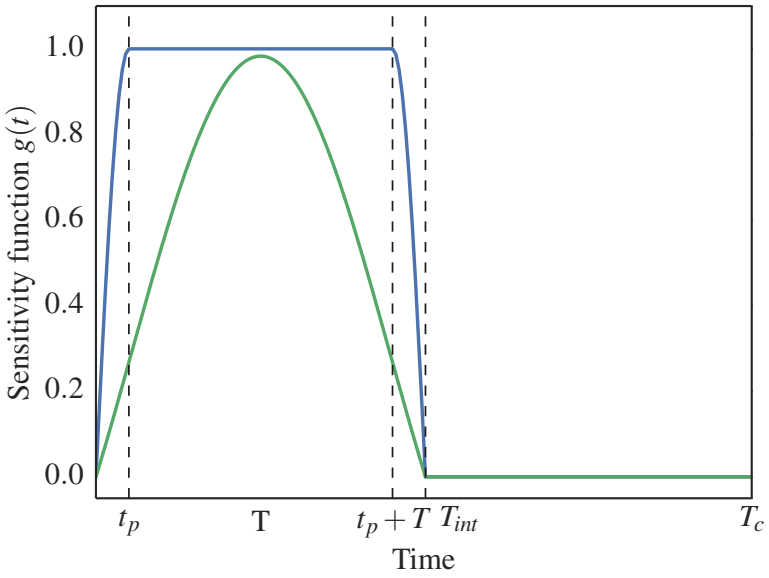

Figure 2.12: Sensitivity function for Rabi (green) and Ramsey (blue) spectroscopy, calculated using eq.(2.46) and eq.(2.47) respectively with T_c cycle time, T_{int} interaction time, t_p pulse time and T dark time.

is calculated for the different interrogation schemes and for a Rabi π-pulse with duration t_p it is [70]:

$$g(t) = \frac{\Delta\omega}{(1+\Delta\omega^2)^{3/2}}[\sin\Omega_1(t)(1-\cos\Omega_2(t)) + \sin\Omega_2(t)(1-\cos\Omega_1(t))] \tag{2.46}$$

where $\Delta\omega$ is the detuning used to generate the lock error signal, $\beta = \pi\sqrt{1+\Delta\omega^2}$, $\Omega_1(t) = \beta t/t_p$ and $\Omega_2(t) = \beta - \Omega_1(t)$.

For a Ramsey interrogation with two $\pi/2$ pulses (i.e. $\Omega t_p = \pi/2$) separated by a dark time T the sensitivity function is [69]:

$$g(t) = \begin{cases} a\sin(\Omega t) & 0 \le t \le t_p & \text{First pulse} \\ a & t_p \le t \le t_p + T_d & \text{Dark time} \\ a\sin(\Omega[T_d + 2t_p - t]) & t_p + T \le t \le T + 2t_p & \text{Second pulse} \\ 0 & T + 2t_p \le t \le T_c & \text{Dead time} \end{cases} \tag{2.47}$$

with $a = -\sin(\Delta\omega T_d)$. The two functions are shown in fig. 2.12.

In the case of Ramsey spectroscopy with duty cycle close to 50 % the instability expressed in 2.44 can be expressed as:

$$\sigma_{y\ \text{Dick}} \approx \frac{\sigma_{y\ \text{osc}}}{\sqrt{2\ln 2}}\sqrt{\frac{T_c}{\tau}}\left|\frac{\sin(\pi T/T_c)}{\pi T/T_c}\right| \tag{2.48}$$

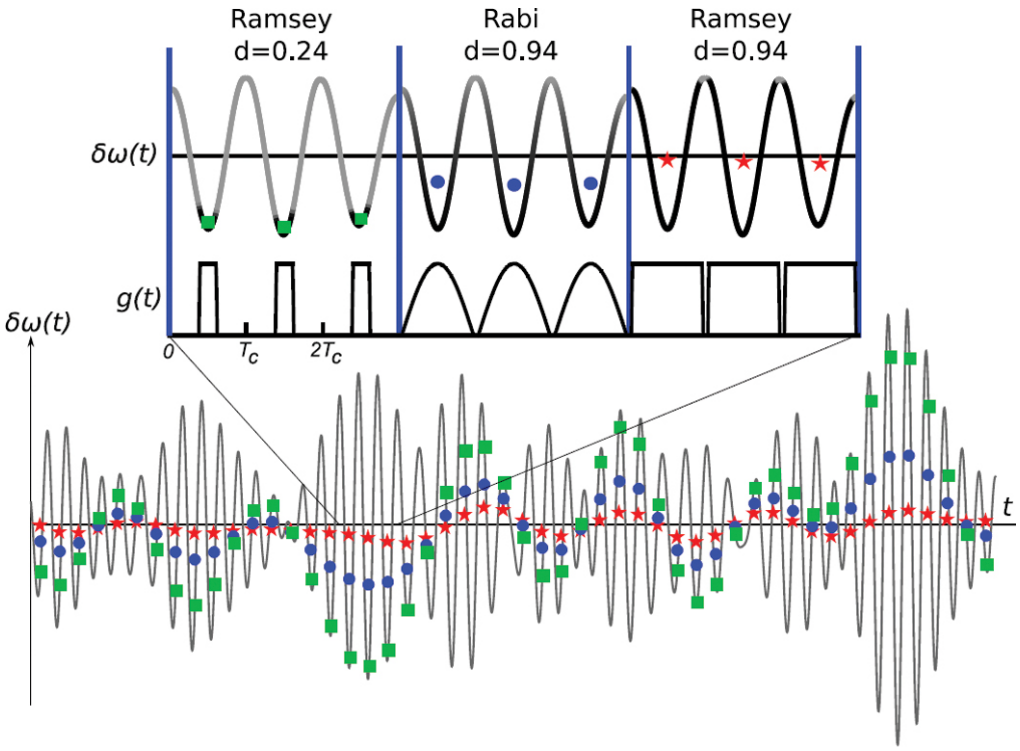

Figure 2.13: Example of the aliasing effect for different spectroscopy techniques. $\delta\omega$ represents an example of frequency noise component close to $1/T_c$. The points show the resulting frequency noise for different spectroscopy techniques and different duty cycles d. From [71].

where $\sigma_{y\ \mathrm{osc}}$ is the clock laser instability calculated from the frequency noise spectrum S_ν.

Figure 2.13 quantitatively illustrates the effect of the aliasing effect when different parameters of the probing pulses are varied. It can be seen that larger interrogation time (i.e. larger duty cycle $d = T_{\mathrm{int}}/T_c$) leads to a better average of the laser frequency noise component which yields to a smaller displacement of the resulting point meaning smaller sensitivity to the Dick noise. On the other hand, the different sensitivity functions for the Raby or Ramsey interrogations bring to different results. Given the different shape of its sensitivity function, the Ramsey scheme gives better rejection of the Dick noise compared to the Rabi case at the same duty cycle d. Moreover, in the case of Rabi interrogation with d close to 1 a residual aliasing is still present due to the shape its sensitivity function. This can be also seen in fig. 2.13, in fact comparing interrogations with the same duty cycle but with different spectroscopy techniques shows that Ramsey gives a lower noise (red stars) compared to Rabi (blue cycles).

Chapter 3

INRIM ytterbium optical lattice clock setup

An optical lattice clock based on ytterbium (Yb) atoms is operating in the Time and Frequency laboratories of the Istituto Nazionale di Ricerca Metrologica (INRIM) in Turin. This frequency standard exploits an ultra-stable laser at 578 nm, frequency locked to the $^1S_0 \rightarrow {}^3P_0$ double forbidden atomic transition of the ^{171}Yb isotope which constitutes a secondary representation of the SI second under CIPM recommendations [30].

In this chapter the experimental layout of the experiment is reported together with the description of the laser sources needed to operate the clock. Currently, the frequency stabilization of the MOT and lattice lasers is done using the multi-wavelength cavity, which is described in chapter 4. However, before its implementation other methods were adopted, these are here illustrated as well. An exhaustive description of the experimental layout can be found in [72].

3.1 Vacuum system and atomic oven

Ultra-high vacuum is necessary to perform the required atomic manipulation and to achieve an adequate lifetime of the trapped atoms in the lattice potential. In this experiment the vacuum system has a horizontal structure with axial symmetry, consisting in an experimental chamber joint together with an atomic effusive oven (see figs. 3.1 and 3.2) with several others standard stainless steel fittings.

The experimental, or main, chamber is where the atoms are cooled, trapped and interrogated and consists in a custom machined piece of aluminium, featuring an octagonal shape and large apertures for an optimal optical access. Anti-reflective windows close the apertures, or view ports, sealed with an indium wire which reduces the mechanical stress, thus reducing the induced birefringence in the glass. In total there are six lateral windows (40 mm diameter) while two larger view ports

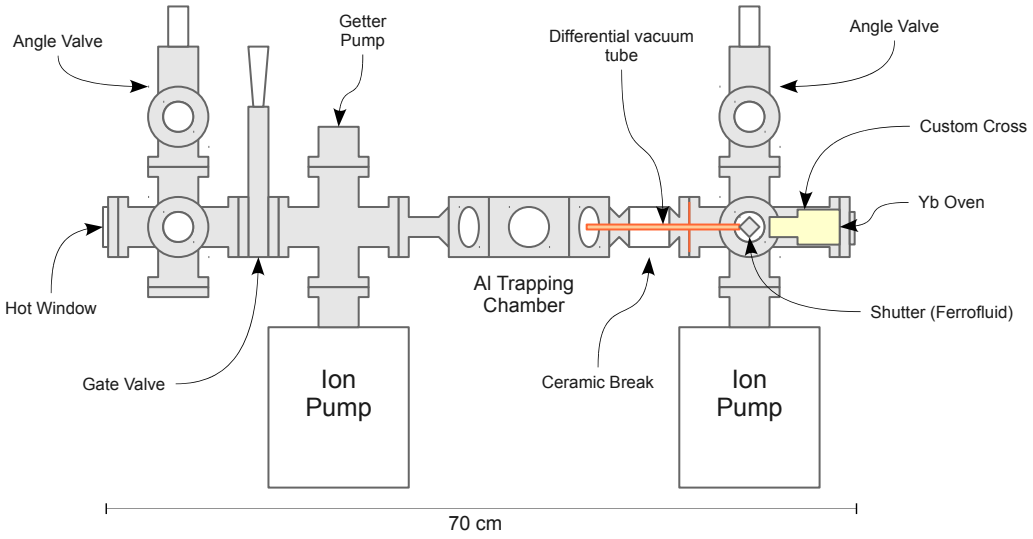

Figure 3.1: Sketch of the vacuum system layout with the main components. From [72].

(70 mm diameter) are present on top and on bottom of the chamber.

The atomic oven its an effusive system where a cartridge, filled with Yb nuggets, is heated up to 400 °C. The hot Yb vapour is collimated to form an atomic beam by a stainless steel tip with a multichannel array made by 37 capillaries with internal diameter of 280 µm and 8 mm of length (see fig.3.3). A commercial power supply used as current generator to heat the oven. The typical current required is about 1.4-1.8 A.

The vacuum is independently maintained in the oven region and in the experimental chamber by two dedicated ion pumps (Agilent VacIon 40) operating at a speed of 40 L/s. Additionally, to improve the vacuum quality on the experimental side, a non-evaporable getter pump (Saes D50) is installed. Since the hot oven limits the utmost pressure achievable, a differential vacuum tube is installed between the oven and the main chamber which maintains a pressure difference and, at the same time, allows the atomic beam to get into the experimental side of the system. This tube is 120 mm long and has a radius of 2.5 mm, further details can be fund in [72]. The vacuum level achieved in the experimental region is 6×10^{-10} mbar while in the oven side is about 2×10^{-8} mbar.

This system is designed to have the oven quite close to the experimental chamber in order to maximize the atomic flux in the trapping region. The distance between the oven tip and the centre of the main chamber is 21 cm. As a consequence of that, the clock can operate without a Zeeman slower ([73]) resulting in a significative experimental simplification.

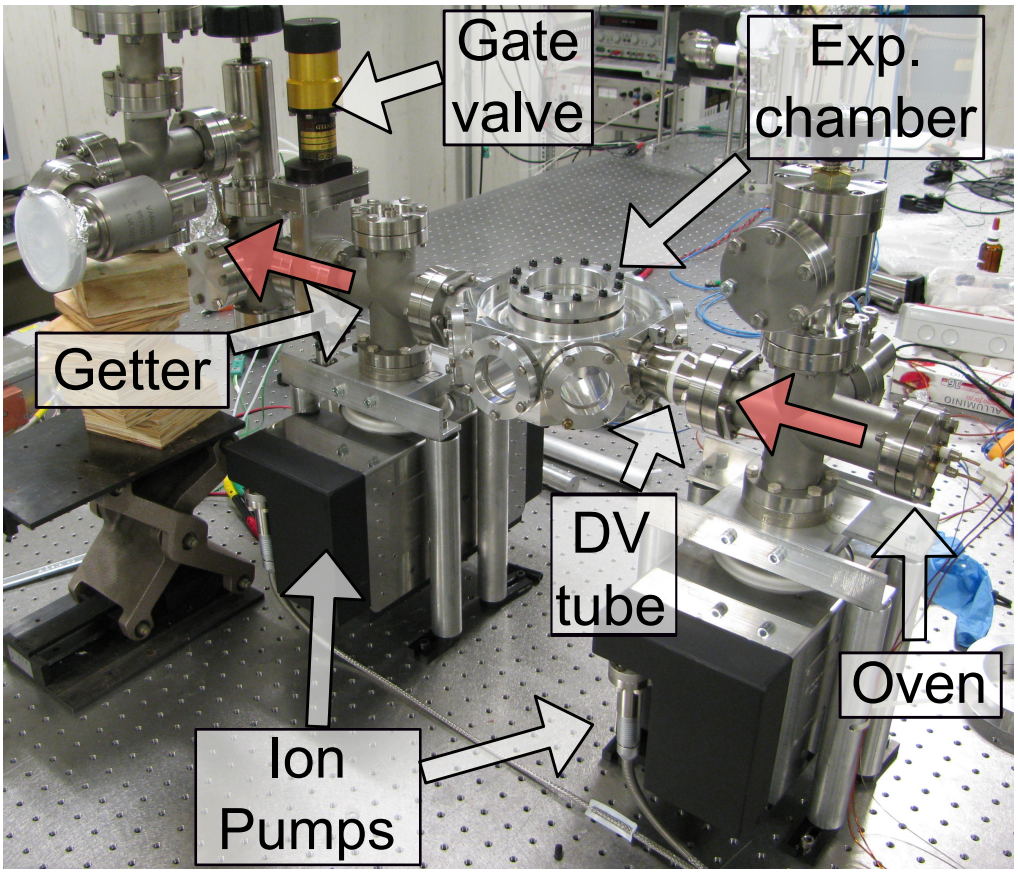

Figure 3.2: Picture taken during the assembly of the vacuum system showing, in particular, the experimental chamber, the atomic oven and the two ion pumps. Red arrows show the atomic beam axis of propagation while DV tube means differential vacuum tube.

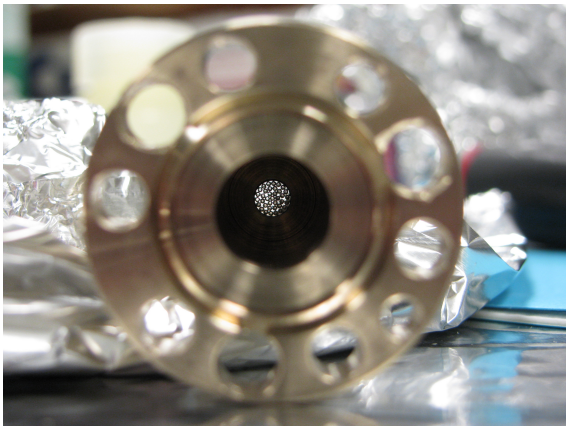

Figure 3.3: Picture of the oven tip with the detail of the multichannel array.

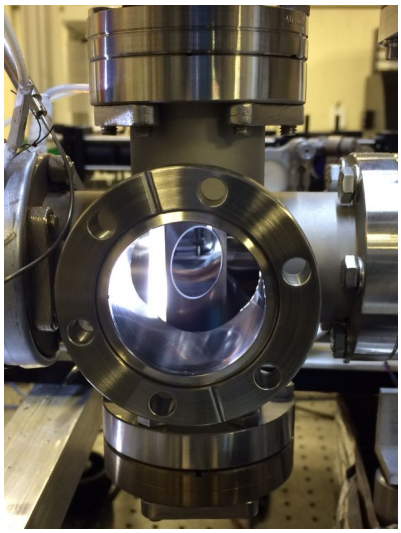

Figure 3.4: Picture of the new mirror installed inside the vacuum system. The atomic beam comes from the right hand side of the picture.

On the opposite side of the oven, beyond the main chamber, the optical access for the slower beam is realized. Originally, the vacuum fitting was closed, on the atomic beam axis, by a sapphire window. It was kept at 230 °C to avoid metallic Yb deposition on the inner face, thus maintaining a good optical transmission at the slower beam wavelength of 399 nm. To improve the black-body radiation shift evaluation (see section 5.3.4), this part has been replaced during 2016 in favour of an intra-vacuum mirror, positioned with a $\sim 45°$ angle with respect the atomic beam axis in order to let the laser beam enter from a lateral view-port and avoiding the direct sight of the trapping region (see fig. 3.4). Between the main chamber and the intra-vacuum mirror a gate valve is present that can be closed to maintain the vacuum in the experimental chamber in the case of a maintenance service on the mirror.

In the oven region, a motorized shutter is installed to prevent the atomic beam to get into the experimental chamber during spectroscopy. It is copper made with a diapason-like shape and its rotation determines the passage of the atomic beam. The mechanical transmission of the rotation is provided by a magnetic joint which couples with the intra vacuum shutter with the motor outside. This system is still under development an it is not operative yet.

3.2 Magnetic fields

The magnetic field gradient needed to generate the MOT is provided by a pair of magnetic coils, mounted along the vertical axis (z axis) around the larger top-bottom windows of the experimental chamber, and operated in anti-Helmholtz

configuration. The chopper wire used to build the coils has a rectangular section (3 mm×1 mm) and is rolled up an aluminium support with hollow core for water cooling. The MOT coils are piloted by a computer controlled power supply, capable to deliver up to 15 A which correspond to a magnetic field gradient of 0.35 mT/m. Fig. 3.5 shows the experimental chamber with all the magnetic coils.

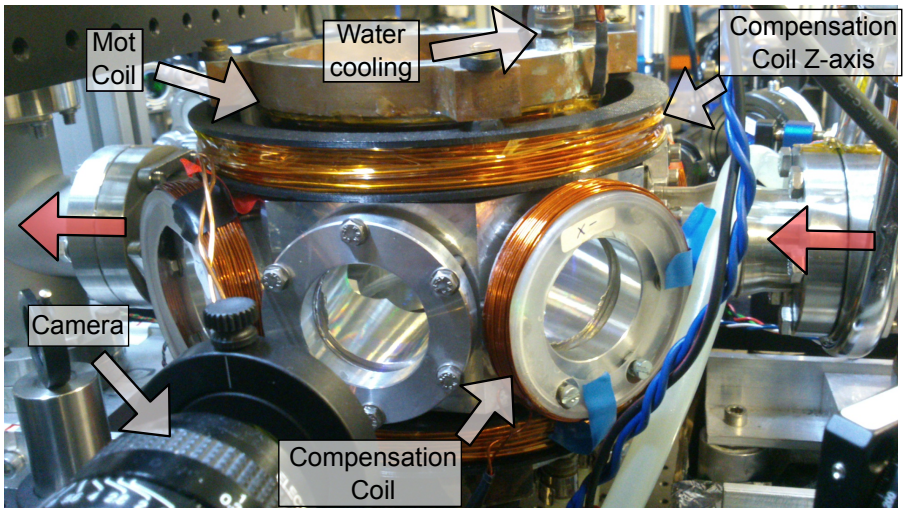

Figure 3.5: Detail of the experimental chamber with the magnetic coils mounted on. The red arrows indicates the propagation of the atomic beam.

To compensate for stray magnetic fields, three pairs of anti-Helmholtz compensation coils are installed along the three orthogonal axis of the chamber. In the horizontal axis (x and y), the chopper wire is winded on a plastic holder, mounted around 4 lateral view-ports and piloted by a calibrated current generator (Agilent E3631A). For the z axis a pair of larger windings coiled up 3D printed holders and mounted around the MOT coils (see fig. 3.5). The power supply which drives these coils is custom made and it is remotely controlled by the computer.

Lastly, to reduce the magnitude of stray magnetic field generated by the ion pumps, these are enclosed in a layer of high permeability, g-iron shield.

3.3 Laser generation

In the Yb optical lattice clock many different laser radiations are used to manipulate and interrogate the atomic sample as introduced in chapter 2. To generate laser light at these particular wavelengths, spread across almost the entire visible spectrum, several non-linear optics techniques are implemented[74]. Second harmonic generation (SHG) is used to produce 399 nm and 556 nm light. It is based on the production, inside a non-linear crystal, of a photon with twice the frequency of the incoming ones. Sum frequency generation (SFG) is used to generate the

clock laser at 578 nm, alternatively to SHG. In this case two photons with different frequency ν_1 and ν_2, interacting in a non linear crystal, result in a third photon with frequency $\nu_3 = \nu_1 + \nu_2$.

3.3.1 399 nm Laser

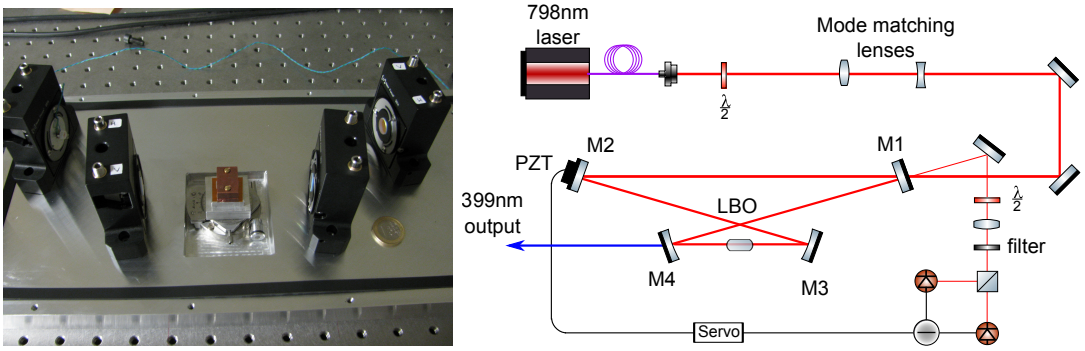

Figure 3.6: Picture of the doubling enhancement cavity with the sketch of the optical layout.

The 399 nm laser, used for cooling down the atoms from the atomic beam and for the first stage of the MOT ($^1S_0 \rightarrow {}^1P_1$ transition), is generated by SHG of a 798 nm laser by means of a lithium triborate (LBO) crystal inside an enhancement four-mirrors bow tie cavity [75]. The cavity increases the circulating optical power through the crystal improving the efficiency of the process. The crystal is made by Raicol and has a section of 1.5 mm × 1.5 mm and is 15 mm long. It is mounted on a rotational stage between M3 and M4 (see fig. 3.6).

The 798 nm input laser is a commercial tapered amplified diode laser (Toptica), capable to deliver up to 3 W. The output light is fiber coupled and it is sent to the doubling cavity where the beam is mode matched by two lenses before getting in. The cavity length is controlled by a mirror mounted on a piezoelectric transducer (M2) and it is servoed using a feedbeck loop based on the Hänsch-Couillaud technique [53]. The typical input power to the cavity is about 1.3 W of 798 nm light which results in 400 mW of UV laser light output.

Alternatively, the 798 nm radiation can be provided by a Ti:sapphire laser (Coherent MBR-110) pumped with 8 W of 532 nm laser provided by a solid state pump laser (Coherent Verdi-V8). This laser can be frequency tuned between 700 nm and 970 nm with an output power at 798 nm of 1.3 W. This laser was originally used on the system and it was replaced by the diode laser during 2016. Currently it is kept as backup solution in case of technical problem.

The 399 nm light is distributed to three different branches namely the slower line, the MOT line and the detection line. Each line features a dedicated frequency modulator (AOM), mode matching lenses and optical shutter. The slower beam

demands the highest optical power in order to maximize the number of trapped atoms, typically 250 mW are sent through this line, limited by the optical fiber radiation damage. We send about 100 mW in the MOT line and 50 mW to the detection beam.

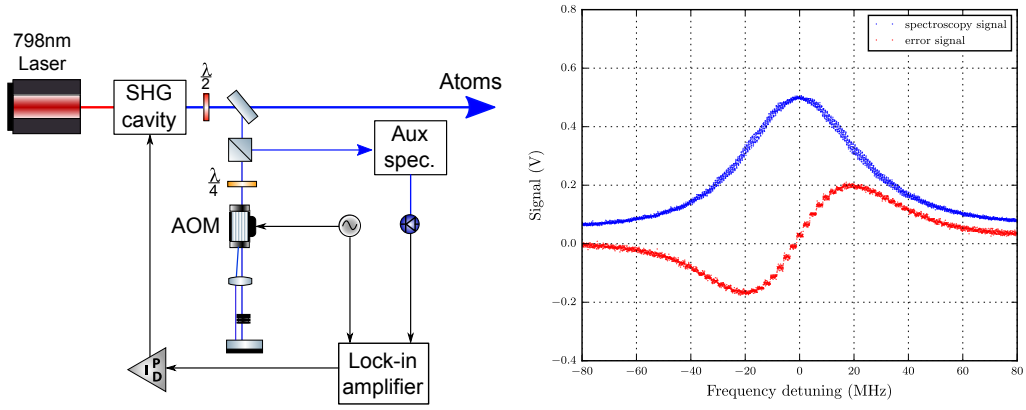

Figure 3.7: Left: scheme for frequency stabilisation on a spectroscopy atomic resonance signal. Right: spectroscopic feature of ^{171}Yb at399 nm as seen from the transverse spectroscopy signal (blue trace) and corresponding error signal used to lock the laser frequency (red trace). From [76].

Frequency lock to the spectroscopy feature Given the linewidth of the $^1S_0 \rightarrow {}^1P_1$ transition about 29 MHz, the frequency stabilization for the 399 nm laser is meant to compensate the laser drift and the laser linewidth less than 1 MHz. To operate the clock are required a linewidth and a daily drift of less than 1 MHz. To frequency stabilize the blue laser we exploit an atomic resonance as reference. We perform transverse spectroscopy using a separate auxiliary Yb oven. To avoid Doppler shifts, the blue light is frequency modulated by a double pass AOM [77], sent perpendicular to the atomic beam and back-reflected while the fluorescence is detected by a photodiode mounted on the transverse plane, perpendicular to the 399 nm. A lock-in amplifier takes the fluorescence and the modulation signals and generates the error signal (see fig. 3.7). A PID control takes this signal and closes the loop acting on the piezo transducer of the 798 nm laser.

This system was used during the absolute measure campaign presented in section 5.4. The frequency stabilization of the 399 nm has then been upgraded at the end of 2016 and it is currently done using the simpler, more compact and flexible set up of the multi-wavelength cavity (see chapter 4).

3.3.2 556 nm Laser

This laser lies in the green region of the visible spectrum, it is used for the second MOT stage ($^1S_0 \rightarrow {}^3P_1$ transition) and it is produced by SHG in a periodically-poled potassium titanyl phosphate (PPKTP) crystal from a 1112 nm laser. The crystal is 20 mm long, held inside a small oven kept at 46 °C to have the correct phase-matching condition, and mounted on a translational stage to get the optimal alignment.

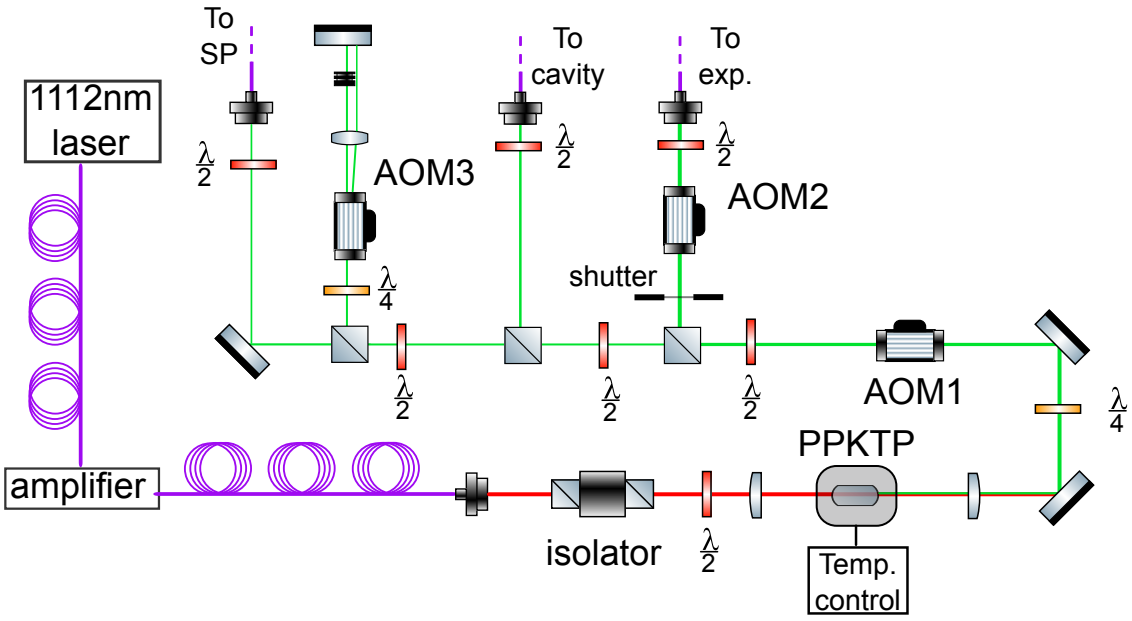

Figure 3.8: Layout of the 556 nm laser generation and distribution. In purple are optical fibers, the coils represent paddles used to control the polarization of the infra-red light. SP is spin polarization.

The input laser source is a doped fiber laser (NKT-Koheras Adjustik) amplified by a fiber amplifier (Keopis Benchtop) up to 1.3 W of optical power. The frequency conversion is made in single pass through the crystal with an efficiency of 1.5 %. The total 556 nm output power can go up to 10 mW and is divided in three parts: the MOT line, the spin polarization line and the cavity line (see fig. 3.8). The distribution layout features a first frequency modulator (AOM1), used for the frequency stabilization, before being divided while the MOT line has a dedicated frequency modulator (AOM2) and a mechanical shutter. The spin polarization distribution branch has a frequency modulator (AOM3) mounted in a double-pass fashion for a larger frequency span operation. The MOT line requires about 2 mW while 200 µW for the stabilization cavity and 500 µW for the spin polarization line are sufficient.

Frequency stabilization is necessary and more stringent compared to the 399 nm one. The required linewidth and daily drift is less than 100 kHz. To do so the

laser is frequency referenced to an optical cavity, made in ULE (both mirrors and spacer) with a horizontal design featuring a notched cylinder spacer 10 cm long. This resonator was already described and characterized in [59]. The frequency is locked with the PDH technique using a circuit analogous to the one used on the clock laser and presented in sec. 3.3.5, with a bandwidth of 120 kHz. The system was upgraded to the multi-wavelength cavity after the 2016 characterization. This cavity has been adopted as ultra-stable cavity for the clock laser as reported in the upgrade of the clock laser section (sec. 3.3.5).

3.3.3 759 nm Lattice Laser and Repumper

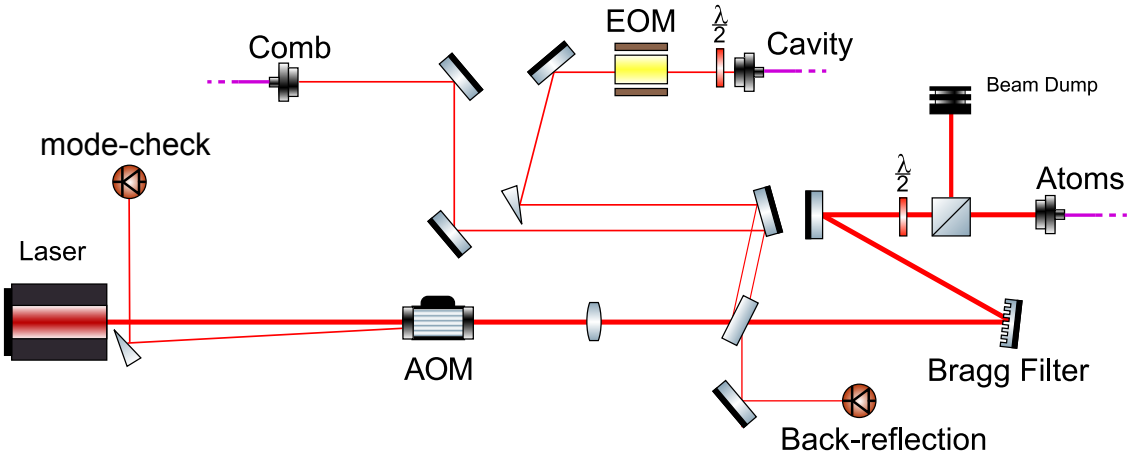

Figure 3.9: Optical layout of the lattice laser distribution.

The lattice 759 nm laser is a commercial Ti:Sapphire (M2 SolsTiS) pumped with a 10 W, 532 nm light provided by a diode-pumped solid state laser (Lightouse Photonics Sprout-D). The total output is about 2.4 W with a linewidth below 20 kHz and it distributed, apart from the experiment, to three auxiliary lines. One to the multi-wavelength cavity for frequency stabilization, the second one is used to send the light to the optical frequency comb for absolute frequency measure while the third branch, exploiting the reflected light coming from the AOM, send the light to a fast photodiode used to monitor the single mode operation of the laser (see figure 3.9). A second photodiode is installed to detect the back-reflected light coming from the retro reflector on the experimental bench.

During the light shift characterization measurements the multi-wavelength cavity was not operative yet and the lattice laser slow frequency drift was compensated by locking the laser to the frequency comb. The beatonte frequency between the lattice laser and the comb tooth was counted using a frequency counter connected to a PC that also calculated the required frequency correction. The PC gave a digital output that was converted to an analogue signal with a DAC and then sent

to the laser's cavity piezo transducer. Given a counter gate time of 1 s, the system was capable to make about one frequency correction per second.

During 2017 the system has been upgraded with a new volume Bragg filter (OptiGrade) mounted before the fiber to the experimental chamber. This filter further suppresses the amplified spontaneous emission (ASE) with a bandwidth of $\delta\lambda < 0.1$ nm.

Regarding the repumper laser, it is a commercial 1389 nm pigtail distributed feedback (DFB) diode laser (NKT-photonics) with an output power of 10 mW. Its frequency does not need to be frequency stabilized since the $^3P_1 \rightarrow ^3D_1$ transition is power broadened to 300 MHz. The chip is placed inside a wooden box to reduce air currents and thermal fluctuations, the light is delivered to the experimental table via optical fiber.

3.3.4 579 nm Clock Laser

The clock laser at 579 nm can be produced by means of two different techniques. The first implementation on the Yb clock exploited the SFG from two infra-red lasers which, at the time of the system design, provided more power compared to the SHG technique. The clock was operated using this set up during the characterization campaign illustrated in chapter 5. However, it is now easier and more convenient to generate 579 nm radiation by SHG from a single 1156 nm laser. This upgrade started at the end of 2016 and the first results are presented in section 5.2.

Generation by SFG The clock laser radiation at 578 nm is generated by SFG in a waveguide PPLN from two infra-red lasers: a 1030 nm erbium fiber laser (NP Photonics Rock Laser) and a neodymium-doped yttrium aluminium garnet (Nd:YAG) at 1319 nm (Lightwave Photonics model 126) (see fig. 3.11).

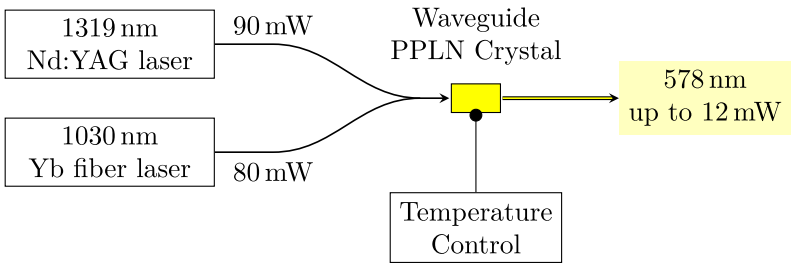

Figure 3.10: Scheme of the experimental apparatus of the sum frequency generation of 556 nm laser light. From [72].

The waveguide, produced by HC Photonics, has 32 channels. It is temperature controlled to maximize the conversion efficiency and mounted on a precision 3-axis translational stage for optimal alignment. The two infra-red lasers are combined in

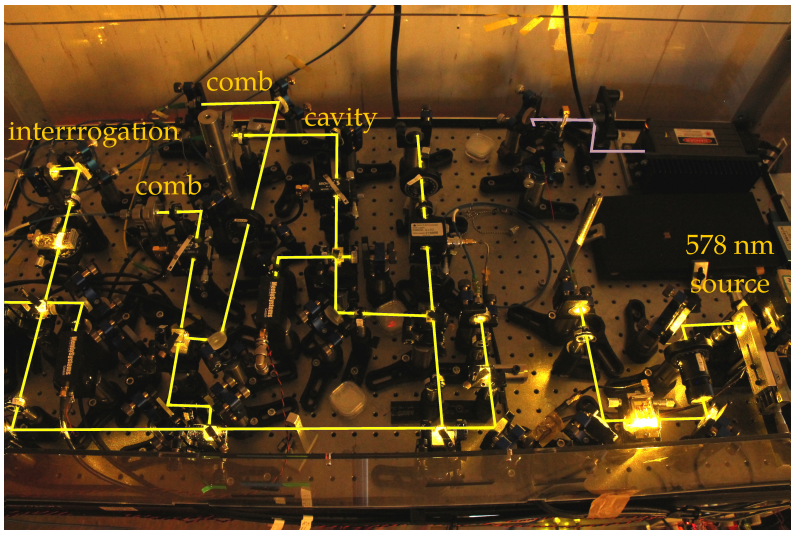

Figure 3.11: Optical table used for generation and distribution of 578 nm radiation. From [76].

a Y-shaped fiber coupler and its output, which is just the bare fiber placed close to the crystal, is coupled to one of the active channels. Typically 12 mW of yellow light is produced from 80 mW of 1030 nm laser and 33 mW of 1319 nm laser. At the crystal output a microscope objective collimates the yellow light and, after passing through a first AOM for frequency stabilization, is fiber coupled to clean the beam spatial mode and also for a more robust optical distribution.

The light is then distributed to the ultra-stable cavity, to the frequency comb and to the experiment (see fig. 3.11). Every line features a double-pass AOM to control the frequency of the laser and a second AOM used for the fiber noise cancellation and the power stabilization.

Generation by SFG The new implementation of 578 nm laser generation features a quantum-dot diode laser (Toptica DL-PRO) frequency doubled by a fiber coupled waveguide PPLN crystal (NTT Photonics). The crystal is enclosed in a dedicated package (see fig. 3.12) containing a peltier, a thermistors and fiber coupling lenses. The temperature stabilization is made by a commercial PID control (Thorlabs). The diode laser output is directly fiber coupled and reaches the doubling crystal without any passage through the air. The crystal temperature is tuned to maximize the doubling efficiency, at $\approx 28.5\,^{\circ}\mathrm{C}$ we got 5.2 mW out of 57 mW of infra-red light. The distribution of the light remains analogue to what reported above.

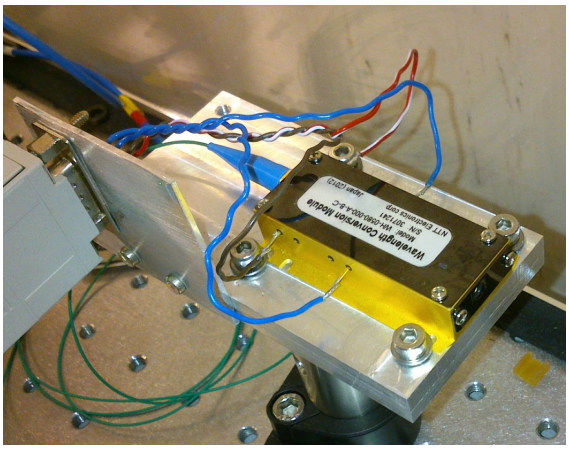

Figure 3.12: Picture of the waveguide PPLN crystal mounted on a custom holder. The input fiber can be seen in the left side of the picture while the electrical wires are used to read the thermistors and operate the peltier.

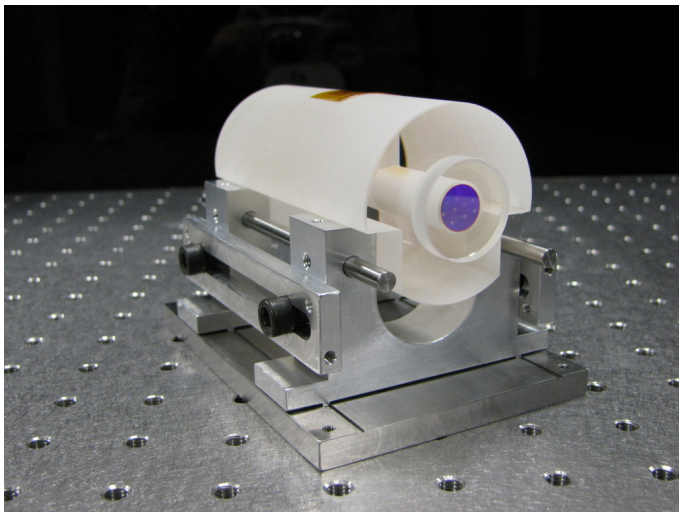

Figure 3.13: Picture of the ultra-stable cavity on the special holder before being mounted into the vacuum chamber. From [72].

3.3.5 INRIM ultra-stable cavity

The 578 nm laser is stabilized to an ultra-stable horizontal Fabry-Perot optical resonator, using the PDH technique. The cavity is 10 cm long ($\Delta\nu_{\mathrm{FSR}} = 1.5\,\mathrm{GHz}$) featuring a notched cylinder spacer made of ULE and fused silica mirrors with dielectric coating and ULE compensation rings (see fig. 3.13). The mirror geometry is flat-concave with a radius of curvature of $-0.5\,\mathrm{m}$. It has a measured finesse of 144 000(2000). The cavity is supported by a 4 points aluminium mounting with Viton pads, specifically designed to suspend the resonator on the Airy points. The

cavity with its holder are enclosed in a copper thermal radiation shield, then inserted in a steel vacuum chamber where it is held in place by 4 ceramic and 4 nylon screws that minimize thermal coupling between the shield and the chamber. The vacuum pressure is below 1×10^{-4} Pa, maintained by a dedicated ion pump. Two flexible heaters are installed on the vacuum steel external chamber walls while the temperature is monitored by two negative temperature coefficient (NTC) thermistors placed on the cavity support and on the thermal shield. The temperature is actively stabilized using the active disturbance rejection control [78] at the zero CTE that is, for this cavity, at 28 °C.

To isolate the system from vibrations, the vacuum chamber, together with the optical set up needed to realize the lock, are mounted on a passive anti-vibration platform (Minus-k BM8) and then it is arranged in an acoustic isolation chamber.

From equation (2.36) the expected thermal limit of the cavity can be computed. Considering the fused silica mirror substrates we have $E = 7.2 \times 10^{10}$ Pa, $\sigma = 0.17$, $\phi_{\text{sub}} = 1/(3 \times 10^6)$. For the coating we have $\phi_{\text{coat}} = 4 \times 10^4$, a thickness d of 2 µm. With a cavity length L of 10 cm, a laser beam waist on the mirrors of $\omega_0 = 190$ µm and an operational temperature of 301 K we found a thermal noise limit on the instability of the resonator of $\sigma_{\text{therm}} = 3.47 \times 10^{-16}$.

In addition to all the aforementioned effects, the long term mechanical stability of the cavity is linked to the mechanical relaxation of the glass spacer as well as the mirror substrates. As a consequence, the cavity tends to reduce its length with time and this translates in a long term drift on the laser frequency. The cavity resonant frequency has been kept under control by measuring it using an optical frequency comb. The drift at the time of the clock characterization was about 5 kHz per day, meaning less than 0.1 Hz per second.

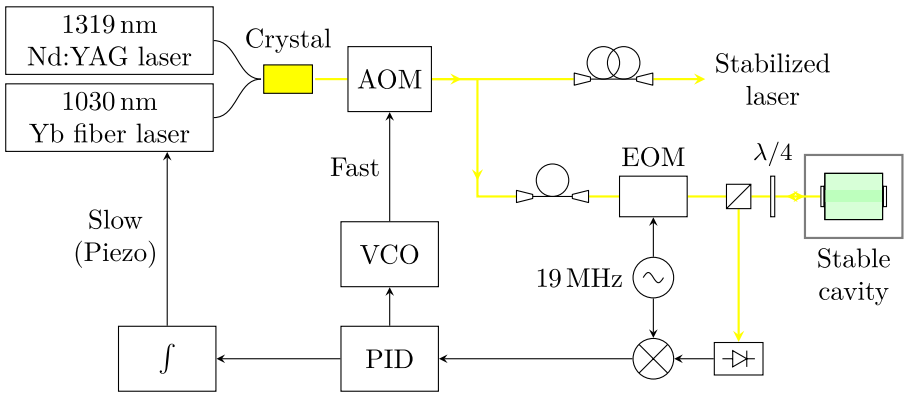

Figure 3.14: Sketch of the realization of the PDH lock of the clock laser. From [72].

Frequency lock The optical layout is retorted in fig. 3.14, 578 nm light is sent to the acoustic chamber via optical fiber, about 6 µW are coupled into the TEM_{00}

mode of the cavity. The phase modulation needed to generate the frequency sidebands is provided by an EOM piloted by a 19 MHz RF while the transmitted and the reflected light from the cavity are detected by two photodiodes mounted on the cavity breadboard. The frequency lock is made by means of the PDH technique with a double-integrator servo with two separate feedback channels. One channel is used to make a fast lock acting on an AOM in double pass while the second channel is used to compensate for slower frequency variation by acting on the piezo of the 1030 nm laser. The control bandwidth is about 120 kHz.

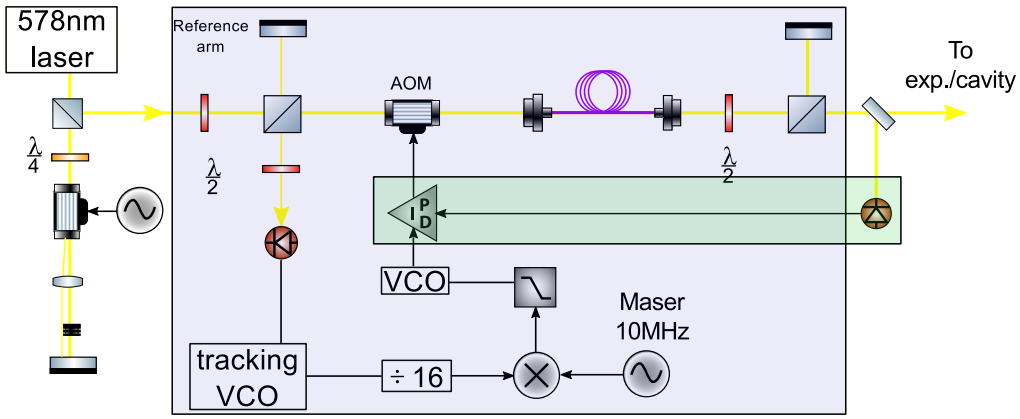

Figure 3.15: Layout of a single clock laser distribution line. The blue shaded area represents the phase noise compensation system. The green shaded region is the power stabilization system. The frequency control done on a double-pass AOM.

Fiber noise cancellation The clock laser is distributed to different parts of the experiment using polarization maintaining optical fibers. However, temperature and mechanical stress induce optical path variation thus introducing additional phase noise to the light they are carrying. To compensate for these effect, an active system of phase noise compensation is implemented on the lines distributing the light to the ultra stable cavity and to the experimental chamber as well. The optical layout is basically a Michelson interferometer (see fig. 3.15). This system exploits a back-reflected portion of the light that makes a round trip passing twice through the fiber thus carrying twice the phase noise compared to the portion that did not crossed the fiber (called reference arm). The idea is to assess the phase noise by measuring the frequency variation of a beatnote generated by the back-reflected light with the reference arm.

Firstly, part of the incoming light is sent to the reference arm. Then, before entering the fiber, the light is frequency shifted by an AOM at 80 MHz. The light is sent through a polarization maintaining optical fiber and a fraction of the output light is sent back. This light passes a second time through the AOM, is superimposed with the reference arm and then is directed on a fast photodiode

that detects the beatnote. A servo loop acting on the RF signals driving the AOM stabilizes the beatnote frequency to a reference $\omega_{\text{ref}} = 10\,\text{MHz}$ signal provided by hydrogen maser.

The electronic circuit which realizes the feedback loop is home-made board which takes the beatnote signal and compares it with the 10 MHz reference from the maser (see fig. 3.15). The AOM works at a frequency $\omega_{\text{AOM}} = 80\,\text{MHz}$ so the beatnote has a frequency of $\omega_b = 2(\omega_{\text{AOM}} + \phi(\omega))$ where $\phi(\omega)$ is the additional phase noise. The board requires a beatnote minimum input power of $-10\,\text{dBm}$ to work propery. The input signal is then electronically manipulated in order to be effectively compared to the reference signal. A tracking VCO circuit is locked to the beatnote input signal providing a clean signal at ω_b without additional noise sources than fibers. This signal is divided by 16 to have a carrier frequency at 10 MHz that can be compared to the reference using a frequency mixer. The mixer output gives $\omega_b - \omega_{\text{ref}}$ (higher frequency components are filtered by a low-pass filter) which is proportional to the fiber noise $\phi(\omega)$ and it is used as error signal by a PID controller to close the loop. A second VCO (ROS-100, Mini-Circuits) produces an oscillating RF ω_{VCO} tuned by a voltage correction signal V_{corr}, coming from the PID output, with a typical linear tuning of 2-3 MHz/V. The RF correction drives the same AOM which modulates the light before the fiber so an offset is introduced to have corrections around 80 MHz.

The system has been tested using an interferometric measurement and it exhibits an instability at the 10^{-18} level after 1000 s of measurements.

Power stabilization Stabilization of the optical power of the clock laser in the different arms is another important factor that needs to be addressed to improve clock performances (both stability and accuracy). In fact, clock laser intensity fluctuations induce a different interrogation pulse area, eventually giving rise to aberrations on the spectroscopic feature. In the case of the ultra-stable cavity, a power fluctuation in the circulating power affects the instability of the local oscillator. A power stabilization scheme (see fig. 3.15) is implemented on the laser beam that performs the atomic interrogation and on the cavity branch.

The light intensity is controlled by a dedicated AOM by changing the driving RF power thus varying the diffraction efficiency. The control is made by a custom made board that takes the signal from a photodiode, which measures the light intensity, compares it to a tunable reference point and produces an error signal with a PID circuit (offset lock). The PID signal then drives a voltage variable attenuator (ZX73-2500, MiniCircuits) which regulates the AOM RF amplitude. In the case of the spectroscopy light the set point can be controlled remotely using a BNC port.

The same scheme is applied also on the blue slower beam and the detection lines as well as on the lattice laser. In these part of the experimental apparatus the optical power plays a central role. The slower intensity regulates the number

of trapped atoms and thus the atomic density in the lattice sites while the probe beam determines the signal read by the PMT. The lattice light induces shift on the atomic transition that scales with the optical power (see sec. 6.2.2) and a controlled modulation of this parameter is convenient when interleaved measurements are performed.

Upgraded system

During the absolute measurement campaign against the caesium fountain ITCsF2, reported in chapter 5.4, the ultra-stable laser stability was limited by an excess of seismic noise on the stabilization cavity. After the campaign the ultra-stable cavity as well as the infra-red laser source and the non-linear crystal were upgraded.

Figure 3.16: Picture of the new cavity positioned on the active anti-vibration platform inside the anti acoustic chamber. It can be noticed the absence of the chamber legs and the wooden platform, positioned on the floor, on which the system is supported.

The cavity used in this system is the one previously implemented in the 556 nm laser stabilization. The measured finesse is 151 000(1000) and the assessed zero CTE temperature is about 21 °C. The implemented thermal actuators are two heaters placed outside the vacuum chamber while the temperature is monitored by two thermistors inside. As a consequence, given the zero CTE below room temperature, the operative temperature is 27.45 °C, higher than what is required. However, with thermal fluctuation measured inside vacuum of about ±400 µK, the

performance of the thermal stabilization system is sufficient to not limit the laser instability.

To address the sensitivity to vibrations that affected the previous system, we put the optical cavity on an active anti-vibration platform (Optosigma-OSDVIA-T45) which ensures 30 dB reduction of vibrations at 5 Hz. Moreover, we modified the acoustic chamber structure by removing the standing legs and positioning the chamber directly on the floor using a wooden basis, reducing additional vibration resonances induced by the higher and less stiff structure (see fig. 3.16).

The frequency lock circuit is a FALC module by Toptica with two locking loops, a fast one acting the diode laser current and a slow one which makes corrections on the laser piezo. The lock bandwidth is 300 kHz with still room for improvements.

Chapter 4

Multi-wavelength cavity

The necessity of frequency stabilized laser light has been explicated in previous chapter. In the case of atomic manipulation, such as laser cooling and trapping, the INRIM Yb optical lattice clock operated with many different systems depending on the specific laser requirements. In the previous chapter are illustrated these implementations like the lock on spectroscopic feature for the blue MOT beams, the use of the optical comb or the green MOT optical cavity. This solution allowed to operate the clock profitably and to obtain significative results as reported in the next chapter but, on the other hand, the multitude of different stabilization schemes brought a certain degree of complexity in the system.

We decided to upgrade the system by designing and implementing a single optical cavity which allows to frequency lock simultaneously several lasers at different wavelengths, in particular the MOT and the lattice lasers. It consists in a Fabry-Perot resonator with mirrors coated for 399 nm (Cooling and 1st stage MOT), 556 nm (2nd stage MOT) and 759 nm (lattice) light. The lasers are locked using the offset-sideband locking technique [66], that is a modified version of the common PDH method (illustrated in sec. 2.5.2), which ensures great flexibility for the experimental conditions. In this way the others frequency stabilization systems are replaced by a compact single device and a single locking technique, with the possibility to be easily moved in case of necessity.

This work on the multi-wavelength cavity was published in [79] and presented at EFTF-IFCS 2017 as well. The first part of the chapter illustrates the experimental apparatus then the cavity performances characterization are reported.

4.1 Experimental apparatus

4.1.1 The optical cavity

The multi-wavelength cavity used in the experiment is produced by Advanced Thin Films and consists in a 10 cm ($\Delta\nu_{\mathrm{FSR}} = 1.5$ GHz) horizontal resonator with

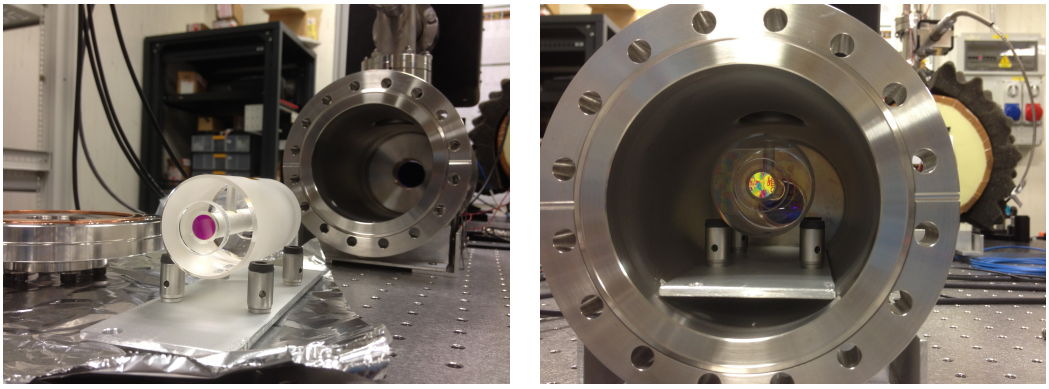

Figure 4.1: Multi-wavelength cavity with its holder during the instalment in the vacuum housing.

cylindrical ULE spacer and mirrors. The two mirrors are in a hemispherical configuration consisting in a flat and a curved mirrors with $-0.5\,\mathrm{m}$ radius of curvature and they both feature triple-v coating for 399 nm, 556 nm and 759 nm light. The manufacturer declared a finesse between 1000 and 3000 at 399 nm and 759 nm and higher than 15 000 at 556 nm evaluated on coating design. The coating characterization has been performed by the manufacturer on witness samples using a spectrophotometer, reported in figs. 4.2 and 4.3.

The cavity is placed inside a vacuum housing which is supplied with a 20 L ion pump that ensures a pressure of about 6×10^{-8} mbar. The temperature inside the vacuum is read by a thermistor and is actively stabilized by a heater from the outer side of the housing using the active disturbance rejection method [80]. The housing is thermally isolated with foam and aluminium foil while inside the vacuum we put ten layers of crumpled Mylar foils.

Figure 4.4 shows the temperature of the vacuum chamber, the thermal fluctuations are about $\pm 10\,\mathrm{m°C}$ depending on the air conditioning activity of the laboratory. The cavity holder consists in an aluminium plate with four 10 mmx25 mm Thorlabs posts screwed to it. Viton pads, glued at the top of the posts, support the resonator (see fig. 4.1). Figure 4.1 shows the cavity when it was installed in the vacuum housing.

4.1.2 The optical table

A drawing of the overall system is given in fig. 4.5. The cavity is mounted on a dedicated 60 cmx90 cmx1 cm aluminium optical breadboard together with the mode matching telescopes, three photodiodes ($\mathrm{PD_{PDH}}$) and the fiber output couplers. The bench can be moved ensuring transportability. Each laser beam passes

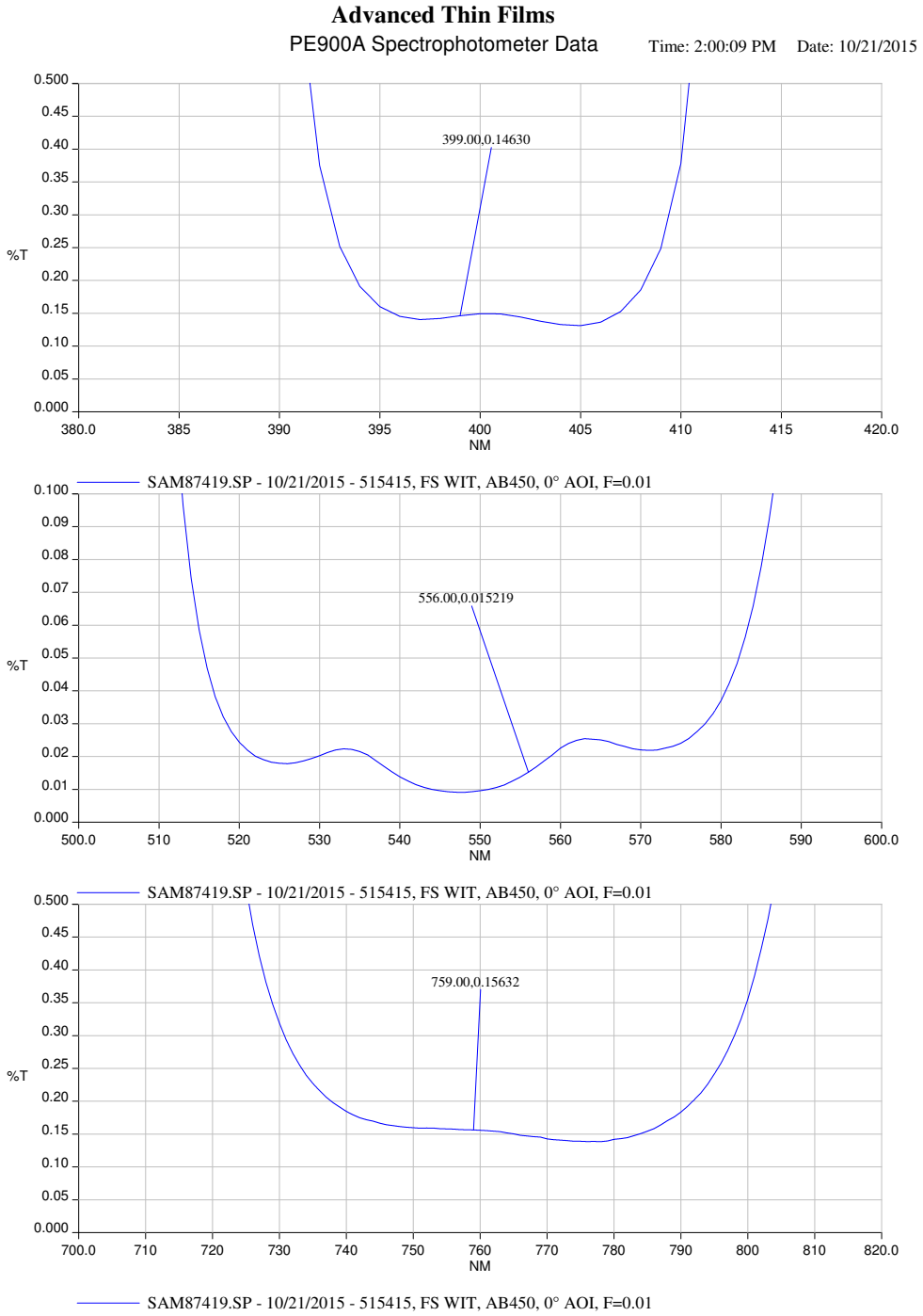

Figure 4.2: High reflective coating data. From Advanced Thin Films.

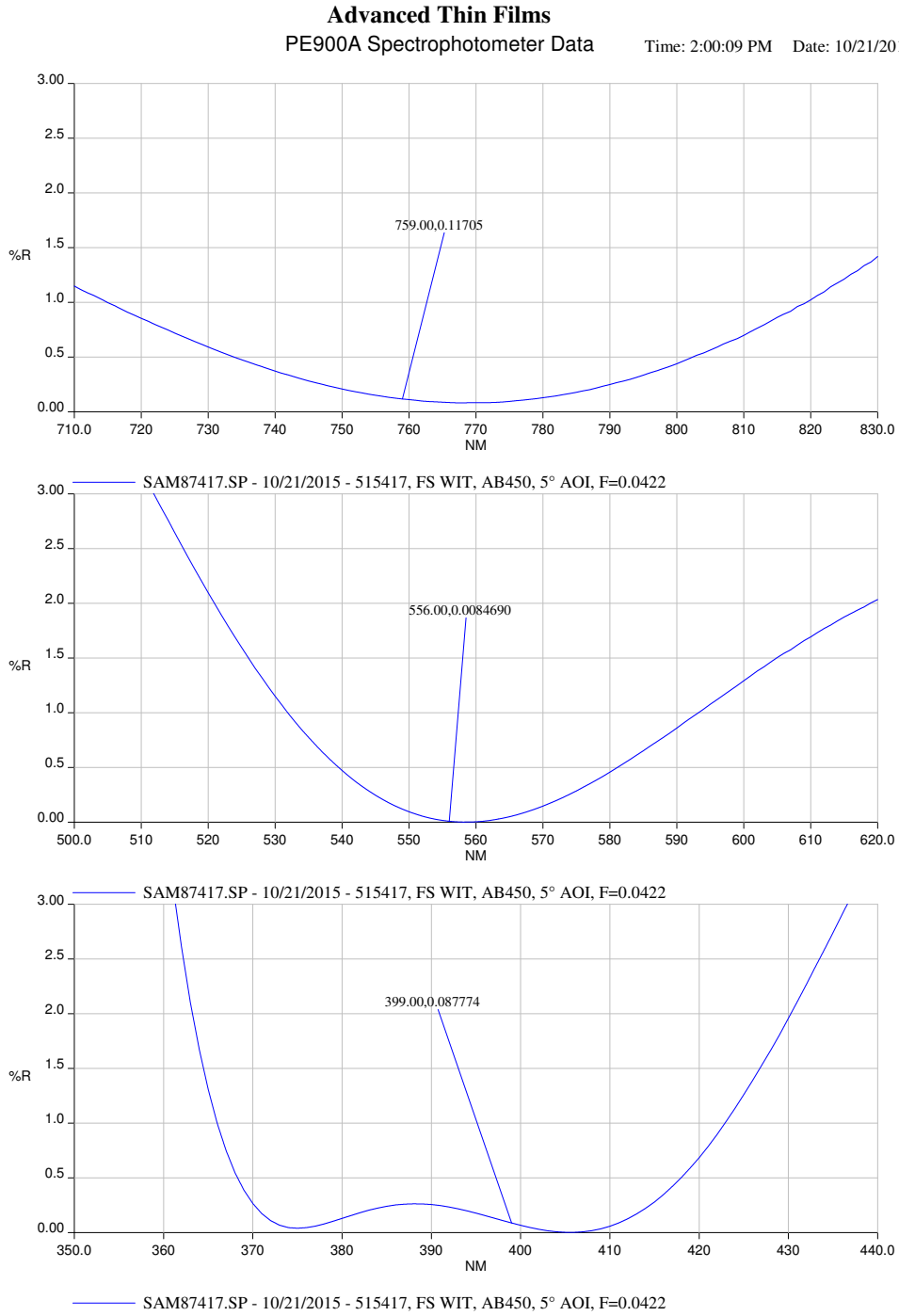

Figure 4.3: Anti reflective coating data. From Advanced Thin Films.

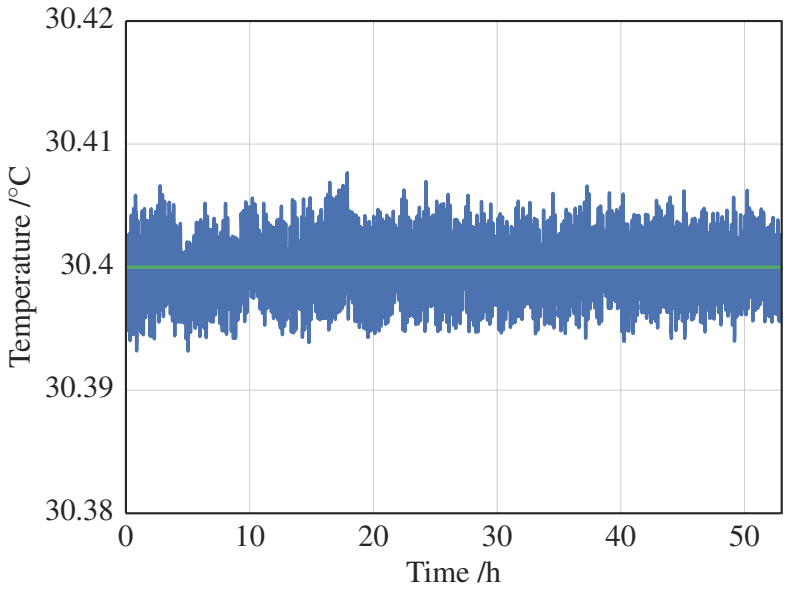

Figure 4.4: Temperature measured inside the vacuum chamber.

through its respective EOM, then it is sent to the cavity table through a polarization maintaining optical fiber. There the beams are superimposed using two dichroic mirrors and enter the cavity from the flat mirror side. At the opposite side a photodiode and a video camera monitor the transmitted light. For the 556 nm, 759 nm and 798 nm we used Jenoptik fiber based broadband EOMs (up to ∼1 GHz) driven by commercial synthesisers featuring phase modulation and with a RF power up to 50 mW. For the 399 nm radiation we used a QBIG EOM, coupled in air, with two resonance frequencies tunable in the ranges 0.6-1 GHz and 1-1.6 GHz. The resonances bandwidth is about 11 MHz, which is enough for Ω_{PDH}. Ω_{gap} is adjusted by tuning the resonance frequency. This EOM is powered by a custom made QBIG synthesiser which can provide the required 4 W RF power.

Three photodiodes ($\mathrm{PD}_{\mathrm{PDH}}$) collect the reflected light coming from the cavity. The lasers are independently modulated at different Ω_{PDH} and the $\mathrm{PD}_{\mathrm{PDH}}$ signals are filtered by narrow band-pass filters to suppress any possible crosstalks between the wavelengths. After amplification, the signals are sent to mixers and demodulated at the respective Ω_{PDH} to produce independent error signals which are then fed to the feedback electronics.

Moreover, the 399 nm laser can be frequency locked in two ways: by directly sending the 399 nm radiation to the cavity or by using the 798 nm light instead. In the latter case the beam is extracted before the duplication cavity, it is fiber coupled and then sent to the cavity in place of 399 nm light. The 798 nm beam is superimposed with the 759 nm on a 50/50 beamsplitter and the reflected light from the cavity is detected by the same photodiode ($\mathrm{PD1}_{\mathrm{PDH}}$). The signal is then

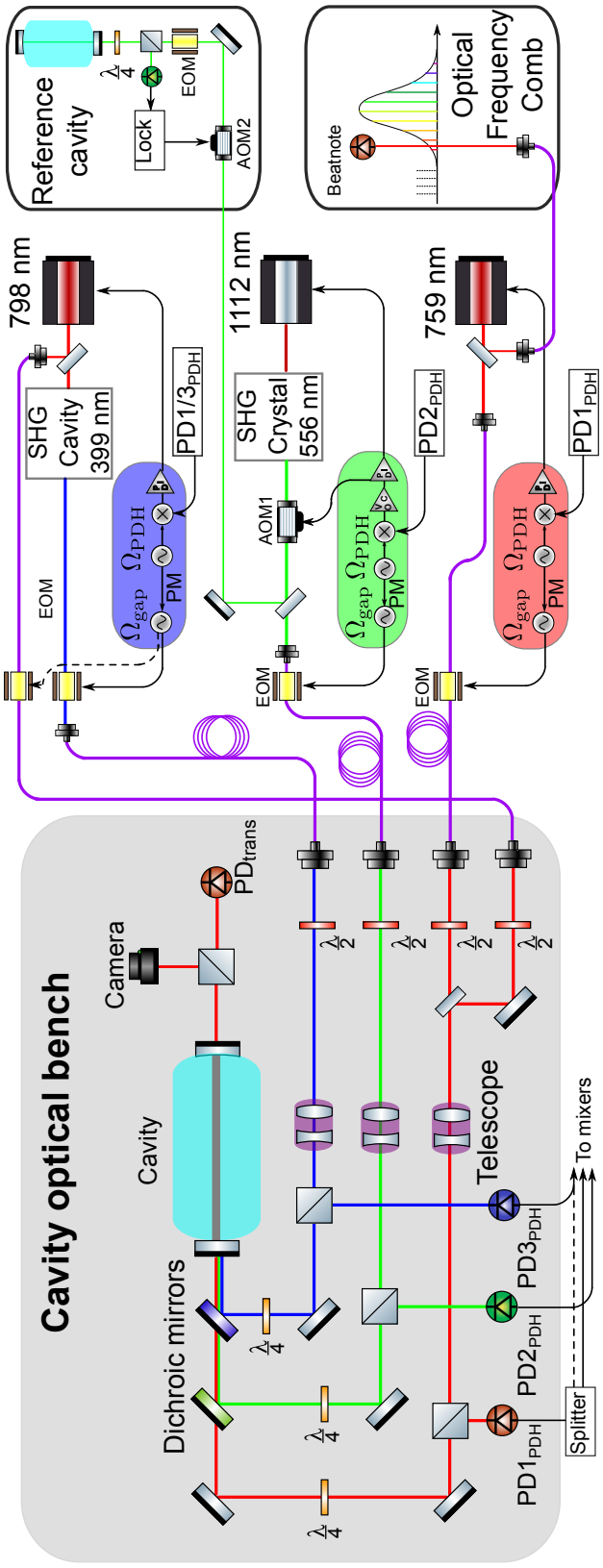

Figure 4.5: Setup of the multi-wavelength cavity: black arrowed lines are electrical signal paths, dashed lines represent the electrical signal path for the 798 nm laser stabilization. Coloured paths signify free-space laser light and polarizing maintaining fibers are in purple. In the right hand side of the picture the set up involving the reference cavity and the optical frequency comb are shown. From [79].

splitted using a RF splitter (MiniCircuits LRPS-2-1), independently filtered and goes to two different PID controls.

4.1.3 Locking to the cavity

The 556 nm laser is referred to the cavity with two locks: a fast one acting on an AOM with a bandwidth of 90 kHz and a slow one acting on the laser's piezo with 3 kHz bandwidth. The electronic feedback loop comprise a PID control and a voltage-control oscillator (VCO) to drive the AOM. The stabilization of the 399 nm (798 nm) and 759 nm uses the respective laser piezo to control the frequency by means of a PID circuit with 3 kHz bandwidth. In table 4.1 are summarized the parameters used to lock the different lasers to the cavity.

Table 4.1: Parameters used for locking the lasers. The bridge frequency for the 759 nm laser can be tuned to the preferred value according to the experimental conditions. From [79].

$\boldsymbol{\lambda}$/nm	$\boldsymbol{P}_{\text{in}}$/µW	$\boldsymbol{\Omega}_{\text{gap}}$/MHz	$\boldsymbol{\Omega}_{\text{PDH}}$/MHz
399	60.5	850.4	8.1
556	6.3	327.0	10.7
759	13.0	/	11.5
798	6.5	174.1	5.9

Following the offset-sideband locking technique we phase modulate the RF signal piloting EOM generating two set of sidebands. The EOM gives rise to the first order sidebands spaced by Ω_{gap} while the phase modulation generates further sidebands around the first order ones, separated by the phase modulation frequency (Ω_{PDH}). By increasing the RF power the carrier amplitude is reduced in favour of the sidebands, this is regulated to maximise the first order sidebands. The phase modulation depth is optimized by maximizing the PDH error signal. This behaviour of the phase modulated light can be seen in fig. 4.6 which shows the transmitted light and PDH error signals for the 556 nm laser. By tuning Ω_{gap} the first order sideband can be kept in resonance with the cavity and locked to it while the laser carrier frequency can be moved to the desired value without the use of additional modulators. This have been tested modulating the RF as fast as 1 MHz/s up to 500 MHz span. The span is limited by the synthesiser capability.

4.2 Characterization

The multi-wavelength cavity is meant to serve the Yb optical lattice clock to frequency stabilize the MOT and the lattice lasers. The optical lattice operates at

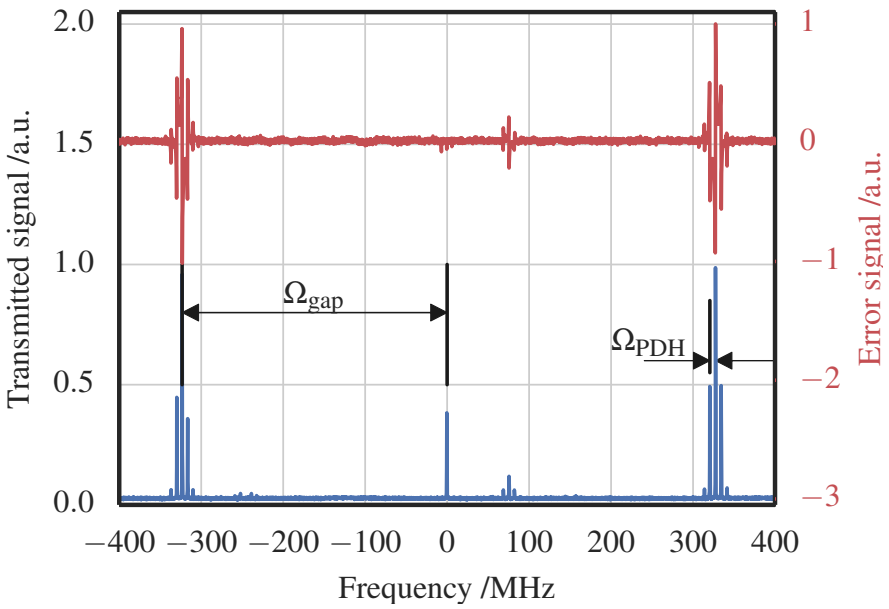

Figure 4.6: Blue: Typical spectrum of the transmitted 559 nm light through the cavity. It shows the depleted carrier, the first order sidebands spaced by Ω_{gap} and the second order sidebands, generated by the PM signal, spaced by Ω_{PDH}. It can be noticed that the carrier does not produce any error signal. Smaller peaks are higher order cavity modes. Red: PDH error signal. From [79].

the magic frequency (see chapter 2) and the clock demands a relative uncertainty introduced by the lattice laser light less than 1×10^{-18}. Taking into account a first-order clock-transition sensitivity of 21.6 mHz/GHz E_r [25] and 200 recoil energy (E_r) lattice trap depth, the required lattice frequency drift accumulated in a typical day of operation ($\simeq$ 10 h) is less than 120 kHz. Regarding the MOT lasers the requirements are evaluated by considering the magneto-optical trapping performance as well as detection, lattice loading efficiency, achievable atomic temperature and atomic state manipulation. This lead to a laser linewidth a daily drift of lass than 1 MHz for the first stage MOT (at 399 nm) and 100 kHz for the second stage (at 556 nm).

4.2.1 Finesse measurement

From (2.33) the Finesse of an optical resonator is defined as the ratio of the mode frequency spacing, or free spectral range ($\Delta\nu_{FSR}$), and the linewidth of the cavity mode ($\delta\nu$). The latter can be expressed as:

$$\delta\nu = \frac{1}{2\pi\tau}$$

giving:

$$\mathcal{F} = \frac{\Delta\nu_{\mathrm{FSR}}}{\delta\nu} = \frac{\pi c\tau}{L}$$

with L the cavity length and τ the decay lifetime of the light resonant with the cavity.

To assess the finesse of the cavity for the various wavelength we used the cavity ring down technique. This method is based on a time measure of the exponential extinction rate of the transmitted light through the optical cavity. To do that the laser frequency is put in resonance with the cavity and then the light is quickly turned off while a fast photodiode (Menlo FPD510-FV - raise time 2 ns) measures the transmitted light. The light is turned off using an electronic switch (response time ∼20 ns) that interrupts the RF frequency driving the EOM (response time ∼15 ns) and thus extinguishing the sideband which was resonant with the cavity. The optical intensity accumulated in the resonator starts to decrease as $I \sim e^{-t/\tau}$, where τ is the ring down time of the cavity. The switch is piloted with a TTL signal generated by a computer which also triggers an oscilloscope that takes the photodiode signal and records the exponential decay. The experimental layout is reported in fig. 4.7 while fig. 4.8a shows a typical ring down signal.

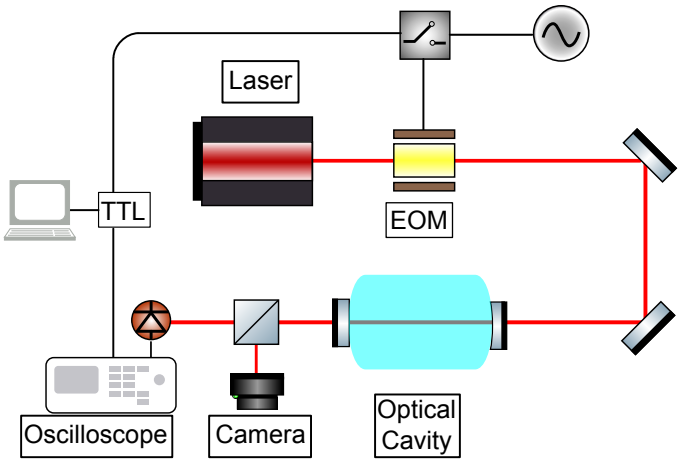

Figure 4.7: Experimental layout for the ring-down measure.

For the 399 nm light the finesse was evaluated by measuring the linewidth of the transmitted mode through the cavity since the decay time was too fast to be measured properly. The frequency was scanned slowly, compared to the cavity response at this wavelength (20 MHz scan in 125 ms compared to ∼60 ns decay time), by using an AOM. The transmitted light is collected on the same photodiode used for the ring down measure and the signal is always recorded with an oscilloscope (see. Fig. 4.8b). We repeated the measure 10 times per each wavelength, the results are summarized in Tab. 4.2 along with the measured optical transmission (throughput) of the TEM_{00} mode. The throughput measure was taken by measuring the ratio

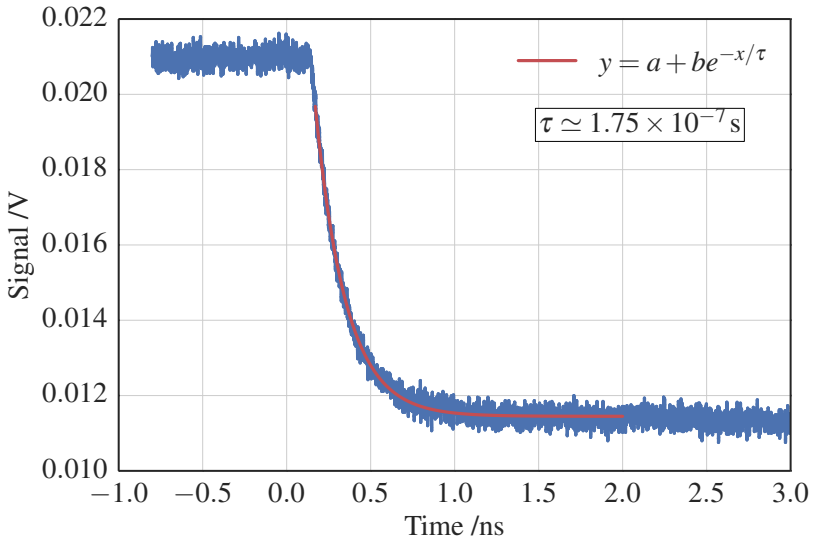

(a) Typical transmitted light signal at 759 nm used to extract the extinction time. Exponential fit present as well.

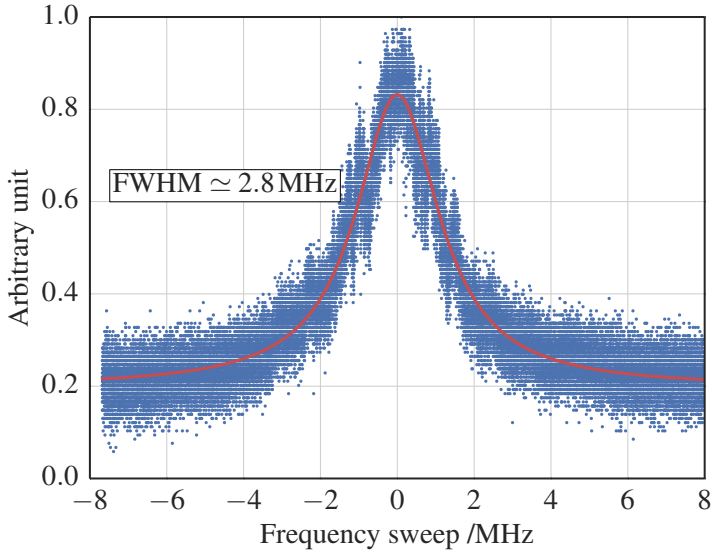

(b) Transmitted cavity mode at 339 nm with lorentzian fit.

Figure 4.8: Signals used to evaluate the finesse.

between the input and the transmitted optical power of the TEM_{00} mode. The video camera was used to assure the correct transmitted mode.

Table 4.2: Measured cavity properties. From [79].

λ/nm	**Finesse**		**Throughput**/%
	declared	**measured**	
399	1000-3000	550 ± 60	3
556	15 000	13900 ± 600	20
759	1000-3000	1660 ± 150	65
798	/	1200 ± 150	69

4.2.2 556 nm characterization

Excluding the clock laser, which is independently stabilized on a separate ultra-stable cavity (see sections 2.5 and 3.3.5), the most demanding frequency stabilization in our system is the 556 nm laser. To characterize the laser linewidth, frequency stability and the cavity's point of vanishing expansion (zero CTE) dedicated measures was performed using an additional ultra-stable cavity as reference. The performance of the reference cavity was reported in [59]. The cavity was also used to frequency stabilize the 556 nm laser before the multi-wavelength one was adopted.

Some 556 nm light (few tens of µW) is extracted after being pre-stabilized on the multi-wavelength cavity. This auxiliary beam is then locked to the reference cavity using an additional AOM (AOM1 in fig. 4.5) together with a PID control with a total bandwith of 100 kHz. In this way the RF signal which drives AOM1 represents the frequency difference between the two cavities whereas the linewidth of that signal represents the laser linewidth. The noise of the error signal of the two laser-branches is uncorrelated within the bandwidth of the two controls (100 kHz).

Zero CTE temperature

To evaluate the temperature where the thermal expansion coefficient vanishes (zero CTE) we measured the frequency difference between the reference and the multi-wavelength cavities while changing the temperature of the latter. This was done by changing the temperature set point of the control driving the heater outside the housing. The result is reported in fig. 4.9a together with a parabolic fit which gives a zero CTE temperature of 30.4 ± 0.3 °C. The data were taken during about one week and the reference cavity drift during this time is negligible.

Linewidth and frequency stability

The frequency difference signal between the two cavities is sent to a spectrum analyser to record the laser linewidth. By incrementally increasing the resolution

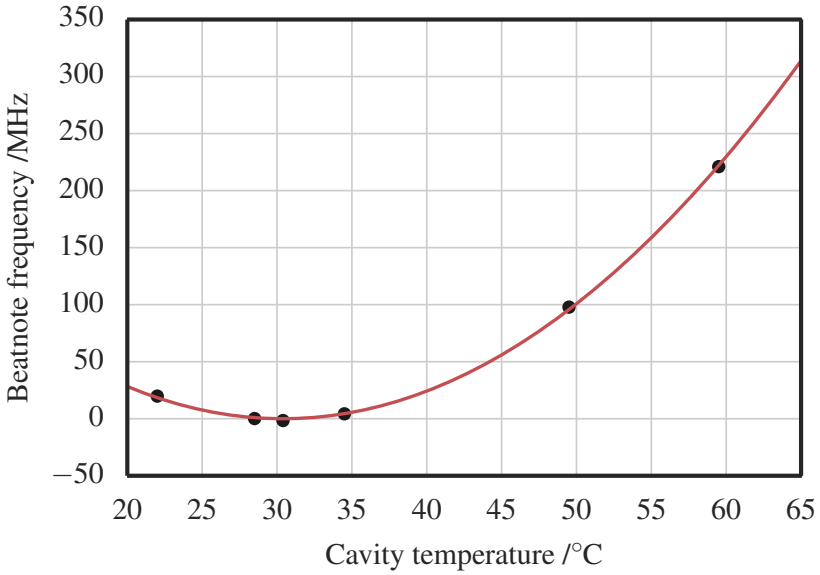

(a) Measurement of the zero CTE point.

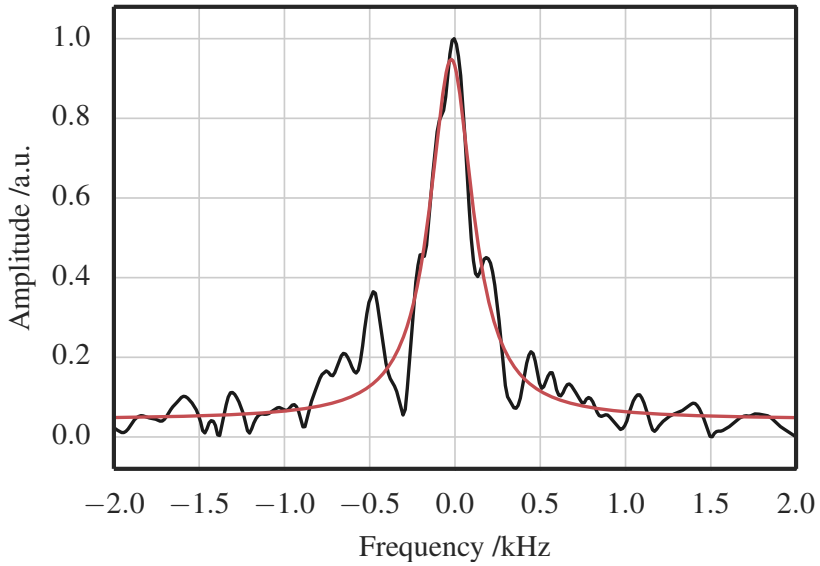

(b) Frequency spectrum of the 556 nm laser locked to the multi-wavelength cavity recorded by a spectrum analyser with 80 ms sweeping time and 100 Hz resolution.

Figure 4.9: Frequency-comparison of the multi-wavelength cavity against the reference one at at 556 nm. From [79].

of the instrument a reduction of the signal can bee seen. We set it to 80 ms of sweep time and 100 Hz resolution giving an upper limit linewidth of 300 Hz (see Fig. 4.9b). The frequency noise of the difference signal was measured using a phasemeter, the

result is shown in figure 4.10. We assessed a white noise floor of $5\,\mathrm{Hz}/\sqrt{\mathrm{Hz}}$ and a flicker contribution of $15\,\mathrm{Hz}/\sqrt{\mathrm{f}}$ (f being the Fourier frequency). Typical acoustic noise is present between 10 Hz and 130 Hz.

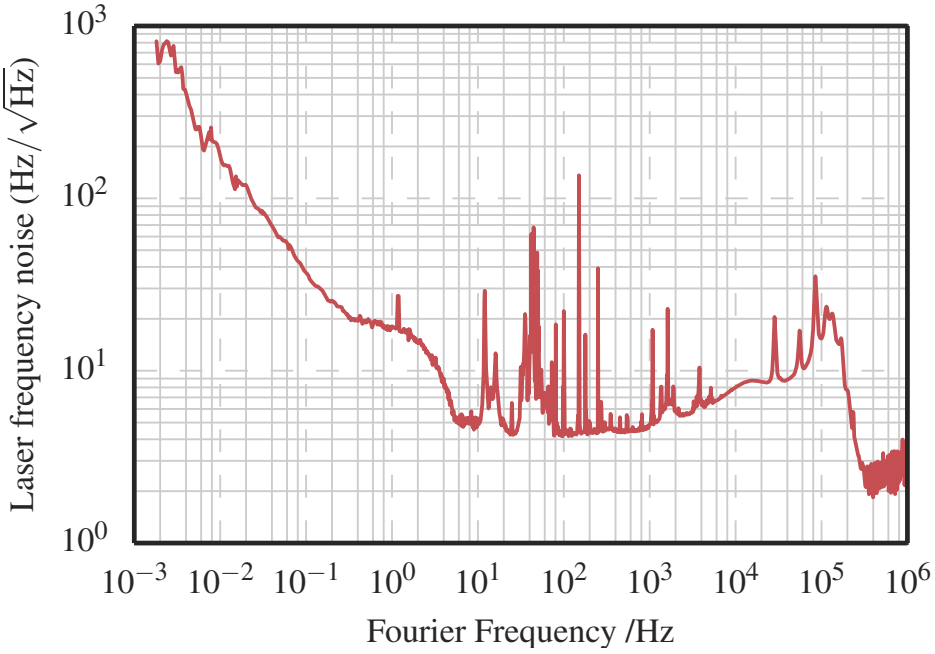

Figure 4.10: Frequency noise spectrum of the 556 nm laser locked to the cavity. From [79].

To corroborate the linewidth measure we calculated the linewidth from the frequency noise spectrum exploiting the β-line technique [81]. The separation line $S_{\delta\nu}(f) = 8\log(2)f/\pi^2$ gives a frequency cut of $f_c = 65\,\mathrm{Hz}$. According to this calculation, for Fourier frequencies $f < f_c$ the noise contributes mainly to the lineshape and thus to the linewidth while for $f > f_c$ it affects mainly the wings. The full width half maximum (FWHM) of the laser frequency is given by:

$$\mathrm{FWHM} = (8\log(2)A)^{1/2} \tag{4.1}$$

with

$$A = \int_{0.001}^{f_c} S_{\delta\nu}(f)df. \tag{4.2}$$

The numerical integration of the laser frequency noise spectrum yields a linewidth of about 245 Hz, which is quite consistent to the experimental observation. Simplifying the noise spectrum with only the flicker and white noise components leads to an analytical integration:

$$A = \int_{0.001\,\mathrm{Hz}}^{5\,\mathrm{Hz}} \frac{225\,\mathrm{Hz}^2}{f}df + \int_{5\,\mathrm{Hz}}^{65\,\mathrm{Hz}} 25\,\mathrm{Hz}^2/\mathrm{Hz}\;df$$

which results in a FWHM = 145 Hz.

From the phasemeter data the Allan-deviation is also obtained and is reported in figure 4.11. From this data the fractional frequency stability at 1 s is 3×10^{-14},

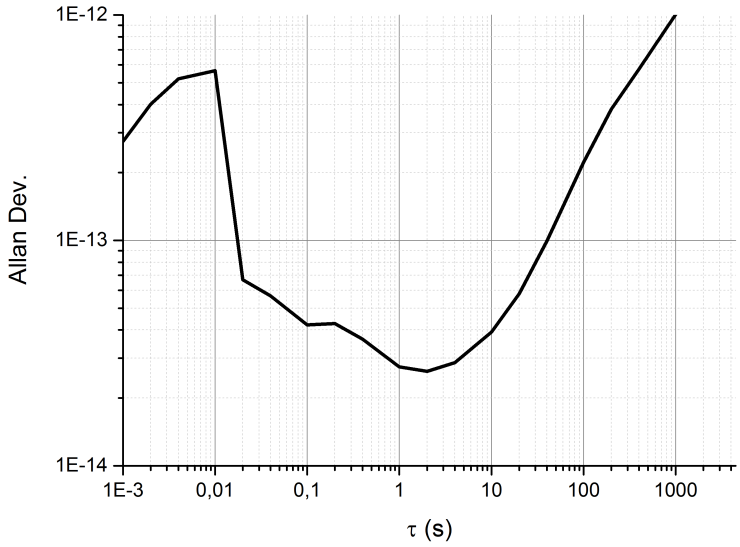

Figure 4.11: Frequency stability of the 556 nm laser locked to the multi-wavelength cavity and compared to the reference cavity.

and is attributed to the multi-wavelength cavity only.

4.2.3 Drift measurement

The cavity frequency drift is measured by using a fiber-based optical frequency comb referenced to a hydrogen maser. The 759 nm laser, frequency locked to the multi-wavelength cavity, is sent through a polarization maintaining optical fiber to the comb table where it is beaten with a comb tooth on a fast photodiode. The beatnote signal is then filtered, amplified and counted by a frequency counter. To bring the beatnote frequency to the counter operating range (1-60 MHz) signal is shifted using a mixer and an additional synthesiser (see 4.12).

To observe effects caused by the presence of several laser beams inside the cavity the drift measure was taken while the lasers are sequentially locked to the cavity. The result is reported in Fig. 4.13. The red trace shows the drift of the 759 nm laser when the 798 nm and 556 nm radiations are locked at the same time. The drift is less than 2 kHz/h with no significant interactions with the other lasers. However, when the 399 nm light is sent to the cavity instead of the 798 nm (fig 4.13, blue trace), we observed and abrupt shift of about 50 kHz in 4 minutes followed by a constant

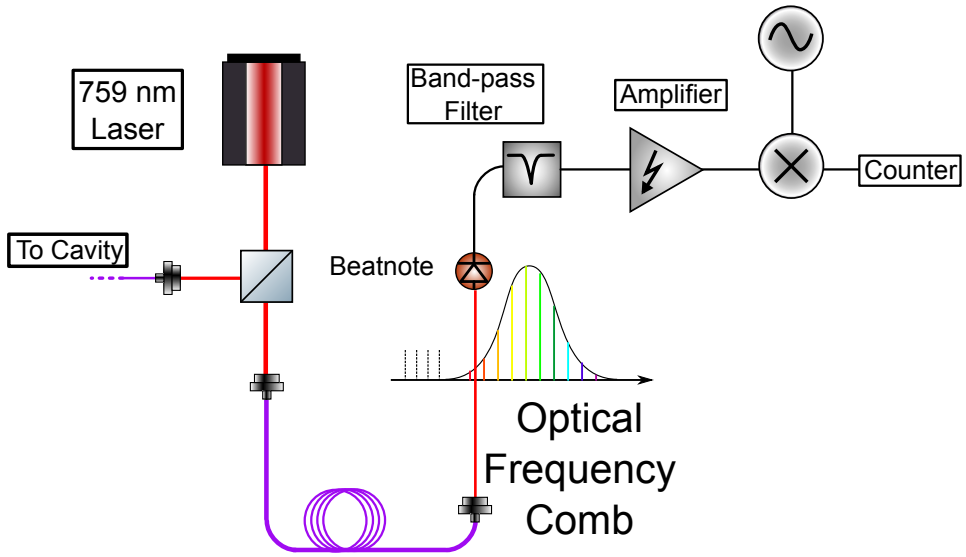

Figure 4.12: Detail of the experimental layout for the drift measure with the optical frequency comb. In purple are the optical fibers.

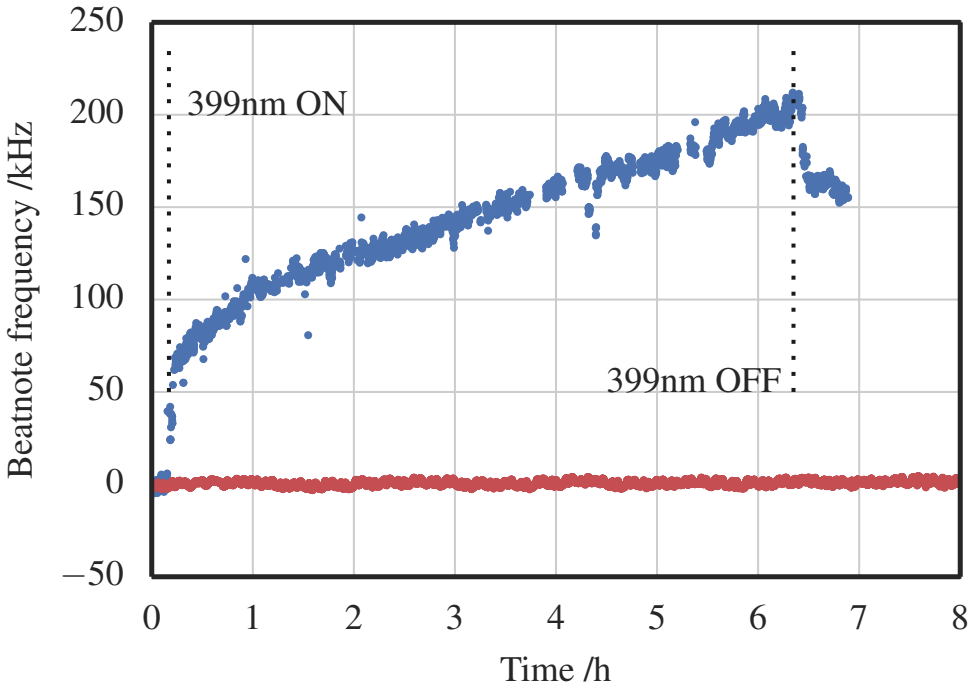

Figure 4.13: Beatnote frequency of the 759 nm laser with the frequency comb referenced to an H-maser. Red: 798 nm 759 nm 556 nm lasers simultaneously locked to the cavity. Blue: 759 nm, 556 nm and 399 nm sequentially locked. Gaps in the data are cycle leaps of the counter. From [79].

22 kHz/h drift. This tenfold increment comes from the high optical absorption of the mirrors coating at 399 nm giving rise to thermal effects. This is also testified by the low finesse and throughput at this wavelength. Moreover, the timescale of the shift (∼200 s) also suggests the mirror deformation takes place on the coating level rather than at the cavity assembly (temperature stabilized on the long therm ∼10 h). The 399 nm radiation can be troublesome and we have already experienced the lower performance of the optics toward the ultra violet region.

Since the finesse is fully determined by the mirrors' cavity losses we can estimate them using the result obtained in Tab. 4.2. For low losses the finesse can be expressed as:

$$\mathcal{F} = \frac{\pi}{2\arcsin\left(\frac{1-\sqrt{\rho}}{2\sqrt[4]{\rho}}\right)} \approx \frac{2\pi}{1-\rho}$$

where ρ is the circulating power after one round-trip, thus $1-\rho$ gives the loss. For a finesse of 550 the round-trip loss is about 1.1 %.

Considering the possible damage on the cavity optics in the long term using the 399 nm light as well as the overall performance we decided to stabilize the 399 nm laser by sending the 798 nm laser to the cavity.

Chapter 5

INRIM Yb clock characterization and absolute measurement

In this chapter the absolute frequency measurement of the unperturbed clock transition ($^1S_0 - ^3P_0$) of ^{171}Yb using the cryogenic caesium fountain ITCsF2 [13] as primary frequency standard is reported. The result of this measurement was already published in [25]. From a metrological standpoint, absolute frequency measurements are fundamental steps as they address the reproducibility of a physical quantity taken as reference, such as an atomic transition, and make possible a comparison between realizations of laboratories around the world. This kind of measurements are even more important in the case of optical lattice clocks. Indeed, we will see that they outperform the current primary Cs frequency standard in terms of both fractional uncertainty and stability, falling in the unconventional, but not completely new, situation where the system under test performs better than the standard. It is mandatory, also, to demonstrate the effectively performances of the different frequency standards in view of a possible redefinition of SI second in terms of an optical transition.

The chapter is organized as follows, firstly the clock operation is reported along with the experimental details of the atomic manipulations and spectroscopy. After that, the systematic shift evaluation is given with the complete uncertainty budget and, lastly, the description of the absolute measurement campaign is illustrated.

5.1 Clock operation

The overall experimental layout is reported in fig. 5.1. Several optics, mounted on two breadboard placed around the experimental chamber, allows the different laser beams to reach the atomic sample making possible the atomic manipulation and interrogation.

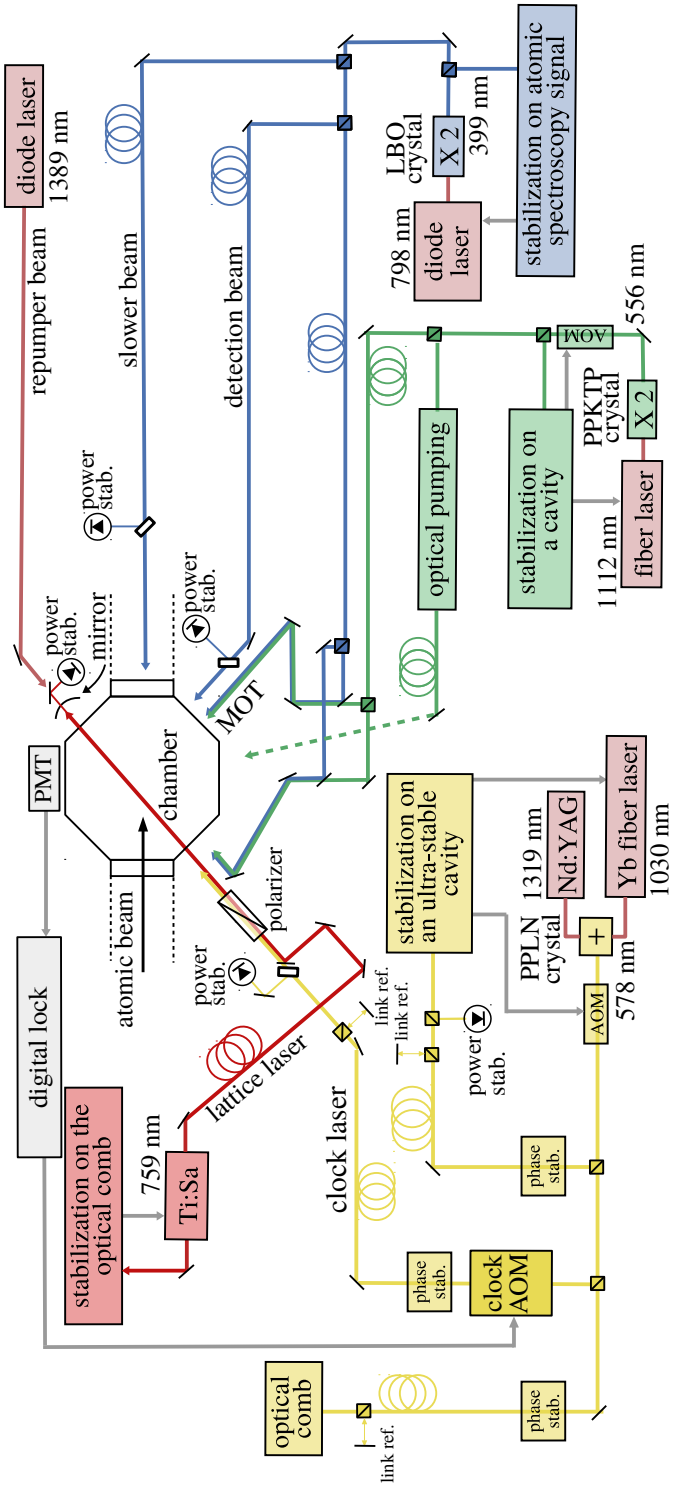

Figure 5.1: Experimental layout of the clock showing the lasers generation and the delivery to the experimental chamber. From [25].

5.1.1 Laser cooling and magneto optical trap

The hot atomic beam is generated by the atomic oven heated up to 400 °C. It is slowed exploiting the strong $^1S_0 - {}^1P_1$ by a counter-propagating beam at 399 nm red detuned from the transition by −350 MHz. The typical optical power delivered on the atoms is about 35 mW and it can be stabilized and modulated by a dedicated power stabilization circuit described in section 3.3.5. The beam $1/e^2$ radius is about 1 cm and the polarization is controlled by a $\lambda/4$ waveplate before getting into the vacuum chamber. It was already mentioned that the system is designed to operate without a Zeeman slower. To compensate for that, the oven is kept close to the trapping region so to have a strong collimated atomic beam and, at the same time, the MOT coils magnetic fringe field helps the slowing efficiency.

The slowing is an ancillary process used to the trap the atoms inside the MOT. The first stage of such a trap is realized using the same blue transition of the slowing process. The MOT blue laser is divided in three branches (one per each axis), sent through the experimental chamber in an orthogonal fashion and then retro-reflected. The light is red-detuned by −20 MHz using the AOM present on the distribution bench. Each line has a power of 10 mW (∼ 30 mW total) and a beam diameter of 1 cm, measured close to the vacuum chamber. The polarization is controlled by a pair of $\lambda/4$ waveplates placed at the entrance and the exit of the chamber to separately tune the the input and back-reflected light respectively. The slower and MOT beams are kept on for the entire duration of the first stage MOT, typically 150 ms, with a magnetic field set at 0.35 T/m along the vertical axis (z). In this way up to 4×10^7 atoms are collected after this process at a temperature of about 1 mK.

The second stage MOT is based on the narrower $^1S_0 - {}^3P_1$ transition at 556 nm, in the green region of the spectrum, to further reduce the temperature of the atomic cloud before being transferred in the optical lattice. To do that, the green MOT beam is also divided in three lines and overlapped onto the blue beams on dichroic mirrors. In this way the green trap region is exactly overlapped on the blue one. The power delivered per each line is about 0.67 mW (∼ 2 mW in total) while the beam $1/e^2$ radius is approximately 0.5 cm. These laser beams cross the same waveplates and are retro reflected by the same mirrors used for the first stage MOT. The green light is maintained on also during the loading of the blue MOT. To switch from the first to the second MOT stage the blue light is simply turned off using the AOMs together with mechanical shutters.

To further optimize the cooling process as well as maximize the loading efficiency of the optical lattice the second stage MOT presents three distinct phases with different frequency, intensity and magnetic field as well. The first one collects the maximum number of atoms from the blue MOT. It lasts 30 ms during which the laser beams are kept full power with a magnetic field gradient of 0.13 T/m. The second substage provides the conditions to cool the atomic cloud down to about

10 µK. During 20 ms the magnetic field is ramped up to 0.2 T/m while the light intensity is reduced by 10 times and the frequency is tuned closer to the atomic resonance. The last phase is meant to maximize the loading efficiency of the optical lattice. It lasts 10 ms with a magnetic field gradient of 0.23 T/m. The control of the laser frequency and intensity is done by means of an AOM (AOM2 in fig. 3.8) which is driven by three separate synthesisers selected by an electronic switch.

The typical fraction of atoms transferred from the blue to the green MOT is 70 % while between 6-10 % can be effectively loaded in the lattice. This results in an atomic population trapped in the lattice of about 7000-15 000 depending on the experimental requirements.

Frequency fine tuning

To fine tune the temperature of the green MOT we use the so called time-of-flight (TOF) signal of the free falling atoms [82]. The atoms are cooled and trapped in the green MOT using the typical sequence, after 60 ms the green light is turned off and the atoms are let fall under gravity potential. The detection beam is displaced few mm below the trapping region, detecting the falling cold atomic cloud which is also thermally expanding. The typical fluorescence signal collected by the PMT is Gaussian shaped (see fig. 5.2), where the width is related to the atomic temperature by the equation:

$$T = \frac{m_{\mathrm{Yb}}}{k_B}\sigma_v^2 \tag{5.1}$$

where m_{Yb} is the Yb mass, k_B is the Boltzmann contestant and σ_v^2 is the Gaussian thermal expansion variance which is be obtained, knowing the vertical beam displacement, from the PMT time signal. The global frequency of the green laser is fine tuned by changing the RF frequency of AOM (see fig. 5.1) and optimizing the TOF signal.

For the last green MOT sub-stage, the light frequency and intensity are fine tuned during the operation of the clock in order to maximize the number of atoms trapped in the lattice acting on AOM2 (see fig. 3.8).

5.1.2 Optical lattice

The optical lattice laser at 759 nm is brought to the experimental table with a core less end cap PM fiber which prevents the fiber to be damaged by the high optical intensity of the laser. To form the one dimensional trapping potential the beam is focused down to a waist of 45 µm the using a 200 mm lens and retro-reflected by a curved mirror. The lattice beam is aligned to overlap the trapping region with the green MOT and forms a 60 mrad angle with the horizontal plane. Typically about 1 W of 759 nm laser gets on the atoms, resulting in a trap depth

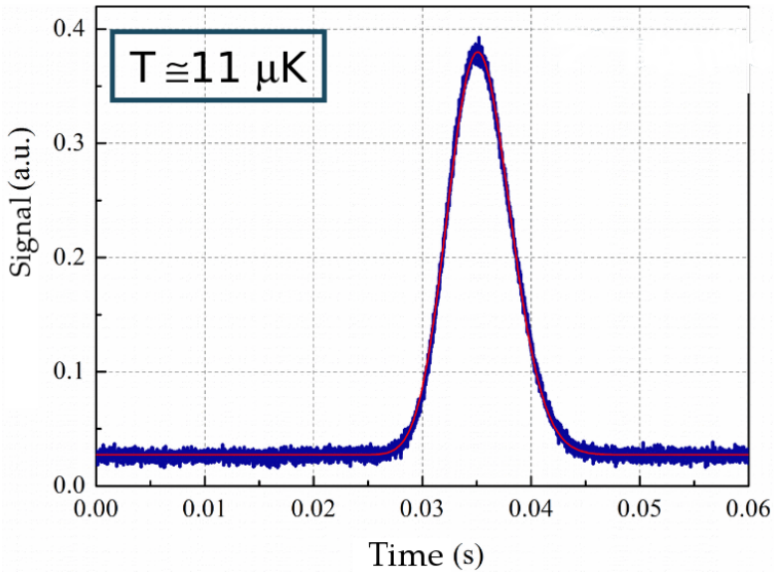

Figure 5.2: Typical time-of-flight signal as collected by the PMT and recorded by an oscilloscope. A Gaussian fit is superimposed on the trace showing an estimated temperature of the green MOT atoms of about 11 µK. From [76].

that can reach about 400 E_r. The operational trap depth is set at 200 E_r while the laser power is stabilized using a photodiode, which collects the beam leaking out the back-reflector, and the AOM in the distribution table (see fig. 3.9). During the operation of the clock the typical vacuum pressure is about 6×10^{-10} mbar, the resulting lifetime in the lattice is 2.7(1) s. The lattice beam is vertically polarized before entering the vacuum chamber with a Glann-Thompson polarizer (see fig. 5.1).

5.1.3 Spin polarization

The spin polarization process is done using the $^1S_0 - {}^3P_1$ at 556 nm. The laser beam double-passes through an AOM driven with a variable frequency RF (see fig. 3.8). The -1 order is sent on the main table with a PM optical fibre, here the polarization is cleaned with a half-waveplate and a polarizing beamsplitter cube. The beam is sent in the experimental chamber from the bottom using a 45° mirror and it is backreflected, in order to be aligned with the z (vertical) component of the magnetic field. The bias vertical magnetic field is generated using the z-axis compensation coils driven by a custom made power supply controlled by the PC.

The spin polarization phase takes place after the atoms are loaded in the optical lattice, the bias magnetic field is set at 0.4 mT while the light intensity is about 5 µW and illuminates the atoms for 1 ms. By optimizing the 556 nm pulse frequency 98 % pumping efficiency is achieved.

5.1.4 Spectroscopy

Once the atoms are trapped in the optical lattice they are ready to be interrogated by the clock laser light using the Rabi spectroscopy scheme (see sec. 2.4). The probe beam consist in a 578 nm laser beam with a $1/e^2$ waist radius of 200 µm and 70 nW of optical power. It is sent collinear with the lattice laser and the linear polarization is assured by the same Glan-Thompson polarizer used for the lattice, tuned to be aligned with the vertical bias magnetic field. The lattice retro-reflector has an anti-reflective coating at 578 nm with less then 1 % reflectivity at this wavelength. The power is actively stabilized and frequency tuned using a double pass AOM (clock AOM in fig. 5.1) positioned on the laser distribution bench before the fiber and piloted by a PC controlled synthesiser.

5.1.5 Detection

The detection of the excited fraction of atoms follows the normalized electron shelving technique[83, 84]. It is a destructive process that exploits the strong $^1S_0$ – $^1P_1$ transition at 399 nm. The transition is saturated by resonant blue pulses while the atomic fluorescence is collected by a photomultipiler tube (PMT) positioned on one side of the experimental chamber. The detection has a waist radius of 0.5 mm and it is directed orthogonally to the clock laser on the horizontal plane illuminating the atoms with 2.5 mW. The power is actively stabilized with the same method presented in section 3.3.5. The interaction with the detection light heats the atoms thus releasing them from the lattice trap, destroying the sample.

Considering the fact that the detection operates on the $^1S_0$ – $^1P_1$, the beam interacts only with atoms present in the ground state. Some passages are thus necessary to properly count the excited atoms. Three pulses are used, the first pulse measures the atoms that remained in the ground state after spectroscopy (P_g). The second one, since the excited atoms are in the metastable excited state $^3P_0$, detects the background florescence caused by scattered light and hot background gas atoms (P_b). To bring the atoms excited during spectroscopy back to the ground state we exploit the short-lived $^3D_1$ level which has a strong decay channel to $^1S_0$. To do that we apply a pulse of 10 mW of resonant 1389 nm light for 6 ms which optically pumps the atoms to the ground state with 90 % of efficiency. Lastly, a third 399 nm pulse detects these atoms which represents the excited fraction (P_e).

The typical signal obtained from this process is reported in fig. 5.3. The signal is then used to calculate a normalized excitation fraction ψ and the total number of atoms N as:

$$\begin{aligned} \psi &\equiv \frac{|e\rangle}{|e\rangle + |g\rangle} \approx \frac{P_e - P_b}{P_e + P_g - 2P_b} \\ N &= |e\rangle + |g\rangle \approx P_e + P_g - 2P_b \end{aligned} \tag{5.2}$$

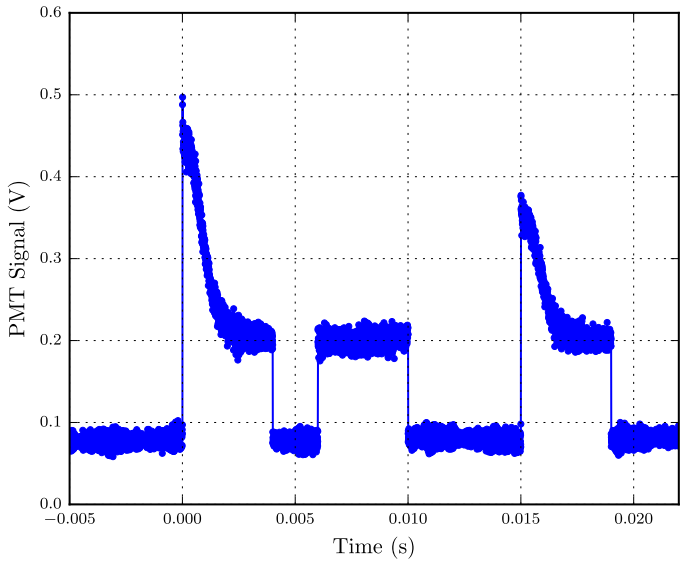

Figure 5.3: Typical detection signal collected by the PMT and recorded by an oscilloscope. The three pulses are clearly visible, the first one, on the left, is proportional to the ground state population. The central feature is the background level while the feature on the right is the signal from the optically pumped excited state atoms. From [76].

where $|g\rangle$ and $|e\rangle$ are the number of atoms in the ground and excited state respectively while P denotes the PMT signal.

5.1.6 Clock sequence

Figure 5.6 summarizes the typical clock sequence. The clock is controlled by a PC program which sends TTL and analogue signals to control the laser pulses, integrates the signals from the PMT and handles the clock laser frequency to make sweeps or to lock it to the atomic resonance. The first step is loading the blue MOT for150 ms. During this time the slower beam and the blue and green MOT beams are kept on while the lattice laser is maintained on for the entire cycle duration. To transfer the atoms in the green MOT the blue light is shut off. The three sub-steps of the green MOT last for a total of 60 ms after which the green light is turned off and the atoms are loaded in the lattice. At this point the spin polarization process takes place. In 15 ms the bias magnetic field is ramped up to 0.4 mT along the z axis before illuminating the atoms with a 556 nm pulse for 1 ms to spin polarize the sample into one of the two Zeeman magnetic ground state sub-levels. The specific sub-level is selected using the PC program which sets the corresponding RF frequency on the AOM (clock AOM in fig. 5.1). Subsequently,

the bias magnetic field is reduced to 0.14 mT to induce a 290 Hz Zeeman splitting between the spectroscopic features (see fig. 5.4). 30 ms are required to switch the current and wait for the magnetic field to stabilize. At this point the atomic sample is ready for spectroscopy. The Rabi pulse has a typical duration of 60 ms during which all the radiation, except for the lattice, are blocked to avoid any disturbance in the trapped atoms. After 5 ms the detection phase begins. The three pulses are 4 ms long and spaced by 2 ms the respective PMT signal is digitally integrated for 2 ms. Before the last detection pulse the repumper laser shines the atoms for 5 ms. The sequence then restarts, the total cycle length is around 350 ms.

The lock on the spectroscopic line is executed by alternatively interrogating the two sides of the resonance. From the difference of the excitation fraction between the two sides the error signal is obtained. This is then transformed in a frequency correction by applying a multiplicative factor that sets the gain of the control. The PC program elaborates the data from the PMT and controls the clock laser frequency. To remove the first order Zeeman shift and the vector light shift, the clock laser is locked on both Zeeman components independently for a total of four interrogations, two per each line.

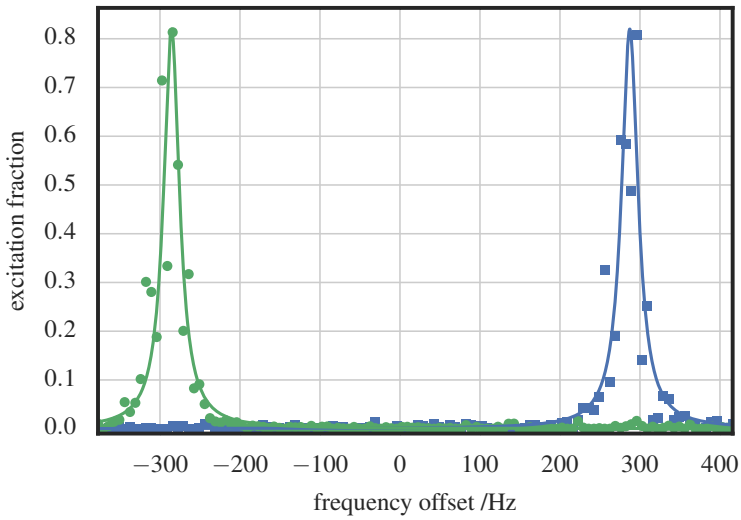

Figure 5.4: Measured clock transition in presence of a bias magnetic field of 0.14 mT with atoms polarized in the $m_F = +1/2$ state (green trace) or $m_F = -1/2$ (blue trace). From [25].

Sideband spectroscopy To get informations about the quality of the optical trap we performed a broadband spectroscopy scanning the clock transition for several tens of kilohertz like reported in fig. 5.5. This kind of trace is called sideband spectrum and from that the trap depth and the temperature of the trapped atoms

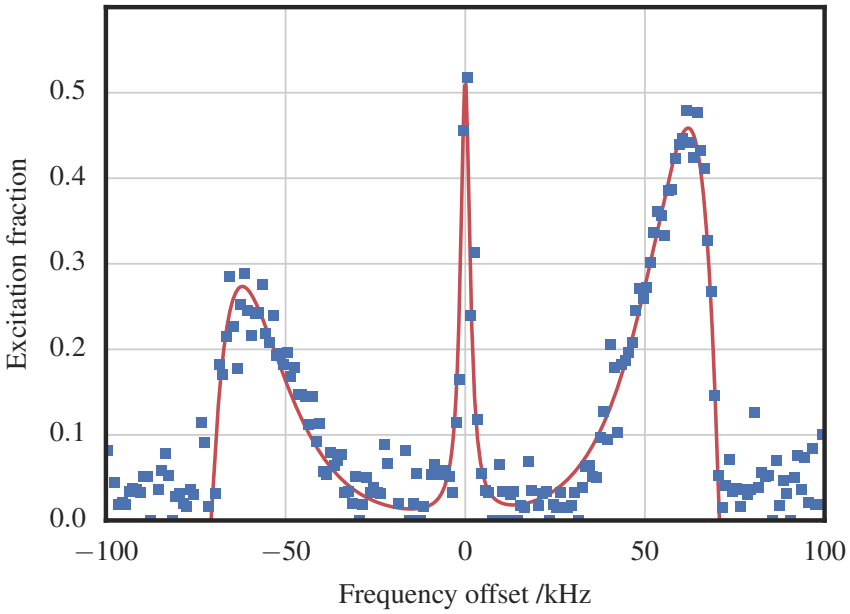

Figure 5.5: Sideband spectroscopy of the clock transition taken with 10^4 atoms trapped in the optical lattice and in a single clock laser scan. It shows the carrier line and two motional sidebands with the combined fit (red trace). From [25].

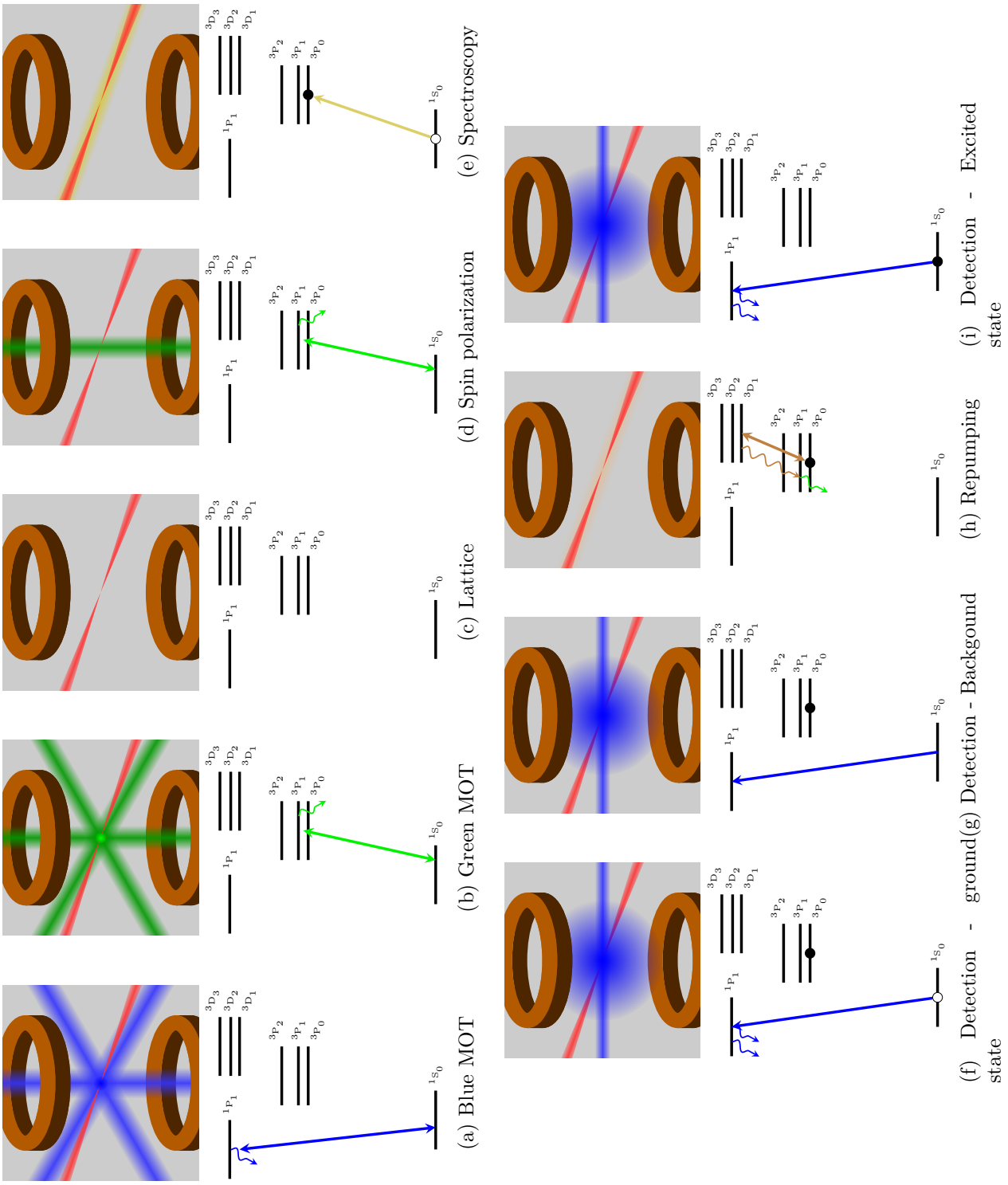

Figure 5.6: Complete clock sequence steps.

can be estimated. The longitudinal motional frequency ν_z is linked to the trap depth U_0 by[85]:

$$h\nu_z = 2E_r\sqrt{\frac{U_0}{E_r}} \tag{5.3}$$

where E_r is the photon recoil energy at 578 nm and h is the Plank's constant. From the ratio of the two sidebands b_{br} the longitudinal temperature of the trapped atoms T_z can be inferred:

$$k_{\mathrm{B}}T_z = \frac{h\nu_z}{\ln b_{br}}. \tag{5.4}$$

The points in fig. 5.5 are fitted with the expected shape for the carrier and sidebands taken from [85]. The result is a trap frequency of $\nu_z = 68.6(3)\,\mathrm{kHz}$ which corresponds to a trap depth of $U_0 = 284(3)\,\mathrm{E_r}$. The longitudinal temperature is $T_z = 7.0(14)\,\mu\mathrm{K}$. The typical working conditions are a trap depth of $200\,\mathrm{E_r}$ and a longitudinal temperature of about $7\,\mu\mathrm{K}$.

5.2 Instability measure

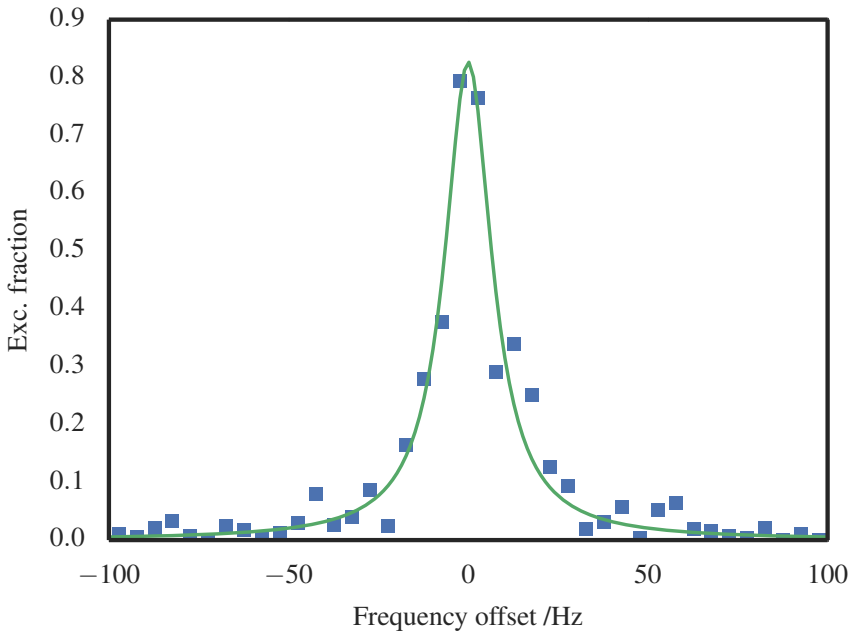

Figure 5.7: Spectroscopy of a spin polarized single Zeeman component of the clock transition. The trace is a lorentzian fit with a linewidth of 18 Hz. From [25].

The usually measured clock transition line is reported in fig. 5.7. It shows a line 18 Hz wide, limited by an excess of clock laser frequency noise attributed to

the seismic noise on the ultra-stable cavity not properly rejected by the passive anti-vibration platform and the vibration insensitive support.

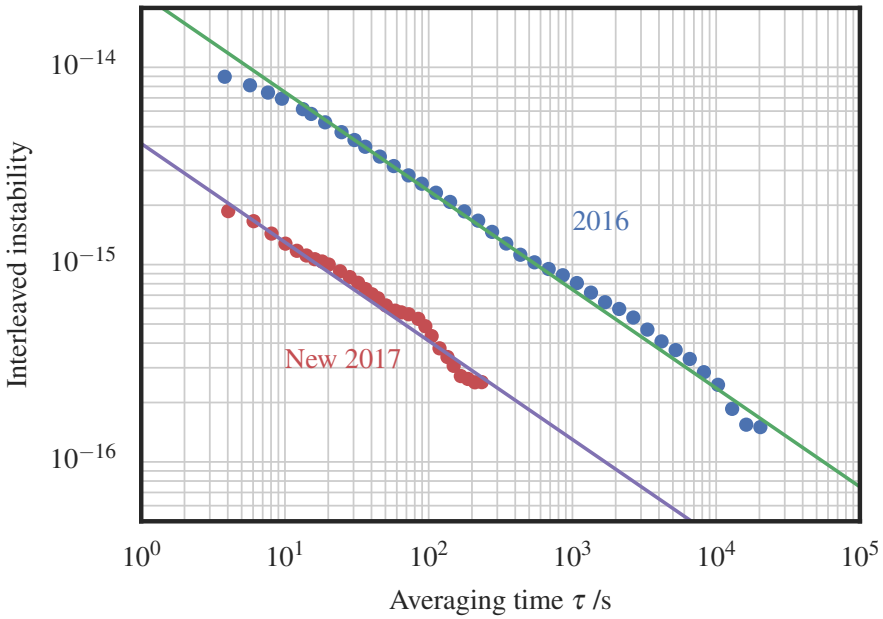

Figure 5.8: Measured instability of the clock as it was during 2016 and with the upgraded set up.

The instability was measured by interleaving two identical clock cycles accumulating two independent frequency corrections. Assuming the two interleaved states with equal instability, it can be computed by taking the difference between the two frequencies and computing the Allan-Deviation. The outcome is reported in figure 5.8 and shows a fractional frequency instability of 2.3×10^{-14} at 1 s averaging down as white frequency noise, limited by the clock laser instability.

Upgraded system preliminary instability The clock laser cavity as well as the 578 nm laser generation was upgraded at the end of 2016 (see sec. 3.3.5). The upgraded set up was preliminary tested during the spring of 2017 obtaining a spectroscopic feature 7 Hz wide with an extended Rabi spectroscopy time of 85 ms. The instability improved to $4 \times 10^{-15}/\sqrt{\tau/s}$ which is aligned to the expected level of performance of the cavity used.

5.3 Uncertainty budget

Before undertake an absolute frequency measurement the system has to be carefully characterized in order to quantify all the systematic effects which alter

Table 5.1: Uncertainty budget for the Yb optical lattice clock. From [25].

Effect	Shift. /Hz	Unc. /Hz	Rel. Shift$\times 10^{17}$	Rel. Unc.$\times 10^{17}$
Lattice polarizability	-0.02	0.04	-4	8
Nonlinear lattice shifts	-0.07	0.05	-12	10
Density shift	-0.01	0.03	-2	6
Zeeman shift	-0.14	0.02	-27	4
BBR room	-1.219	0.013	-235.3	2.5
BBR oven	-0.011	0.004	-2.1	0.8
Probe light shift	0.005	0.018	1.0	3.5
Background gas shift	–	0.008	–	1.5
Static Stark shift	–	0.005	–	1
Servo error	–	0.006	–	1
Tunnelling	–	0.002	–	0.4
Line pulling	–	0.002	–	0.4
AOM switching	–	0.0005	–	0.4
Fiber links	–	0.0005	–	0.1
Gravitational redshift	13.474	0.003	2601.2	0.6
Total	12.02	0.08	2320	16

the unperturbed clock transition. The different perturbations are summarized in a table (see tab. 5.1) realizing the complete uncertainty budget evaluation of the clock.

The clock final fractional uncertainty is 1.6×10^{-16}. To assess and quantify every single source of uncertainty we operate the clock interleaving two clock sequence varying a single parameter, enhancing the effect under test, and registering the resulting frequency shift of the clock transition. Every shift, along with its uncertainty, is extrapolated to the actual experimental conditions by performing interpolations to the experimental data.

5.3.1 Lattice light shift

The largest systematic source of uncertainty comes from the optical trapping potential which, as described in sec. 2.2.2, induces a large perturbation on the atomic energy levels. The shift depends on both the lattice intensity and lattice laser frequency ν_l and it is described by eq. (2.27). We can re-write it in terms of the effective trap depth $U_e = \xi U_0 = \xi \alpha_{E1} I$ seen by the atoms and expliciting the c coefficients as done in [28]:

$$\begin{aligned}\Delta\nu_{ls} = &- \left(a\Delta\nu + \frac{3}{4}d(2n^2+2n+1)\right)\frac{U_e}{E_r} - d\left(\frac{U_e}{E_r}\right)^2 + \\ &+ (a\Delta\nu - b)\left(n+\frac{1}{2}\right)\left(\frac{U_e}{E_r}\right)^{1/2} + d(2n+1)\left(\frac{U_e}{E_r}\right)^{3/2}\end{aligned} \tag{5.5}$$

where $E_r = (\hbar k)^2/2m$ is the photon-recoil energy, $\Delta\nu_L$ is the lattice frequency detuning from the E1 magic frequency, $a = \frac{\partial \Delta\alpha_{E1}}{\partial \nu}$ is the slope of the differential E1 polarizability at ν_{E1}, b is the the combined multipolarizability contribution, d derives from the hyperpolarizability $\Delta\gamma$ and n is the lattice vibrational level occupied by the atoms.

Experimentally, we evaluated the scalar shift by interleaving low $U_0 = U_L$ and high $U_0 = U_H$ trap depth clock sequences at different lattice laser frequency and correcting the obtained shift with non linear term coefficients, b (multipolar polarizability) and d (hyperpolarizability), taken from [86, 28].

The trap depth modulation is induced varying the lattice power by changing the diffraction efficiency of the AOM present in the lattice distribution bench before the optical fiber (see fig. 3.9). In this way the beam shape quality and the spectrum of the Ti:sapphire laser are not degraded. In particular, the atoms are always loaded at $U_L \approx 200\,\mathrm{E_r}$ and then, in the case of high trap depth, is quickly ($\sim$0.1 ms) raised up to $U_H \approx 300\,\mathrm{E_r}$ before spectroscopy. A fast photodiode (3 GHz bandwidth) monitors the lattice laser single mode. A multi-mode operation would result in amplitude modulation noise which can be directly seen from the photodiode signal on a spectrum analyser. Before each clock measurements, the lattice laser absolute

frequency is taken using an optical frequency comb while, during the experiment, the frequency drift is compensated by locking the frequency to the comb.

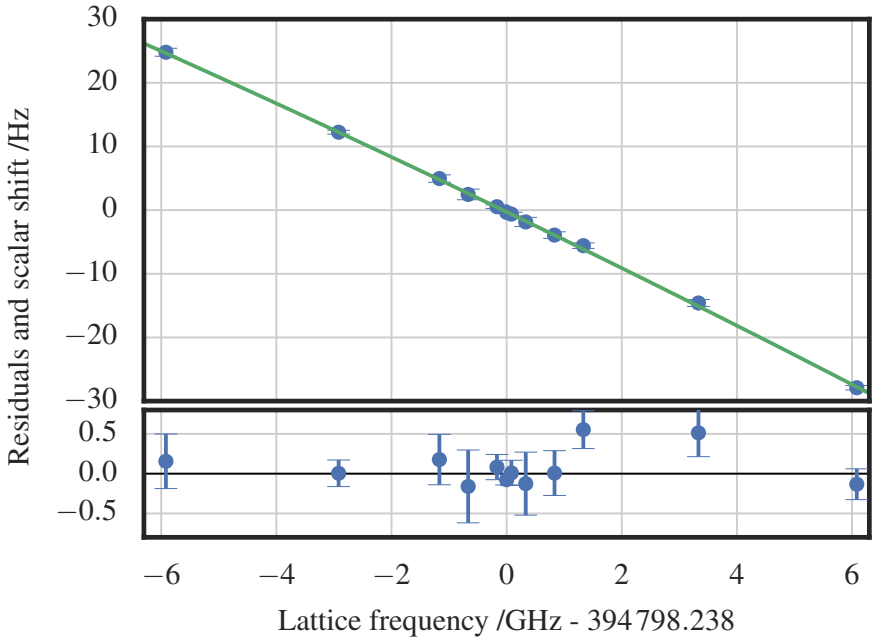

Figure 5.9: Scalar lattice light shift. From [25].

The operational lattice frequency was set at 394 798.238 GHz. At this frequency we evaluated the light shift by interleaving between low $U_L = 196(4)\,\mathrm{E_r}$ and high $U_H = 348(5)\,\mathrm{E_r}$ trap depth and assuming the shift scaling linearly between the two states. The obtained value at U_L is $-0.02(4)$ Hz, has to be corrected to account for non linear effects. The detail of the trapping condition, like the trap depth U_e and the average motional state occupation in the lattice n, are evaluated from the sideband spectra (see fig. 5.5). In the typical operational condition we have $\xi = 0.8(1)$ and $n = 2.1(10)$ at U_L and $n = 1.5(8)$ at U_H. We calculated the hyperpolarizability and the multipolar shift using coefficients from literature[28] and using eq. (5.5) obtaining a correction of $0.064(32)$ Hz, on top of that we corrected for the non linearity in the effective shift between U_L and U_H estimated to be $-0.13(6)$ Hz. These two elements sum to a final shift of $-0.07(5)$ Hz which constitutes the largest contribution to the final uncertainty budget due to the uncertinty in the multipolar and hyperpolarizability coefficients at high trap depth.

To assess the lattice magic frequency, we also investigated the light shift as a function of the lattice frequency. In figure 5.9 are reported the measured shift obtained interleaving between $U_L = 208(2)\,\mathrm{E_r}$ and $U_H = 333(4)\,\mathrm{E_r}$ for different lattice laser frequency ν_l and scaling the data at $U_0 = 200\,\mathrm{E_r}$. The data are interpolated with a second order polynomial expansion having linear coefficient

$a = -27(3)\,\mathrm{mHz\,GHz^{-1}}$ and a quadratic term $c = -0.016(30)\,\mathrm{mHz^2\,GHz^{-1}}$ which results in a shift of $c\Delta\nu^2 U_e/E_r$. We evaluated the so called $E1$-magic frequency, which is the frequency which zeroes the scalar shift corrected for the multipolar couplings (magnetic dipole and electric quadrupole), using the light shift obtained at the working point along with the linear term a and extracting the zero crossing point. This frequency is then corrected using the non linear contribution also used for the operational lattice frequency. The final value is $\nu_{E1} = 394\,798.205(17)\,\mathrm{GHz}$. This result is not consistent with the previously reported values for Yb clock [87, 28]. We attribute this discrepancy to the spectral purity of the titanium-sapphire laser that was not filtered. A new Bragg filter, which should lift this discrepancy, has been installed in the optical set up (see fig. 3.9) and is currently under characterization.

5.3.2 Density shift

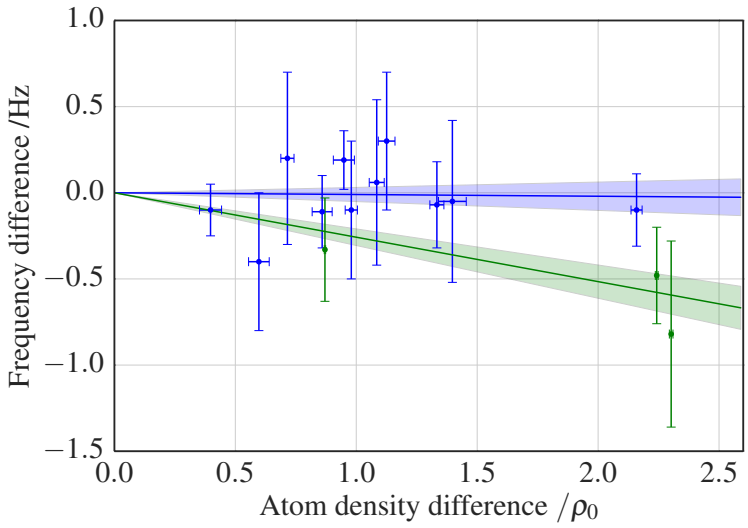

Figure 5.10: Density shift measured with 0.39(2) excitation number (blue points) and at 0.34(2) (green points). The line represents the fit with respect to the same color dataset while the shaded region is the statistical uncertainty.

Cold collisions take place among trapped atoms inducing a perturbation in the clock laser transition which depends on the atomic density. When the atomic sample is spin polarized the atoms are prepared in the same quantum state. Given the fermionic nature of ^{171}Yb, the Pauli exclusion principle induces a suppression of the s-wave scattering channel. The shift is thus dominated by p-wave cold collision [50]. However, inhomogeneity of the Rabi pulse can still bring a small amount of s-wave scattering.

To evaluate this systematic effect we measure the frequency shift between clock cycles with different atomic population. We modulate this parameter by changing the duration of the blue MOT loading. In this way, assuming the atomic density proportional to the number of trapped atoms, the density in varied without affecting the trapping conditions. Moreover, cold collisions also depends on the excited fraction of the atomic sample after spectroscopy [88].

To express the data ins convenient to define the atomic density which corresponding to 1 atom per lattice cite ρ_0. To calculate that we consider a trapping region with a radius of 45 µm, from the lattice beam waist, and 0.5 mm long, from the dimension of the second stage MOT giving a volume $V = 3.2 \times 10^{-12}\,\mathrm{m}^3$. The lattice wavelength is 759 nm which generates about $t \simeq 1.3 \times 10^3$ trapping sites along the trap length. If we take 1 atom per lattice cite the resulting density is $\rho_0 = t/V = 4 \times 10^{14}\,\mathrm{m}^{-3}$. The evaluation of the absolute number of atoms present in the trap has an uncertainty of 20 % however, working with ratios gives an uncertainty of 1 % on the relative measurement.

The result of the experimental evaluation of the systematic shift is reported in fig. 5.10, the data were taken interleaving clock cycles with low and high number of spin polarized atoms and with an excitation fraction, measured after spectroscopy, of 0.39(2). The atomic density was varied from $\rho \simeq 0.1\,\rho_0$ to $\rho \simeq 3\,\rho_0$. The experimental points are interpolated with a linear fit without offset obtaining a slope of $-0.01(4)\,\mathrm{Hz}/\rho_0$. Tu underline the effect of the excitation fraction, a second measurement was performed with the same conditions but with a lower excitation fraction namely 0.34(2) obtaining a slope of $-0.4(2)\,\mathrm{Hz}/\rho_0$. This dependence was effectively foreseen by the behaviour of p-wave collisions as described in [88].

The typical operating conditions for the clock are $\rho \simeq 0.7\,\rho_0$ and excitation fraction 0.39(2) giving a density shift of $-0.01(3)$ Hz meaning a fractional frequency uncertainty of 6×10^{-17}.

5.3.3 Zeeman shift

Magnetic fields couple with atoms and perturbs energy levels through the notorious Zeeman effect[8]. As we have seen, this effect plays a fundamental role in atomic clocks like, for example, in atomic manipulation and spectroscopy. However, both first and second-order Zeeman shift alter the clock transition and they require a careful characterization to evaluate an unperturbed transition.

During spectroscopy a bias magnetic field is applied to induce a separation between the two Zeeman components of the clock transition (see fig. 5.4). The typical separation between a Zeeman feature and the unperturbed one is 290.1(3) Hz. Considering a first order magnetic sensitivity for Yb of 210 MHz/T [87], this corresponds to a magnetic field of 138(1) µT. By separately measuring the frequency of the two magnetic components we can measure the stability of the magnetic field. It was found to be lower than $0.1\,\mu\mathrm{Th}^{-1}$. The first order Zeeman shift can be removed

by taking the frequency average between the two magnetic component, exploiting the linearity of the shift with respect to the magnetic field.

The second-order Zeeman effect, in optical lattice clocks, arises from the interaction of the two triplet states $^3P_0$ and $^3P_1$ [7]. The repulsion of the two states gives a shift quadratic with the magnetic field $\Delta\nu = aB^2$ with $a = 7(1)\,\mathrm{Hz/mT^2}$[87]. Operating the clock with a magnetic field of $138(1)\,\mu\mathrm{T}$ gives a $-0.14(2)\,\mathrm{Hz}$ shift, that corresponds to a fractional frequency uncertainty of 4×10^{-17}.

5.3.4 Black-body radiation shift

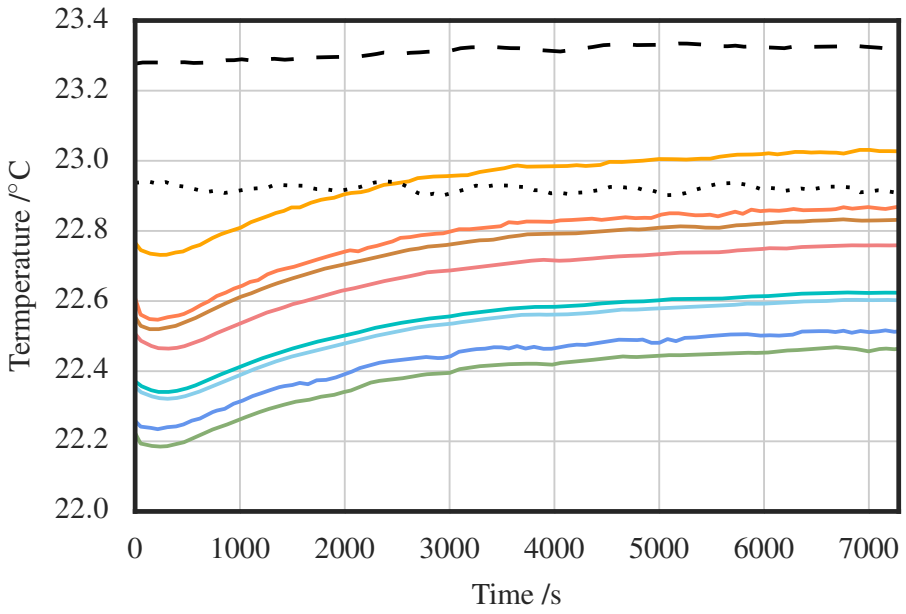

Figure 5.11: Temperature registered by the thermometers spread around the experimental chamber during a single measurement run. From [25].

The experiment runs at room temperature and, as a consequence, the atomic sample is immersed in an environmental thermal radiation which induces a Stark shift on the clock states that perturbs the clock transition. This external electromagnetic field is called back-body radiation (BBR) and, in the case of optical lattice clocks, its characteristic frequency is much smaller than the clock transition allowing the shift to be approximated to a static interaction plus a dynamic correction as [89]:

$$\Delta\nu_{\mathrm{BBR}} = -\frac{1}{2}\left(\alpha^{(0)}_{^3\mathrm{P}_0} - \alpha^{(0)}_{^1\mathrm{S}_0}\right)\langle E^2\rangle_T(1+\eta_{\mathrm{clock}}(T)) \tag{5.6}$$

where the coefficients $\alpha^{(0)}_{|i\rangle}$ are the clock states static polarizabilities, $\langle E^2\rangle_T$ is the time averaged electric field of a black body at temperature T and η_{clock} is the dynamic correction. In the case of ^{171}Yb we have $\Delta\alpha^{(0)} = \left(\alpha^{(0)}_{^3\text{P}_0} - \alpha^{(0)}_{^1\text{S}_0}\right) = 36.2612(7)\,\text{kHz}/(\text{kV/cm})^{-2}$ and $\eta(T = 300\,\text{K}) = 0.0179(5)$ [89, 90]. The precise knowledge of the temperature sensed by the atoms is crucial as the integration of the Planck's radiation law yields $\langle E^2\rangle_T = (831.9\,\text{V m}^{-1})^2[T/(300\,\text{K})]^4$, expliciting a T^4 dependency.

The temperature of the experimental chamber and the oven is continuously monitored by ten calibrated platinum resistance thermometers (Pt1000, uncertainty 0.2 K) placed around the vacuum chamber. Eight of those are positioned around the trapping region while one is placed close the oven and the last far from it. The main heating sources are the oven, the MOT coils and the water cooling, these generate temperature gradients across the chamber. The temperature is read by 4-wires resistance reading with an uncertainty of 0.04 K. The spread between all the sensors is below 2 K. An example of the temperature measured during the operation of the clock is reported in fig 5.11, it shows a transient at the beginning of the experiment caused by the thermalisation of the apparatus.

To evaluate the environmental temperature seen by the atoms, we assumed a uniform probability density function considering the average of the recorded temperatures in a single run, $T = (T_{\max} + T_{\min})/2$ and the uncertainty $((T_{\max} - T_{\min})/\sqrt{12}$ [91]. The main limiting factor in every single measurement run is given by the temperature transient. When all the measures are statistically analysed considering their correlations (see sec.5.4), the resulting uncertainty is 0.8 K. The BBR shift caused by the environmental temperature is thus $-1.219(13)$ Hz.

As described in chapter 3.1, the trapping region lies on the axis of the atomic beam coming from the hot oven, therefore this constitutes an additional thermal radiation source. On top of that, during the first part of the campaign, on the opposite side of the oven a hot window was present to give optical access to the slower beam, with direct sight to the atomic sample. This window was heated at 230(5) °C and its radiation has to be taken into account as well. To address these effects, we performed a ray tracing analysis to calculate the effective solid angle subtended by the thermal source (considering also radiation reflections in the vacuum chamber) as perceived by the atoms. The oven is kept at a temperature of 400(10) °C and constantly monitored with a thermocouple. The uncertainty in the evaluation arises from the difference in temperature between the body and the tip of the oven and the sensor position as well as the thermocouple accuracy. The BBR coming from the oven has to pass through the copper differential vacuum tube, present between the oven and the experimental region (see chapter 3.1). The result of this model, after considering a copper emissivity of $\epsilon_{\text{Cu}} = 0.4(2)$ and the possibility of the radiation to make up to two reflections before getting on the atoms, is a BBR shift of $-0.011(4)$ Hz.

As far as the hot window is concerned, in the analysis we considered up to 5

reflections from the stainless steel fitting surfaces (emissivity $\epsilon_{\text{steel}} = 0.5(3)$) and 1 from the polished aluminium chamber (emissivity $\epsilon_{\text{Al}} = 0.13 \pm 0.1$) obtaining a shift of $-0.12(15)$ Hz. The hot window was removed during March 2016, an intra cavity cold mirror was installed in its place. This additional source of uncertainty was evaluated to be 5×10^{-17} by looking to the final relative uncertainty budget after averaging data with and without the hot window.

5.3.5 Probe light shift

The interaction between the atoms and the clock laser light during the spectroscopy pulse induces, in turn, a Stark shift on the clock transition. The shift depends on the laser intensity and, in the case of a Rabi π pulse, the required amount of light scales as $I_\pi \propto t_i^{-2}$ [28], with t_i the interaction time. In our analysis we referred to the published value for Yb [87] and rescaled it to our experimental condition. For a spectroscopy pulse of 70 nW and 60 ms long the probe light induced Stark shift is 0.005(18) Hz.

5.3.6 Gravitational red-shift

According to special relativity and the equivalence principle, a difference in the gravitational potential between an event (one clock) and an observer (reference clock) gives a time dilation that results in a difference in time flow [92]. In the case of frequency standards, this means that the frequency measured by two clocks positioned at different height (Δh) are shifted by $\Delta\nu/\nu_0 = g\Delta h/c^2$ where g is the local acceleration of gravity. The magnitude of such an effect is $\Delta\nu/\nu_0 \simeq 10^{-17}$ for an elevation difference of $\Delta h = 10$ cm.

When a comparison between clocks is performed, a careful evaluation of the gravitational red-shift is necessary to avoid an offset in the resulting frequency. If the two clock are in the same laboratory the difference in height can be easily measured with high precision. On the other hand, when clocks are positioned far away from each other, the same measure could result cumbersome, yielding to an additional uncertainty contribution in the gravitational potential determination. Indeed, for remote clock comparisons like in the generation of international timescales, every measurement is reported to the altitude with respect to the geoid. The evaluation of the gravitational potential with respect to the geoid at the INRIM's laboratories was undertaken in 2013 within the European project 'International timescales with optical clocks' (ITOC) [93, 94]. We consider here the results obtained with the Global Navigation Satellite System/geoid (GNSS/geoid) method because is better suited for long-haul optical fiber and satellite clock comparisons given it smaller accumulated error over long distances (> 1000 km) compared to the traditional levelling method [95]. The gravitational potential at the height of the Yb

atomic cloud is $C(\mathrm{Yb})_{\mathrm{GNSS/geoid}} = 2336.48(27)\,\mathrm{m^2 s^{-}2}$ [25] causing a gravitational red-shift of 13.474(3) Hz.

During the absolute frequency measurement of the Yb clock transition against the caesium fountain the two clocks were located in the same laboratory, within 10 m of separation. We assessed a height difference of $\Delta h(\mathrm{Yb{-}Cs}) = 0.15(2)\,\mathrm{m}$ resulting in a gravitational red-shift during the comparison of $1.6(2) \times 10^{-17}$.

5.3.7 Other shifts

Several other marginal effect are considered to complete the uncertainty budget.

Fiber noise cancellation, residual Doppler and AOM chirp As already mentioned in section 3.3.5, the Doppler noise cancellation system introduces a fractional uncertainty of 1×10^{-18} after 1000 s of operation. However, the reference mirror of the compensation system, that is the mirror mounted on the experimental bench which sends the light back to the fiber, is placed 30 cm away from the lattice back-reflector. This back-reflector, instead, constitutes the reference frame of the trapped atoms in the lattice. As a consequence, vibrations that shake the chamber and the optical table (e.g. MOT coils switching and water cooling) can induce an additional Doppler shift because the trapped atoms move with respect of the probe light wave-fronts. The assessed relative uncertainty is 5×10^{-17}.

The frequency of the clock laser is modulated by means of an AOM, to avoid thermal effects on the crystal of the modulator we switch the frequency at constant power. By performing heterodyne interferometry we did not observed any shift up to 2 mHz that is taken as uncertainty. Moreover, changing frequency on the AOM to switch the Rabi pulse induces causes a phase jump not compensated by the fiber-noise cancellation system [96]. This results in a frequency shift of 0.5 mHz which we consider as uncertainty.

Servo error The atomic servo loop stabilizes the clock laser frequency on the atomic resonance by probing both $m_F = \pm 1/2$ components. However, any effect preventing this process result in a systematic frequency drift of the recorded transition. This is the case of uncompensated linear drift in systematics or local oscillator. We evaluated this disturbance by taking the average of error signal during measurements of the campaign obtaining an uncertainty of 1×10^{-17}.

DC Stark Stray electrical charges in the proximity of the trapping region would induce a Stark shift on the clock transition [89]. In our setup the vacuum chamber is aluminium made and act as a Faraday cage, shielding the atoms from external fields. On the other hand, electrical charges can build up on the windows surfaces [97]. Two big view-ports are present 25 mm away from the trapping region, along the

vertical axis of the chamber, having 38 mm of radius and 12 mm of thickness. We evaluated a capacitance between the two windows of 0.6 pF and a time constant of ~ 50 d considering a high resistivity of $10^{18}\,\Omega\,\mathrm{m}$ for fused silica [97, 25]. At the time of the evaluation, the vacuum chamber was used by three years thus the potential charges accumulated on the windows surfaces should have decayed yielding to a shift $< 1 \times 10^{-17}$ that is considered as uncertainty.

Background Gas collisions The residual gas particles present in the vacuum chamber and the hot atoms from the atomic beam can collide with trapped atoms inducing a shift. This effect can be related to the lifetime of the atoms in the lattice [98]. We consider a typical lifetime of 2.7 s and a C_6 coefficient for Yb dimers taken from [99] obtaining a shift of 8 mHz that we adopt as uncertainty.

Tunneling Atoms can move from one lattice cite to the adjacent by means of quantum tunneling effect, causing a broadening of the motional levels structure of the trap [100]. Tunneling is suppressed operating the lattice at large trap depth. With a potential $U_0 = 200\,\mathrm{E_r}$ deep and a temperature of $T = 7(3)\,\mu\mathrm{K}$ we estimated that about 70 % of the atomic sample lies in the lowest three vibrational levels of the lattice. We consider the width of the third band as uncertainty that is 2 mHz.

Line pulling The presence of atomic transitions close to the spectroscopic feature induces a small effect called line pulling. This arises from the convolution of the resonance under test and a tail of a nearby transition, the sum of the two leads to a shift of the peak centre toward the disturbing line. In the case of a Yb clock we have the influence of the lattice motional sidebands (see fig. 5.5) and the σ clock transition. For the former we gave an upper limit using [101]:

$$\delta\nu_{\mathrm{pull}} = \sqrt{b}\frac{\Delta^2}{\delta} \tag{5.7}$$

where Δ is the linewidth, δ is the frequency separation between the carrier and the sideband and b is the ratio between the carrier and the sideband. Considering a spectroscopy line 20 Hz wide, 70 kHz separation and a ratio of 0.88 we obtain a shift of 5(2) mHz. However, assuming a similar but opposite line pulling from both sidebands, the net effect is a zero shift with an uncertainty of 2 mHz. In the case of σ clock transitions these are suppressed by the linear polarization of the probe light and the spin polarization of the sample further reduce this effect that results to be negligible in our system.

5.4 Absolute frequency measure against ITCsF2

The absolute frequency of the ^{171}Yb optical frequency standard was measured with respect to the INRIM primary frequency standard, the caesium fountain

IFCsF2, during a campaign started in January 2016 and finished at the end of May 2016. To bridge the frequency gap between the microwave standard ($\sim$ 9 GHz) and the optical lattice clock ($\sim$ 500 THz) an Er-fiber optical frequency comb is adopted. It operates with a repetition rate of 250 MHz referenced to a hydrogen maser. The fountain operated continuously during the campaign and counted the hydrogen maser frequency.

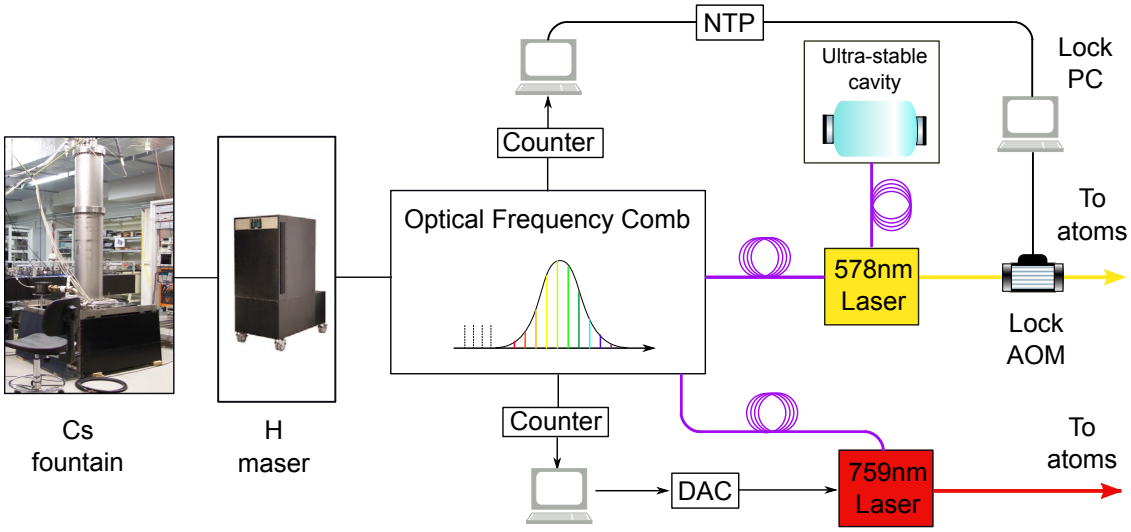

Figure 5.12: Layout of the absolute measure of the ^{171}Yb clock transition against the primary frequency standard, the caesium fountain ITCsF2. The 578 nm light, stabilized on the ultra-stable cavity is sent through PM fibers (purple lines) to an optical frequency, referenced to an hydrogen maser, comb where its frequency is counted and recorded on a dedicated PC. At the same time the fountain measures the maser frequency. Lock PC is used to lock the laser frequency on the atoms and it records the frequency sent to lock AOM (see main text for details). The scheme of the lattice leaser frequency lock to the comb is also illustrated.

A diagram showing the measurement setup is reported in fig. 5.12. From the clock laser distribution bench a fraction of light, frequency stabilized on the ultra-stable cavity, is sent to the frequency comb through a PM fiber. The fiber link is actively stabilized to compensate for additional phase noise (see sec. 3.3.5) introducing an uncertainty of 1×10^{-18} after 1000 s of measurement. The beatnote frequency of the laser and the comb tooth was counted redundantly to avoid cycles slips in the counter. We removed points with a discrepancy between the different counters reading larger than 2 Hz. The light sent to the comb is stabilized on the cavity and has a different frequency with respect to the laser beam sent to the atom, as this is steered by an additional AOM (lock AOM). The frequency measured by the comb and the one driving the lock AOM are recorded on two separate computers at different rate because the comb and the clock records data operates

with different cycle time. The two computers are connected to the INRIM' Network Time Protocol (NTP) server and are synchronized within 3 ms. The collected data are averaged and interpolated at common timestamps and, considering a cavity drift of $0.1\,\mathrm{Hz\,s^{-1}}$, the uncertainty relative at this operation has been calculated as 6×10^{-19}.

To evaluate the uncertainty introduced in the measurement by the comb we measured the same optical frequency with two independent optical combs, obtaining an uncertainty of 1×10^{-16} after averaging for 10^4 s, limited by the electronic noise of the comb setup.

The characterization of the cryogenic caesium fountain ITCsF2 has been already reported in [13]. During the data taking period the fountain run in two distinct regimes, respectively, high and low atomic density. The former exhibits an accuracy of 4.8×10^{-16} and an instability of $2.5 \times 10^{-13}/\sqrt{\tau/\mathrm{s}}$ while in the low atomic density the uncertainty reduces to 3.0×10^{-16} and the instability goes up to $3.6 \times 10^{-13}/\sqrt{\tau/\mathrm{s}}$.

During the campaign we collected data for 227 h in a total of 31 runs. The result of all the different measurements is reported in fig. 5.13 as a function of the date (modified Julian date MJD). Given the fountain different operative regimes as well as the variations in atomic density in the optical standard, the systematic uncertainty related each point is different but always limited by the fountain contribution. In addition, the removal of the hot window (see sec. 3.1) during the campaign brought a reduction in the BBR uncertainty of the Yb clock as can be seen in fig. 5.13 after ten measurements.

The statistical analysis of the whole data took into account the correlations between the different measurements with different shifts [102] and followed the Gauss-Markov theorem [103, 104]. The result of the analysis gives a frequency of the unperturbed $^1\mathrm{S}_0 - {}^3\mathrm{P}_0$ transition of ^{171}Yb of $f_{^{171}\mathrm{Yb}} = 518\,295\,836\,590\,863.59(31)$ Hz and the detail of the different uncertainty contributions is reported in tab. 5.2. From the correlation matrix we obtained a reduced chi squared of $\chi^2_{\mathrm{red}} = 1.36$ for an average with 30 degrees of freedom. The resulting p-value is 10 %. Considering the detailed uncertainty budget, the measurement is limited by the primary frequency standard contribution of 4×10^{-16} while the optical has been characterized at a level of 1.6×10^{-16} as reported in chapter 5. The statistical uncertainty contributes with 3.4×10^{-16}. However, this value was increased to 3.9×10^{-16} to compensate for the $\chi^2_{\mathrm{red}} > 1$.

The result is in good agreement with the recommended ^{171}Yb frequency as secondary representation of the second $f_{^{171}\mathrm{Yb}}(\mathrm{CIPM2015}) = 518\,295\,836\,590\,864.0(10)$ Hz and it constitutes the first absolute measurement of a Ytterbium optical lattice clock in Europe. In fig. 5.14 the obtained frequency is compared with previous measurements along with the weighted average of the ensemble. Points reported in figure are obtained against caesium frequency standards [87] or derived from

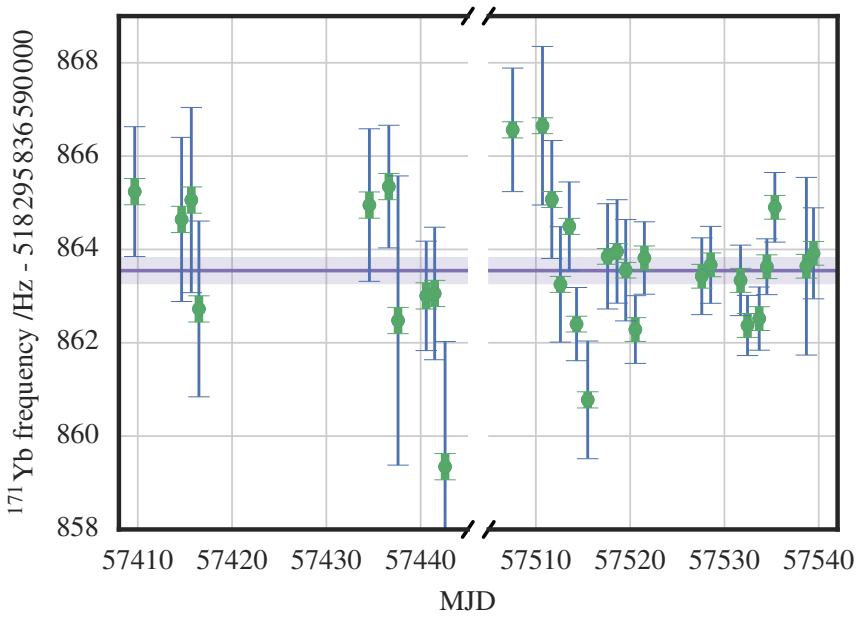

Figure 5.13: Absolute frequency measurements of the $^1S_0 - {}^3P_0$ transition of ^{171}Yb taken against ITCsF2. Data obtained during the measurement campaign from January to May 2016. Blue error bars represent the combination of statistical and systematic uncertainties in each run while the green bars represent the combined systematic uncertainty of the Yb clock and the fountain. The shaded region denotes the 1σ uncertainty of the averaged data. From [25].

Table 5.2: Detail of systematic contributions of the Yb-ITCsF2 comparison. From [25].

Contribution	Unc. /Hz	Frac. Unc.$\times 10^{16}$
ITCsF2	0.20	3.9
Statistics	0.18	3.4
Yb	0.08	1.5
Comb	0.05	1.0
Grav. redshift	0.001	0.02
Fiber link	0.0005	0.01
Synchronization	0.0003	0.006
Total	0.28	5.4

frequency ratio with ^{87}Sr optical frequency standards [28, 105, 106] or with comparison against terrestrial time (TT) [29, 107, 108, 109]. To obtain the ^{171}Yb frequency from the frequency ratio we used the CIPM recommended frequency of

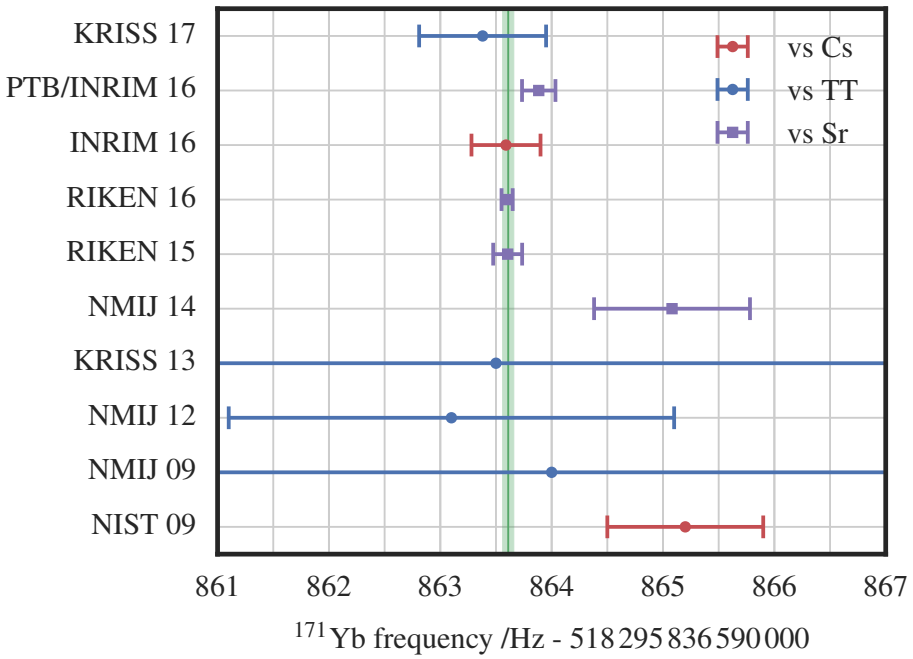

Figure 5.14: Comparison between the different absolute measurement of the Yb clock transition. In red are the direct measurements against Caesium standards, in purple are data deducted from frequency rations ^{171}Yb/^{87}Sr and in blue are measurement taken with respect to the Terrestial Time.

^{87}Sr $f_{^{87}\mathrm{Sr}}(\mathrm{CIPM2015}) = 429\,228\,004\,229\,873.2(2)$ Hz as secondary representation of the second [30]. It worth notice that this result represents the second measurement of a ^{171}Yb clock against a primary frequency standard ever performed after the one done by NIST in 2009, posing a very important metrological milestone for the experiment.

Chapter 6

Ytterbium optical clocks at NIST

National Institute of Standards and Technology (NIST) is one of most important metrological institutes in the world and its research represents the *state-of-the-art* in many fields, especially atomic physics and time and frequency metrology. I have been guest researcher for nine months, during 2016, of the Optical Frequency Measurement (OFM) Group at NIST in Boulder, Colorado. This group conducts several experiments such as the development of optical clocks [110], frequency combs for frequency comparisons, ultra-low noise microwave generation [111] and spectroscopy [112] as well as the development of ultra-stable optical cavities for laser stabilization [113]. In particular, a Ytterbium (Yb) optical lattice clock has been running since 2005 [87, 114, 90, 21] and now the experiment counts two Yb clocks which exhibit performances among the best in the field [21]. My advisors have been Dr. C. Oates, leader of the OFM Group and Dr. A. Ludlow, leader of the Yb experiment.

During my stay at NIST I have been involved in many laboratory activities in particular, the measurement of the uncertainty budget of one clock (YbI) and the realization of the zero-dead-time clock (ZDT clock) and its instability measurement. Besides, I worked on the losses characterization of the new crystalline mirrors (CM), which are going to be used for a new generation ultra-stable optical cavity.

This chapter is organized as follows: firstly the experimental layout of the two clocks is described, then the uncertainty budget evaluation is reported and after that the ZDT clock is shown along with the fundamental aspects of the aliasing effect called Dick effect [68]. Finally the work on the CM is described. The work on the ZDT clock has already been presented in a dedicated publication [21] as well as the lattice light shift evaluation [44].

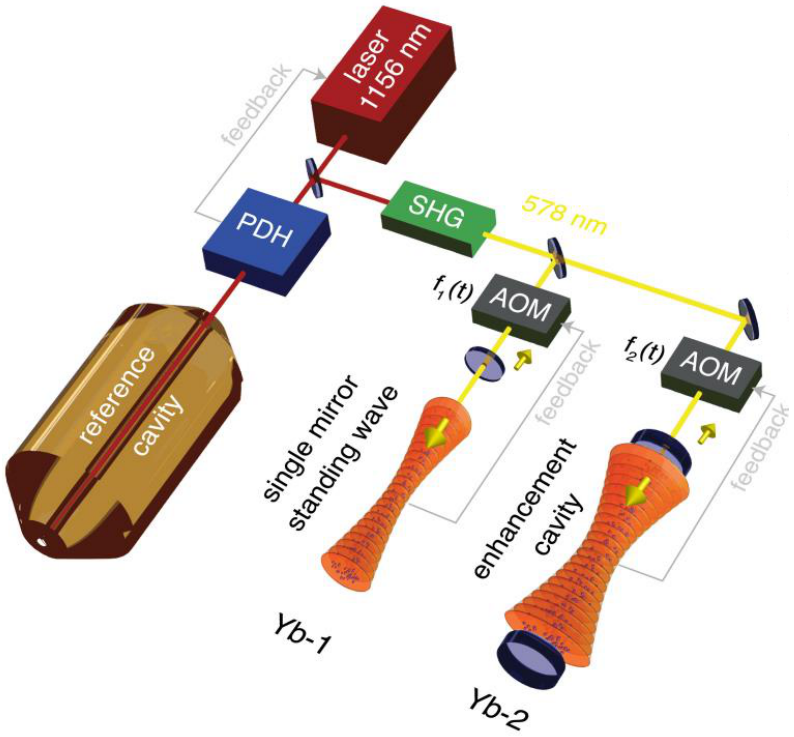

Figure 6.1: Scheme of the experimental setup of the two Yb clocks at NIST. From [21].

6.1 Experimental setup

The NIST Yb experiment consists of two optical lattice clocks referred as YbI and YbII. The experimental setup is sketched in fig. 6.1, the two separate atomic systems share the clock laser source as well as the MOT and lattice lasers while a repumper diode laser is present for each clock (not shown in the picture for simplicity). The main difference between the two clock regards how the lattice standing wave is generated and for the presence on YbI of an atomic shutter. An exhaustive description of the apparatus can be found in [43, 115].

Laser cooling and MOT operation In both atomic systems the atomic beam is created by heating at $\sim 500\,^{\circ}\mathrm{C}$ a ytterbium nugget in an effusive oven kept inside a high vacuum enclosure ($\sim 10^{-7}\,\mathrm{mbar}$). The oven temperature is maintained constant using a feedback servo loop. Hot atoms travel along the vacuum chamber axis passing through a narrow channel which separates the oven high vacuum region to the experimental chamber ultra-high vacuum ($\sim 10^{-9}\,\mathrm{mbar}$). The vacuum is maintained by an ion pump and a getter pump, a vacuum gauge is also present to monitor the vacuum level. To avoid systematic effects caused by the atomic beam, a

mechanical shutter is installed on YbI which prevents the hot atoms to get into the main chamber during spectroscopy. The system is designed to slow down and trap atoms from the thermal beam without using a Zeeman slower. The oven is kept close to the experimental chamber to have a higher atomic flux, while a laser beam counterpropagates against the atomic beam exciting the strong ${}^1S_0 - {}^1P_1$ dipole transition at 399 nm. The frequency of the slower beam is detuned by ~ 120 MHz below resonance and is fine tuned to cool down only ^{171}Yb atoms. Typically 10 mW of slower radiation is used, however this value and the loading time can be modified to regulate the number of atoms collected. Usually $1-5 \times 10^6$ Yb atoms are present after cooling. In YbI the slower beam enters from a side of the vacuum chamber and it is reflected by an intra vacuum mirror, avoiding the direct sight of the oven output thus reducing the BBR shift related uncertainty. In YbII the slower enters from the opposite side of the oven through a sapphire window kept at a temperature of 300 °C to avoid Yb metallic deposition on the inner surface. The slowed atoms are then confined in a two-stage magneto optical trap[1] made by crossing three back-reflected laser beams, arranged in an orthogonal fashion. The first stage is at 399 nm, 15 MHz red-detuned, with 1 mW beams and and a magnetic field gradient of ~ 3 mT/cm generated by a pair of anti-Helmotz coils. It traps and cools the atoms down to the Doppler limit of 1 mK. The copper wires used to produce the MOT coils have hollow core for water cooling, the coils can carry up to 100 A. The loading time of the trap usually ranges from 30 ms up to 1 s depending on the experimental requirements.

The second MOT stage exploits the ${}^1S_0 - {}^3P_1$ intercombination transition at 556 nm in the green region of the spectrum, that cools further down the atoms at the µK level. During this phase the magnetic field gradient as well as the light intensity and the frequency detuning are regulated to optimize the transfer efficiency from the blue MOT, the temperature of the atoms and to optimize the loading in the optical lattice. The first of the three green MOT phases applies 300 µW of 556 nm light detuned by 2 MHz for ~ 17 ms with a magnetic field gradient of 1 mT/cm. After this the atomic cloud is compressed for 20 ms by doubling the magnetic field gradient while the frequency detuning is moved by 1 MHz towards the resonance, this ensures a better overlap with the optical lattice potential. The third, and last, green MOT stage features a laser power of $< 30\,\mu$W and a detuning of < 500 kHz with a duration up to 50 ms. These parameters are fine tuned to control the number of atoms, the final temperature is between 4 and 25 µK limited by Doppler cooling limit. A temperature of tens of µK it is sufficient to load the atomic cloud in the optical lattice.

[1]For a detailed description of the MOT functioning see chapter 2.

Optical lattice Both clocks implement 1-D optical lattice along the vertical direction to strongly suppress tunnelling of the atoms among trapping sites [100] operating at the magic wavelength (see chapter 2). The most significant difference between the two atomic systems is how the optical lattice potential is generated.

On YbI the collimated lattice laser light, coming from a fiber output coupler, is manipulated using a lens before crossing the vacuum chamber from the bottom side, generating a gaussian beam of 120 µm of waist. This is back reflected by a plane mirror placed on the top side of the chamber and mode matched to the incoming ray by a second lens. On YbI the optical power sent to the atoms can go up to 2 W corresponding to a trap depth of $\sim 400\,E_r$.

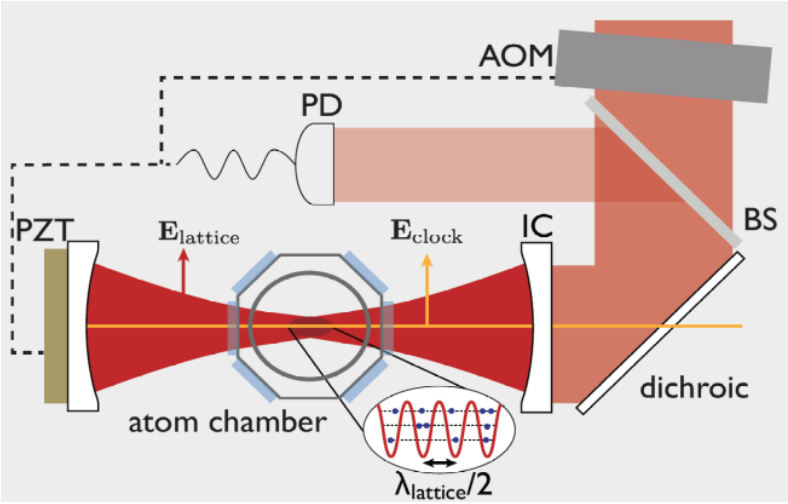

Figure 6.2: Scheme of the power enhancement cavity along with its power and length lock. The clock laser beam is also shown for completeness. Courtesy of NIST Yb clock group.

In YbII the lattice potential is generated inside a build-up cavity, which consists in a vertical, out of vacuum, Fabry-Perot resonator with a finesse of about 200. The cavity allows to accumulate power up to 100 times while keeping large beam waist of about 320 µm to maintain a low atomic density and to control the atomic collisions. The input power is ~ 200 mW resulting in a trap depth up to $2000\,E_r$. With such a deep lattice YbII is capable to routinely operate with more than 1 million trapped atoms. In order to avoid heating effects due to amplitude fluctuations, the input power is stabilized using the PDH technique with a fast feedback acting on the AOM and a slow correction applied on the mirror PZT (see fig. 6.2).

Laser generation The 399 nm laser is generated by a commercial Toptica diode laser at 798 nm featuring a SHG doubling stage, with a total output of 250 mW (see fig. 6.3). The laser light is splitted between YbI and YbII. YbI has a dedicated

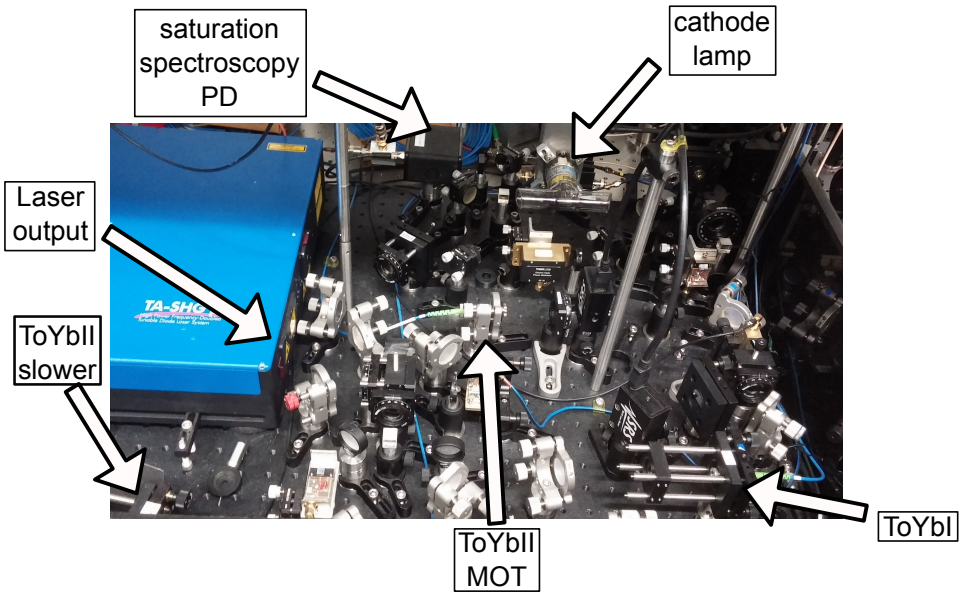

Figure 6.3: 399 nm laser output and YbII distribution bench. The hollow cathode lamp used to lock the frequency is also visible.

distribution bench made by miniaturized optics mounted on a separated optical bench covered by foam to reduce thermal effects on alignment thus ensuring a long operation without human intervention. The 399 nm laser frequency is locked on the ^{171}Yb frequency by absorption spectroscopy [116, 117] with a hollow cathode lamp filled with Yb and Ne (buffer gas) as atomic frequency reference [43]. The optical power for the three branches (slower, MOT beam and detection) is stabilized using separate feedback servo loops acting on AOMs.

The 556 nm light is provided by SHG of an 1112 nm Yb fiber laser using a frequency conversion wavegiude. The frequency is stabilized using a high-finesse ULE optical cavity, kept under vacuum and temperature stabilized to reduce the frequency drift. The lock operates both on the laser piezo (slow corrections) and an external AOM (fast corrections). Total output power of 15 mW and it is splitted between the two clocks.

The lattice laser source is a commercial Titanium Sapphire (Ti:S) with an output power of ~ 6 W, pumped with a 18 W, 532 nm laser. The frequency is stabilized using a reference optical cavity and applying the feedback on the laser's intra-cavity piezoelectric transducer. The light is sent to the two clocks both featuring an interference Bragg grating ($\Delta\lambda = 0.05$ nm) to filter the amplified spontaneous emission (ASE) close to the lattice wavelength, thus ensuring the best spectral purity. A special photonic crystal fiber [118], capable to handle high power beams, was installed to deliver the maximum optical power to YbI. On YbII, given the lower lattice power needed, a conventional PM fiber is used. Once the light comes out

from the fiber a PBS cube ensures clean linear polarization and a $\lambda/2$ waveplate, together with a $\lambda/4$ waveplate, compensate the birefringence induced by the vacuum viewports. The absolute lattice frequency is also measured using an optical frequency comb referenced to a hydrogen maser.

Clock laser It consists in a quantum dot, tapered amplified diode laser at 1156 nm with a linewidth of 30 kHz. The laser is frequency stabilized, by means of the PDH technique, with an ultra-stable, 29 cm long, ULE optical cavity exhibiting a finesse of 877 000 [21]. The laser linewidth reaches 100 mHz when locked to the cavity. The resonator is kept under vacuum ($\sim 10^{-8}$ mbar) together with three nested layers of polished aluminium which act as passive thermal radiation shields. The vacuum housing has an estimated thermal time constant of 4 days, suppressing short time thermal fluctuation by 7 orders of magnitude. In order to actively stabilize the temperature, on the outer surface of the vacuum enclosure are installed 6 in-loop and 6 out-of-loop thermistors with resistive heaters. The set point temperature corresponds to the zero CTE of the cavity at 35 °C.

The 1156 nm laser is then frequency doubled using a periodically polled lithium niobate (PPLN) wavegiude crystal in single pass, which gives a total output of 20 mW of 579 nm light. After being splitted and distributed, 5 mW are available for each clock for spectroscopy.

The instability of the local oscillator has been measured using the atoms as frequency discriminator.The resulting Allan-deviation is reported in fig.6.4. The fliker floor instability is $\sigma \leq 1.5 \times 10^{-16}$ in the averaging time interval 1-1000 s, this result represent an upper limit because it includes the detection noise as well. The cavity frequency drift has been evaluated by monitoring the atomic transition over the course of a year resulting in a constant drift of -35 mHz/s. It is actively compensated by a computer controlled automatic drift cancellation system.

The distribution optical bench along with the infra-red laser are mounted on an active anti-vibration platform providing further noise suppression in the region 5-100 Hz. Moreover this bench is placed inside an anti-acoustic chamber which ensures an additional shielding against acoustic vibrations. For each clock, a fiber switch, placed along the 578 nm fiber, selects the optical path of the clock laser light which can be either the two directions along the optical lattice. The two optical paths are designed in order to have a 'main' direction which is phase noise compensated and power stabilized, used for the actual clock laser light and a 'rear' direction where the full power 578 nm beam is used for the sideband cooling process. In YbI the main direction goes from the top to the bottom (the clock laser light enters from the lattice back reflector, see fig. 6.5) side, while for YbII is the opposite as reported in fig. 6.2.

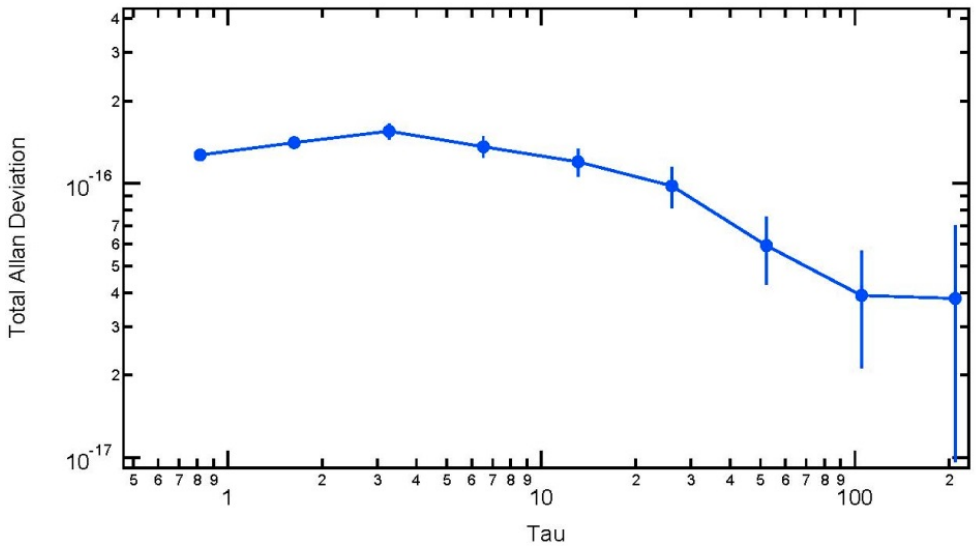

Figure 6.4: Fractional frequency instability of the free running clock laser locked on the locked on the ultra stable 29 cm long cavity. Courtesy of NIST yb clock group.

Phase noise compensation The clock laser light is sent to the two clocks through optical fibers. However, mechanical and vibrational stress introduces optical path variations in the fibers that result in additional phase noise of the local oscillator radiation. This noise is actively stabilized using the reflected light signal that goes back from the experimental table to the distribution optical bench, making a round trip and passing twice through the fiber. The beatnote between the incoming and the back reflected light is collected by a photodiode. The noise compensation corrections are applied by an AOM located on the distribution bench.

Special care was taken to minimize the residual Doppler effect caused by the relative motion of the atoms trapped in the lattice respect to the clock laser wave fronts. The reference point of the fiber noise cancellation system, that is the mirror surface that reflects the light back though the optical fiber, is the back side of the lattice retro-reflector. This mirror on one side is reflective at 759 nm while on the other side is partially reflective for 578 nm (see fig. 6.5). In this way the vibrations, that mechanically shake the mirrors, affect equally both the lattice standing wave and the clock laser.By actively cancelling the local oscillator phase noise the trapped atoms and the probing light are in the same reference frame [96]. The level of noise suppression is $\leq 2 \times 10^{-17}$ at 1 s, assessed using a Mach-Zender interferometer.

6.1.1 Sideband cooling

When atoms are strongly trapped in the optical lattice they are distributed among the vibrational levels of the trapping potential. Different populations of the

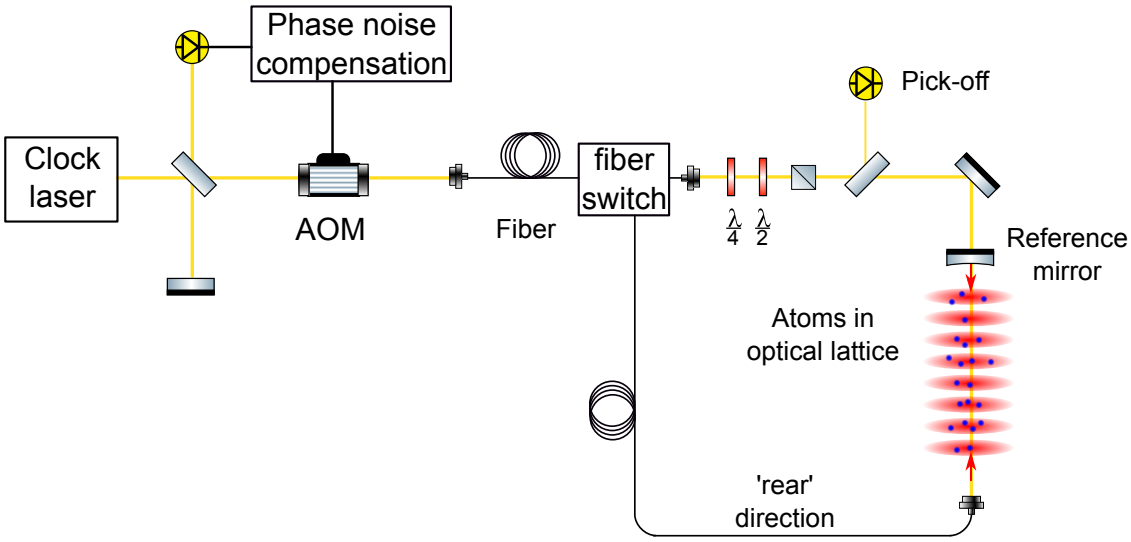

Figure 6.5: Scheme of the 578 nm clock laser optical path through the atoms in the lattice.

motional states results in different amplitude of the spectroscopic sidebands. We saw in sec. 5.1.6 the relation between the ratio of the blue and red sideband and the longitudinal temperature of the atoms trapped in a 1D lattice (eq. (5.4)). The sideband cooling technique allows to bring higher vibrational level atoms to the lowest one by means of a 578 nm red-detuned light pulse, resonant to the transition $|g, \boldsymbol{n}\rangle \rightarrow |e, \boldsymbol{n-1}\rangle$[2], along with the 1389 nm repumper light. The atoms cycles around the red detuned transition and the decay happens predominantly at the carrier frequency, thus the average outcome of this mechanism is the depletion of the higher motional state in favour of the lowest, like an optical pumping process. As a consequence, the red sideband of the spectrum is significantly suppressed as can be seen in fig. 6.6, resulting in a reduced atomic temperature in the longitudinal direction of few µK.

6.1.2 Clock sequence

The experimental sequence applied on the two clocks are quite similar and it is sketched in fig. 6.9. The cycle starts with the loading of the blue MOT at 399 nm for 80-100 ms, during this time the 556 nm lasers are already turned on. After loading the MOT the 399 nm light is switched off and the atomic cloud is directly transferred in the green MOT, then the three cooling steps are applied for ~ 20 ms each. When the 556 nm light is turned of, the atoms at a temperature of about

[2]where g and e denotes the internal atomic state while n the motional state.

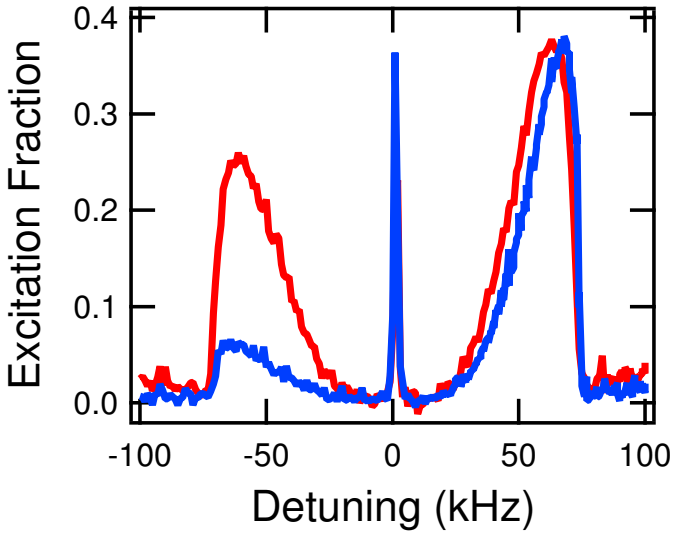

Figure 6.6: Sideband spectra of the trapped atoms with (blue) and without (red) sideband cooling at the same trap depth. A strongly suppressed red sideband is visible in the blue curve. From [44].

5-10 µK are loaded into the lattice potential. The lattice laser light remains on for the entire cycle. Once the lattice is loaded the atoms are further cooled down with 20 ms of sideband cooling and the desired Zeeman ground state level is selected by an optical pumping process with a 556 nm pulse 10 ms long (see sec. 2.3.3). After that the magnetic field is shut down, the system waits for 20 ms before spectroscopy to allow the magnetic field to stabilize. This is the end of the preparation stage, the typical number of trapped atoms ready to be interrogated is about 5000 for YbI and 10 000 for YbII.

The interrogation phase is different in the case of Rabi or Ramsey spectroscopy. For the former typically a 280 ms π pulse is applied, resulting in a Fourirer limited spectroscopy line of 3 Hz (see fig. 6.8). The pulse length can be optimized for the desired application between 140 ms and 1500 ms limited by the local oscillator coherence time. When Ramsey interrogation is applied the usual $\pi/2$ pulse duration is 25 ms separated by a free evolution time of 240 ms which gives fringes with a central feature of 1.9 Hz (see fig. 6.8). The typical contrast for both techinques is above 90 %. The clock laser light remains active during the free evolution time at a far detuned frequency, to ensure that phase noise compensation systems maintain phase continuity between the two pulses.

The detection phase exploits the atomic shelving techniques (see sec. 5.1.5 for details). The florescence from three 399 nm light pulses is recorded to evaluate the number of atoms at the ground state $|g\rangle$, the background and the exited state $|e\rangle$ atoms respectively (7 ms pulses separated by 6 ms). After the second detection

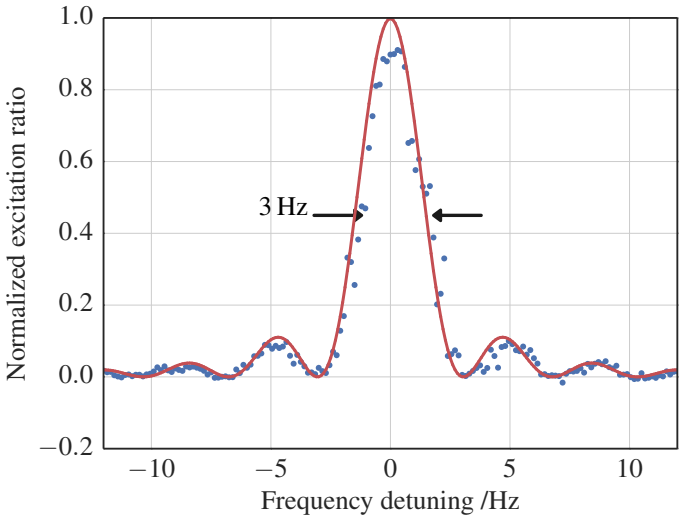

Figure 6.7: Typical Rabi spectroscopy with interrogation time $t = 240\,\text{ms}$

pulse, a 1389 nm repumper light pulse (4 ms) brings atoms from the metastable $^3P_0$ level to $^1D_1$ excited state and then they decay to the ground state where are detected by the last 399 nm pulse. The flourescence light, is recorded by PMT and it is proportional to the atomic population in the different states (P_g,P_e and P_b). The normalized atomic signal is computed as:

$$\psi \equiv \frac{|e\rangle}{|e\rangle + |g\rangle} \approx \frac{P_e - P_b}{P_e + P_g - 2P_b}. \tag{6.1}$$

The total cycle duration is about 530 ms, depending on the experimental requirements.

From [7].

$$\sigma_{\text{atom}} \simeq \frac{1}{\pi Q}\sqrt{\frac{T_c}{\tau}}\sqrt{\frac{1}{N} + \frac{1}{Nn_{\text{ph}}} + \frac{2\sigma_N^2}{N^2} + \gamma} \tag{6.2}$$

6.2 Uncertainty budget evaluation

The last complete uncertainty budget for YbI was completed in 2009 giving a fractional uncertainty of 3.4×10^{-16} [87]. Now a second clock is present (YbII) and the ultimate goal is to compare the frequency of the two clocks at a level of 10^{-18}. In order to achieve that, the systematic effects have to be controlled better than few parts in 10^{18}, which means that every effect that could be neglected in the past now has to be thoroughly characterized.

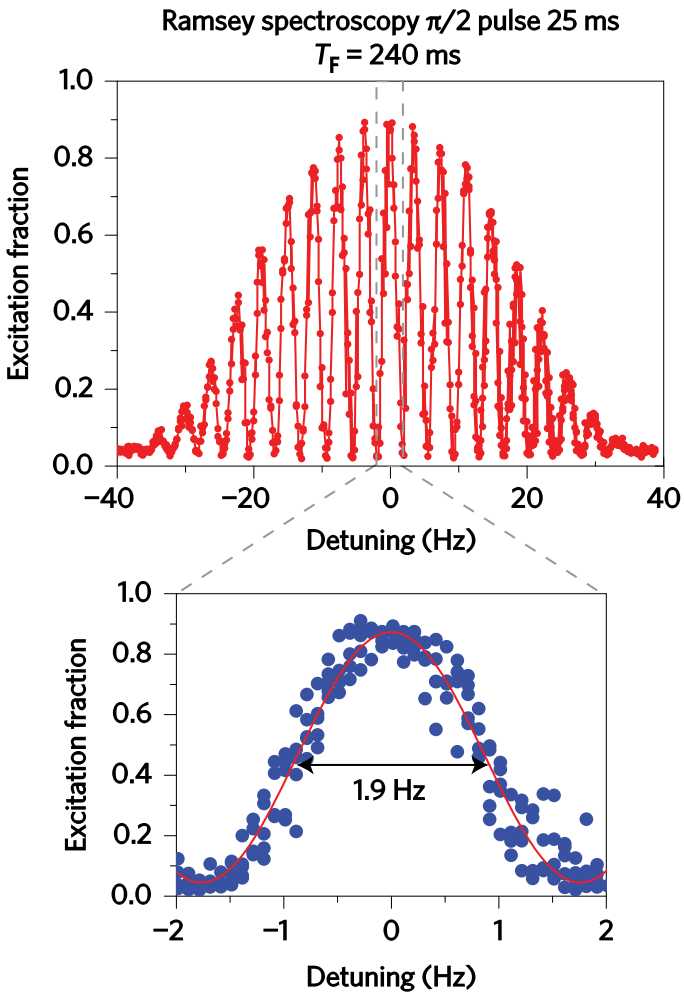

Figure 6.8: Typical Ramsey spectroscopy with free evolution time T_F of 240 ms. From [21]

During my visit I worked on the measurement of several systematic shifts measured using YbI, which I will give the details in this paragraph namely: cold collisions, lattice light, background gas collisions and residual Doppler. The work reported here on lattice light shift is part of a longer data taking period eventually resulted in a publication [44]. The final complete uncertainty budget is reported in Tab. 6.1.

6.2.1 Density shift

Trapping large ensembles of ultra-cold atoms in an optical lattice allows to increase the signal to noise ratio of the atomic state measure and it is one key feature of optical lattice clocks. However, cold collisions between the trapped atoms

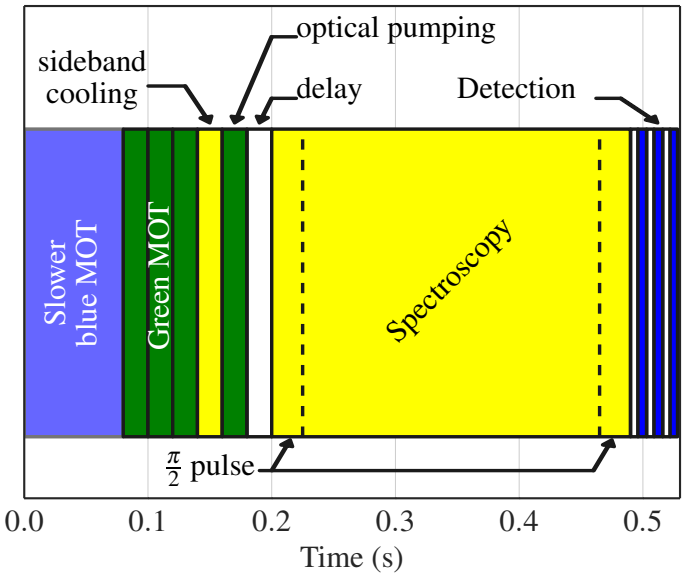

Figure 6.9: Diagram of the clock sequence. In case of Ramsey spectroscopy the $\pi/2$ pulses are represented with dashed lines. In Rabi spectroscopy the π pulse lasts the entire spectroscopy time.

Table 6.1: Complete uncertainty budget evaluation o the two clock at NIST. Presented at EFTF-IFCS 2017.

	Shift (10^{-18})	Unc. (10^{-18})
BBR Stark	-2358.3	1.0
Lattice	-1.4	0.8
Second-order Zeeman	-117.8	0.3
Cold collision	0.8	0.2
Background gas collision	-10.2	0.8
DC Stark	0.0	<0.1
Probe AC Stark	0.04	0.04
First-order Doppler	0.0	<0.1
Second-order Doppler	0.0	<0.1
Tunneling	0.0	<0.1
Servo error	0.0	<0.1
Line pulling	0.0	<0.1
AOM phase chirp	0.0	<0.1
Total	-2486.9	1.6

give rise to a density dependent perturbation of the transition.

To evaluate this shift we interleaved measurements with different number of atoms in the lattice for different lattice trap depth. To modulate the number of atoms we changed the slower beam intensity keeping the cycle duration constant. The obtained shift is divided by the population difference between the two interleaved clock states (Δ_{pop}) and it is plotted in figure 6.10. The first three points (at low trap depth) do not follow the linear trend of the shift. This can be explained by the p-wave barrier at $\approx 30\,\mu$K[50] which corresponds to a lattice trap depth of $\approx 300\,\mathrm{E_r}$. Atom ensembles trapped in such shallow traps do not have enough energy to overcome the centrifugal barrier, thus experience a lower shift. The magnitude of the shift is $-6.0(7) \times 10^{-23}\,(\Delta_{\mathrm{pop}}\mathrm{E_r})^{-1}$, where the first three points of the plot are excluded from the fit.

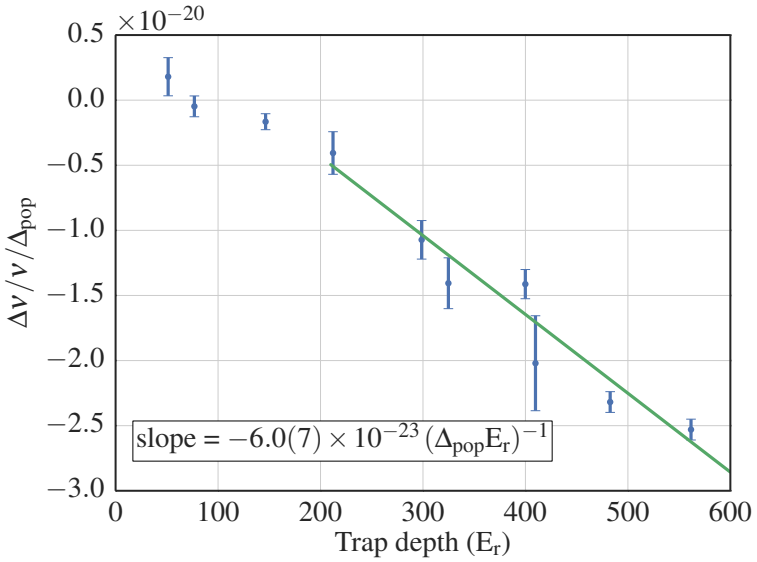

Figure 6.10: Density shift per atom unit versus the lattice trap depth.

Density shift evaluation changes dramatically when any parameter of the system is altered. At the time of these measurement the lattice beam on YbI was prepared to have a smaller beam waist, approximatively half of the typical value of 120 µm, to enhance lattice dependent effects. This set up was used for the lattice light shift evaluation as well as the background gas shift and the residual Doppler. As a consequence the shift evaluated here differs from what reported on Tab.6.1, which has been assessed afterwards with the larger lattice beam radius and at a trap depth of $50\,\mathrm{E_r}$. The desity shift evauation reported here has been used to correct and remove the effect when evaluating otther systematic effects like, for example, lattice light shift or the background gas shift. The result reported in this paragraph is implemented in the data analysis system, in order to subtract the density shift

to extract other effects of interest when the system runs with the aforementioned parameters.

6.2.2 Lattice Stark shift and operational magic wavelength

Electronic energy levels of the atoms are perturbed in presence of a light field (AC Stark effect). In optical lattice clocks atoms are trapped in a strong stationary light potential, made by a retro-reflected laser, called optical lattice. In this way a high number of atoms are trapped with a long lifetime in the trap, allowing long interaction time with the clock laser and, consequently, a high signal to noise ratio. This shift depends on the frequency and intensity of the lattice laser. The effect is cancelled, at first order, tuning the laser frequency to the so-called magic wavelength, for which the energy levels of the clock transition are perturbed by the same amount. However, when the accuracy of the clock goes beyond the 10^{-17} level, other smaller effects that prevent an exact cancellation of the perturbation must be considered [20, 46]. In particular, higher order couplings (magnetic dipole M1 and electric quadrupole E2) introduce shifts which scale non-linearly with the trap depth as well as Hyperpolarizability, which arises from two photon absorption by a quantum absorber and depends quadratically on the lattice intensity. Additionally, recent theoretical works suggest that these higher order perturbations depend on the lattice motional levels occupied by the atoms which, in turn, depends on the atomic sample temperature [119, 48], making more difficult the experimental characterization.

Considering a 1-D optical lattice, with confinement both longitudinal and transverse, the resulting lattice light shift for an atom in the longitudinal lattice band n_z and transverse motional state $n_\rho = n_x + n_y$ is [44]:

$$\begin{aligned}\frac{\delta\nu_{\text{clock}}}{\nu_{\text{clock}}} =& n_5\Delta\alpha'_{\text{M1E2}} + [(n_1+n_2)\Delta\alpha'_{\text{E1}} - n_1\Delta\alpha'_{\text{M1E2}}]U^{\frac{1}{2}} \\ &- [\Delta\alpha'_{\text{E1}} + (n_3+n_4+4n_5)\Delta\beta']U \\ &+ [2\Delta\beta'(n_1+n_2)]U^{\frac{3}{2}} - \Delta\beta' U^2\end{aligned} \tag{6.3}$$

where Δ indicates a difference in a quantity between clock states and U is the dimensionless ratio between the lattice trap depth to recoil energy E_r. The other terms appearing in (6.3) are: the differential dipole polarizability $\Delta\alpha'_{\text{E1}} = \Delta\alpha_{\text{E1}}E_r/\alpha_{\text{E1}}(\nu_{\text{magic}})h\nu_{\text{clock}}$, higher multipolarizabilities $\Delta\alpha'_{\text{M1E2}} = \Delta\alpha_{\text{M1E2}}E_r/\alpha_{\text{E1}}(\nu_{\text{magic}})h\nu_{\text{clock}}$ and hyperpolarizability $\Delta\beta' = \Delta\beta E_r^2/\alpha_{\text{E1}}(\nu_{\text{magic}})^2 h\nu_{\text{clock}}$. The transverse and longitudinal quantum numbers are: $n_1 = (n_z + 1/2)$, $n_2 = \frac{\sqrt{2}}{k\omega_0}(n_\rho + 1)$, $n_3 = \frac{3}{2}(n_z^2 + n_z + 1/2)$, $n_4 = \frac{8}{3k^2\omega_0^2}(n_\rho^2 + 2n_\rho + 3/2)$ and $n_5 = \frac{1}{\sqrt{2}k\omega_0}(n_z + 1/2)(n_\rho + 1)$ with $k = \frac{2\pi\nu_l}{c}$ for lattice frequency ν_l. The magic frequency ν_{magic} is defined as the lattice frequency such that $\Delta\alpha_{\text{E1}} = 0$.

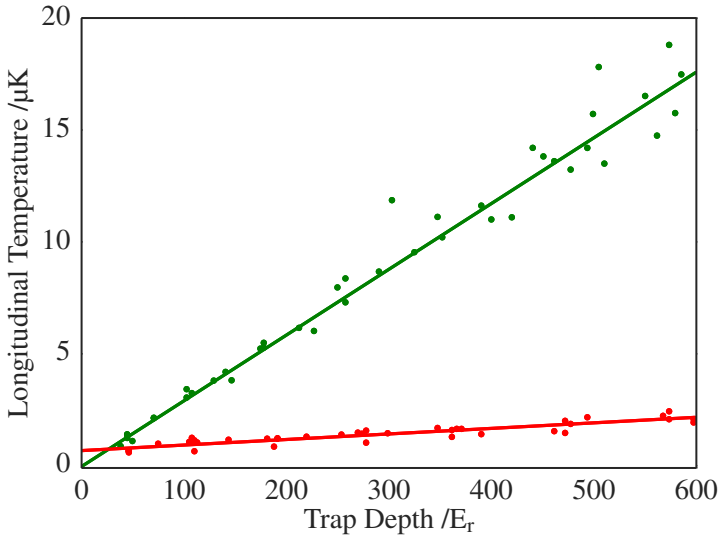

Figure 6.11: Longitudinal temperatures, extracted from sideband spectra, as a function of trap depth. The red trace corresponds to sideband cooling operative, while the green trace is without.

The lattice depth, as well as the atomic temperature, is determined via motional sideband spectroscopy (see fig. 6.6) for all the clock shift measurements. The lattice light frequency, locked to an external reference cavity, was daily measured using an ocatave-spanning Ti:sapphire optical frequency comb referenced to a calibrated hydrogen maser. The experimental measure of the atomic temperature with respect to the trap depth is reported in fig. 6.11, It shows a linear trend of the temperature with trap depth and also a smaller slope for sideband cooled samples compared to non cooled ones. We attribute this scaling to the combined effect of the lattice light shift on the $^1S_0 \rightarrow {}^3P_1$ cooling transition and the trapping energy limit of the finite lattice depth. This linear scaling brigs a substantial simplification in eq. (6.3): n_z and n_ρ gain an additional $\sqrt{U}$ dependency which gives $\langle n_1\rangle$,$\langle n_2\rangle \propto \sqrt{U}$ and $\langle n_3\rangle$,$\langle n_4\rangle$,$\langle n_5\rangle \propto U$. Accordingly eq.(6.3) can be expressed as:

$$\frac{\delta\nu_{\text{clock}}}{\nu_{clock}} = -\alpha^*(\nu_l)U - \beta^* U^2 \tag{6.4}$$

where α^* and β^* are the finite-temperature polarizability and hyperpolarizability respectively.

We measured the perturbation changing both frequency and intensity of the lattice laser on YbI and comparing the frequency with YbII, used as reference. Moreover, in order to investigate the impact of the atomic temperature on the shift, the entire measurement was performed two times with and without the sideband cooling process. The obtained data are reported in fig. 6.13a when sideband

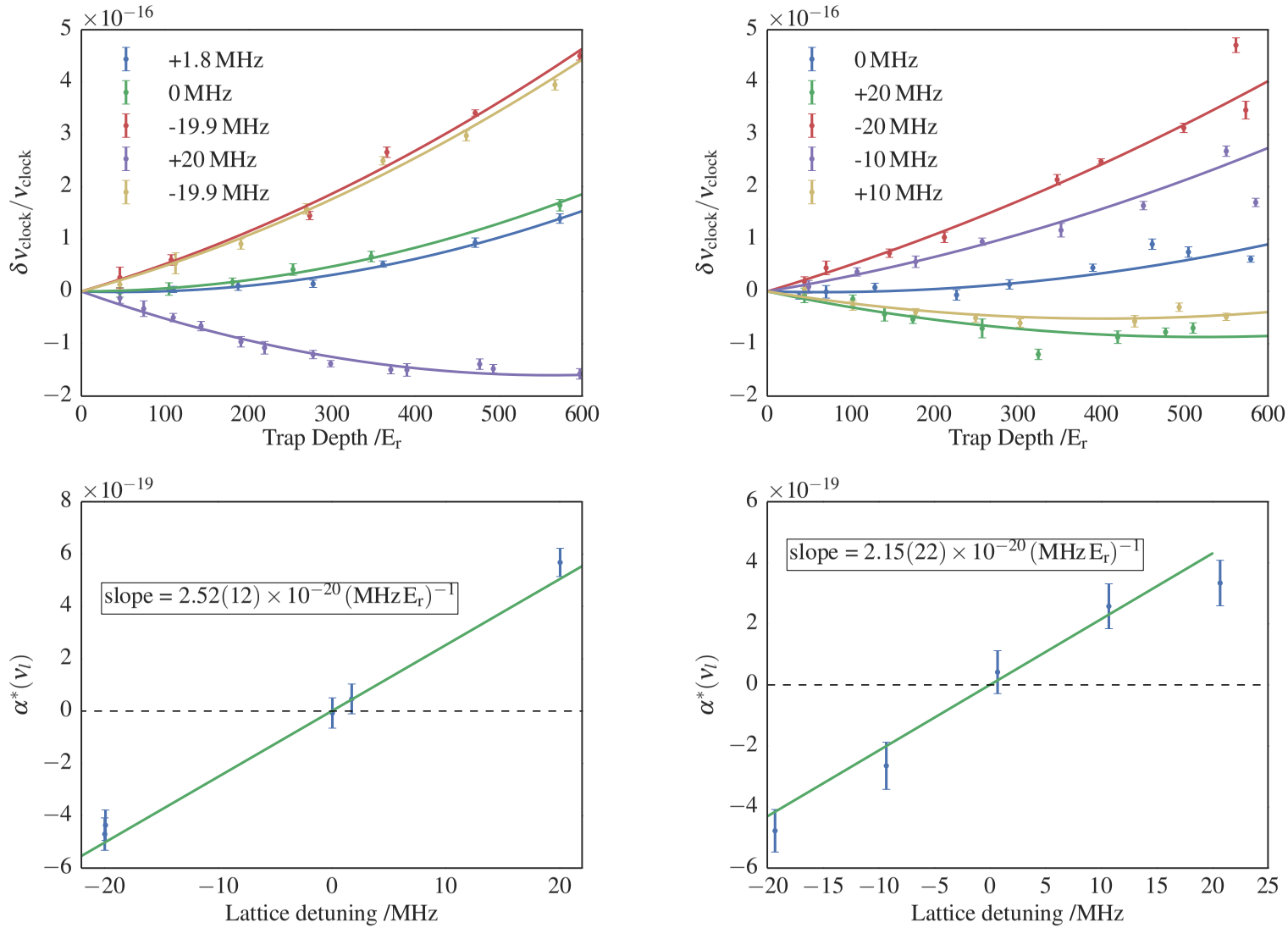

(a) Sideband cooling ON

(b) Sideband cooling OFF

Figure 6.13: Lattice lattice light shift evaluation on YbI with and without sideband cooling, using YbII as reference: shift in function of lattice trap depth at different lattice frequency (with global quadratic fit) and linear coefficient in function of lattice light frequency.

cooling is applied and in fig. 6.13b when it is not. The raw data were corrected for the density shift ($< 4 \times 10^{-18}$) while the error bars represent the total Allan deviation obtained at the end of each run. A global quadratic fit of the data is performed by fixing β^* for every frequency detuning (hyperpolarizability has negligible dependency on the lattice frequency close to magic frequency). The obtained linear coefficients α^* are reported in fig. 6.13a and 6.13b for the two cases. The parameters collected from the fit are gathered in Tab. 6.2. A direct comparison of the shift at fixed lattice frequency, when the additional cooling process is applied, is reported in fig.6.12.

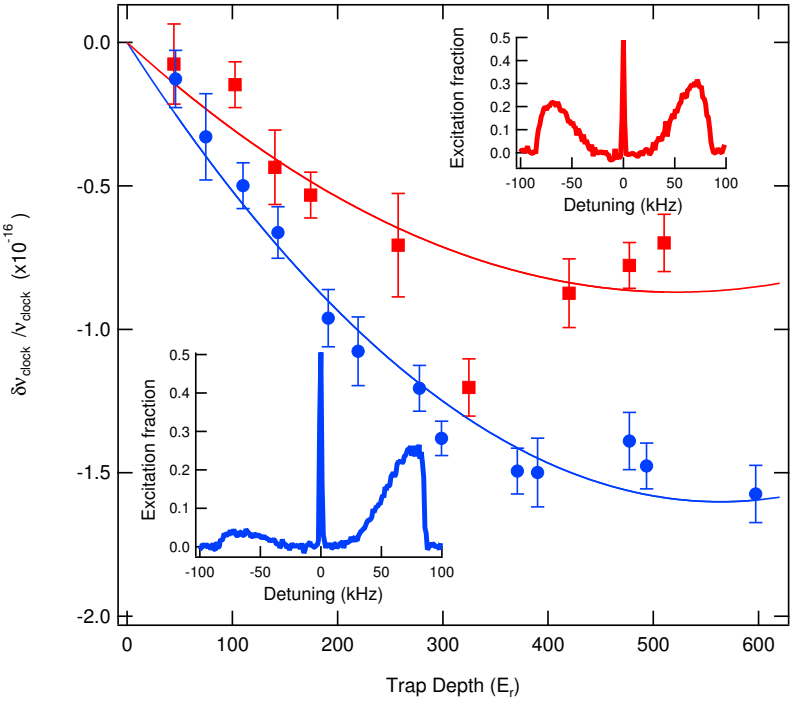

Figure 6.12: Comparison of lattice light shift with (blue trace) and without (red trace) the sideband cooling application for 20 MHz detuning from ν_{magic}. Since the cooler atoms are more localized in the high-intensity portion of the lattice, they experience a larger shift originating from the hyperpolarizability. The inset shows representative sideband traces. Courtesy of NIST Yb clock group.

It can be directly seen that sideband cooling affects only the longitudinal temperature T_l without changing the transverse T_t quantity. Another significative result is the dependency of the parameters to the average temperature of the atomic sample. As a consequence, colder atomic samples resulting from the sideband cooling process exhibits larger shift. This because almost the entire atomic population

[3]Data taken during 2015

Table 6.2: Summary of the data obtained from the fit of the lattice light shift data in different condition.

	YbII[3]	YbI (no s-band)	YbI (s-band)
T_l-T_t ($\mu K/1000\,\mathrm{E_r}$)	28	29 - 56	2.4 - 55
ν_{zero} (394 798XXXMHz)	270.7(9)	271.7(16)	269.3(9)
$\partial\alpha^*/\partial\nu_l$ (MHz^{-1})	$1.84(5)\times10^{-20}$	$2.15(22)\times10^{-20}$	$2.52(12)\times10^{-20}$
β^*	$3.6(2)\times10^{-22}$	$3.2(11)\times10^{-22}$	$5.0(7)\times10^{-22}$

lies in the lowest lattice motional state which experiences the highest lattice laser intensity.

By performing a linear fit of $\alpha^*(\nu_l)$ (fig. 6.13b) we can extract the lattice frequency which nulls the linear shift (ν_{zero}). This quantity correspond to the theoretical ν_{magic} shifted by the effect of multipolar contributions, the correction is small compared to the other terms ($\approx 400\,\mathrm{kHz}$) and is calculated theoretically [44]. Stronger shift with colder atoms can be appreciated in the different magnitude of the linear fit, however the evaluation of the magic frequency is consistent in each case. As far the hyperpolarizability is concerned a significative difference of about 36 % between the two cases further underlines the importance of a careful evaluation of the temperature of the atomic sample.

Operational magic wavelength When non linear shifts are taken into account, a new operational regime can be defined, the so called *operational magic wavelength* [119, 44], where the hyperpolarizability shift is compensated by the linear polarizability term by frequency detuning the lattice laser from the usual ν_{magic}. This gives the experimental advantage of a linear shift insensitive to the trap depth fluctuations at first order.

From the fit obtained we can define the operational magic wavelength as [44]:

$$\nu_{\mathrm{opmagic}} \equiv \frac{(-2\beta^* U)}{\partial\alpha^*/\partial\nu_l} + \nu_{\mathrm{zero}}. \tag{6.5}$$

Resolving this equation at a trap depth of $50\,\mathrm{E_r}$, which is sufficient for a 10^{-18} uncertainty operation of the clock, and using the value obtained in the previous paragraph gives a shift of $2.0(3)\,\mathrm{MHz}$ above ν_{zero}. At this regime, a variation of 10 % in trap depth introduces a variation in $\delta\nu_{\mathrm{clock}}/\nu_{\mathrm{clock}}$ of less than 1×10^{-19}.

6.2.3 Background gas collisions

The atomic manipulation, necessary for the clock to function, takes place into an ultra-high vacuum chamber, at typical pressure of few nTorr (∼130 nPa). Atoms

held in the optical lattice, however, can interact with particles of the residual gas (basically H_2 molecules) or the hot Yb atoms coming from the effusion oven. To avoid the effects due to the atomic beam, a mechanical shutter is present on YbI which prevents the hot atoms to get into the main vacuum chamber during spectroscopy. The typical lifetime of the trapped atoms is among 1-2 s.

These collisions are quite challenging to characterize since the size of the shift is small and there is not a straightforward way to change the vacuum pressure to magnify the effect. Moreover, theoretical models necessitate experimental corroboration in the case of Yb atoms, in this sense this measurement could help to improve the understanding of the underlying process.

We separately measured the shift coming from the background gas and from the atomic beam.

Background gas collisions $\mathrm{Yb}-\mathrm{H_2}$ Vacuum pressure was increased by heating the getter pump present in the system, which releases mainly H_2. This can be done by running a current through the pump. The getter emission was also preliminary measured using a residual gas analyzer. Figure 6.14 shows the relationship between the averaged pressure, measured using a vacuum gauge, and the $1/e$ lifetime of the atoms trapped in the lattice τ obtained at difference trap depth. It can be noticed a linear dependency of the pressure in function of the loss rate (the inverse of the lifetime τ^{-1}), not affected by the trap depth and with a slope of $2.87(5)\,\mathrm{n}\tau^{-1}$.

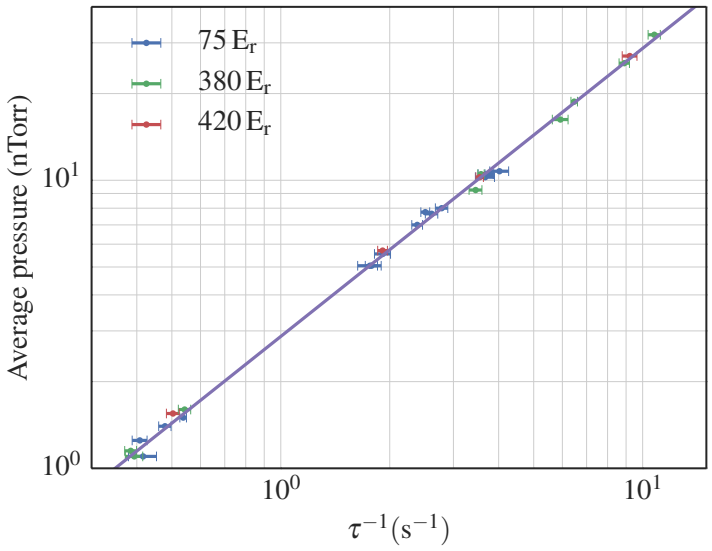

Figure 6.14: Pressure measured using the vacuum gauge in function of the lattice loss rate.

We took the frequency shift at different pressures and for different lattice trap depth ($75\,E_r$ and $400\,E_r$ respectively) keeping the atomic shutter closed during

spectroscopy. YbII has been used as frequency reference. The result is reported in figure 6.15. The error bars correspond to the Allan deviation of the measured frequency difference between the two clocks. The slopes obtained at the two different trap depths are consistent within 1σ. When the two data sets are combined, the resulting shift is $(\Delta\nu/\nu_0)_{\mathrm{Yb-H_2}} = 1.64(12) \times 10^{-17}\,\tau^{-1}$.

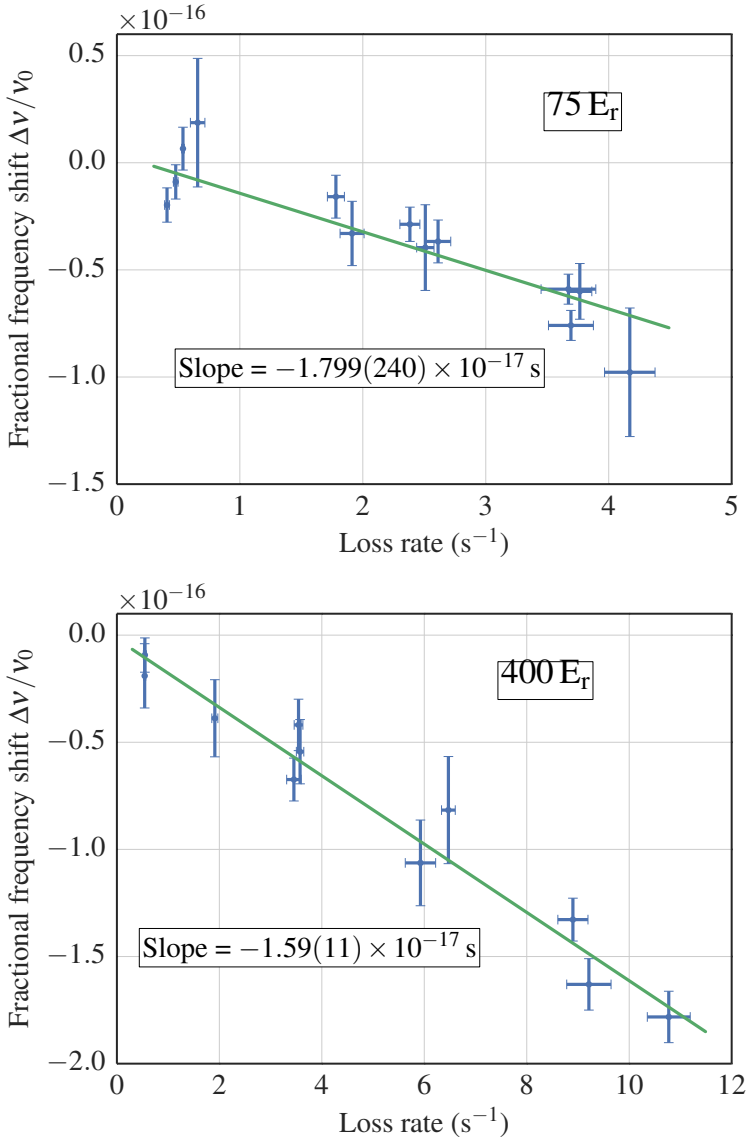

Figure 6.15: Frequency difference measurements between YbI and YbII while changing the vacuum pressure in the former, at 75 E_r and 400 E_r trap depth.

The line broadening caused by the background gas was investigated as well. Figure 6.17 shows the clock transition spectrum taken with 500 ms Rabi interrogations at different vacuum pressure. No significant broadening can be observed at

pressures below 20 nTorr (2.7 µPa).

The final shift present under normal operation, with a typical lifetime of 1.6 s corresponding to a loss rate of 0.625 s^{-1} and a pressure of 1.79 nTorr (239 nPa), is $\frac{\Delta\nu}{\nu} = -10.8(8) \times 10^{-18}$.

Atomic beam collisions Yb − Yb We interleaved measures with the atomic shutter open and closed during spectroscopy time, at different oven temperatures and lattice trap depth. Varying the oven temperature results in a different partial pressure of Yb in the experimental chamber.

The result of the interleaved measure is reported in figure 6.16, a significant trap depth dependence between 100 E_r and 570 E_r cannot be inferred. However, only one point was collected at 570 E_r and the error bars are still large as well, thus a strong conclusion cannot be made. In order to address only the effect of the atomic beam collisions, during the analysis the background gas shift has been removed for each datapoint. The shift is evaluated as $\left(\frac{\Delta\nu}{\nu_0}\right)_{\mathrm{Yb-Yb}} = 9.2(2) \times 10^{-18}$ s.

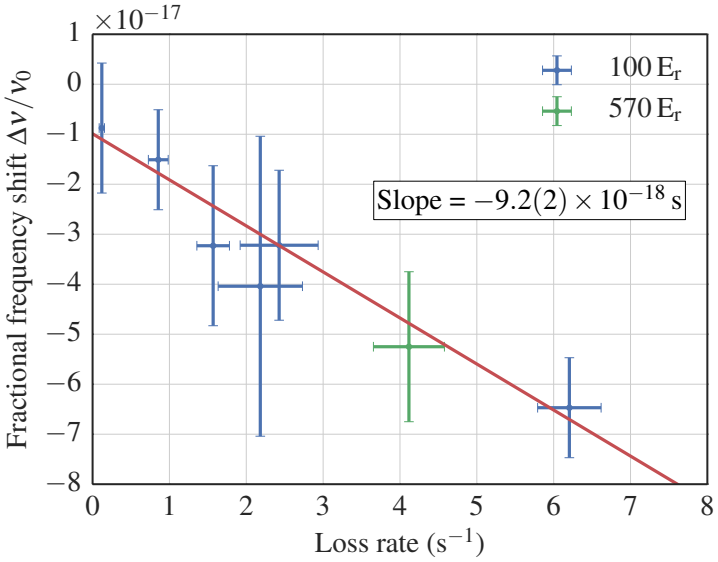

Figure 6.16: Frequency shift measure made by interleaving YbI with the shutter open and closed, at different lattice trap depth.

It has to be noted though that this shift is not present on YbI during normal operation because of the presence of the atomic shutter. An additional atomic shutter is foreseen to be installed on YbII as well.

Comparison to theory The most advanced model describing the interaction between background gas particles with trapped atoms is reported in [98]. It basically takes into account the weak, long-range interactions which does not eject

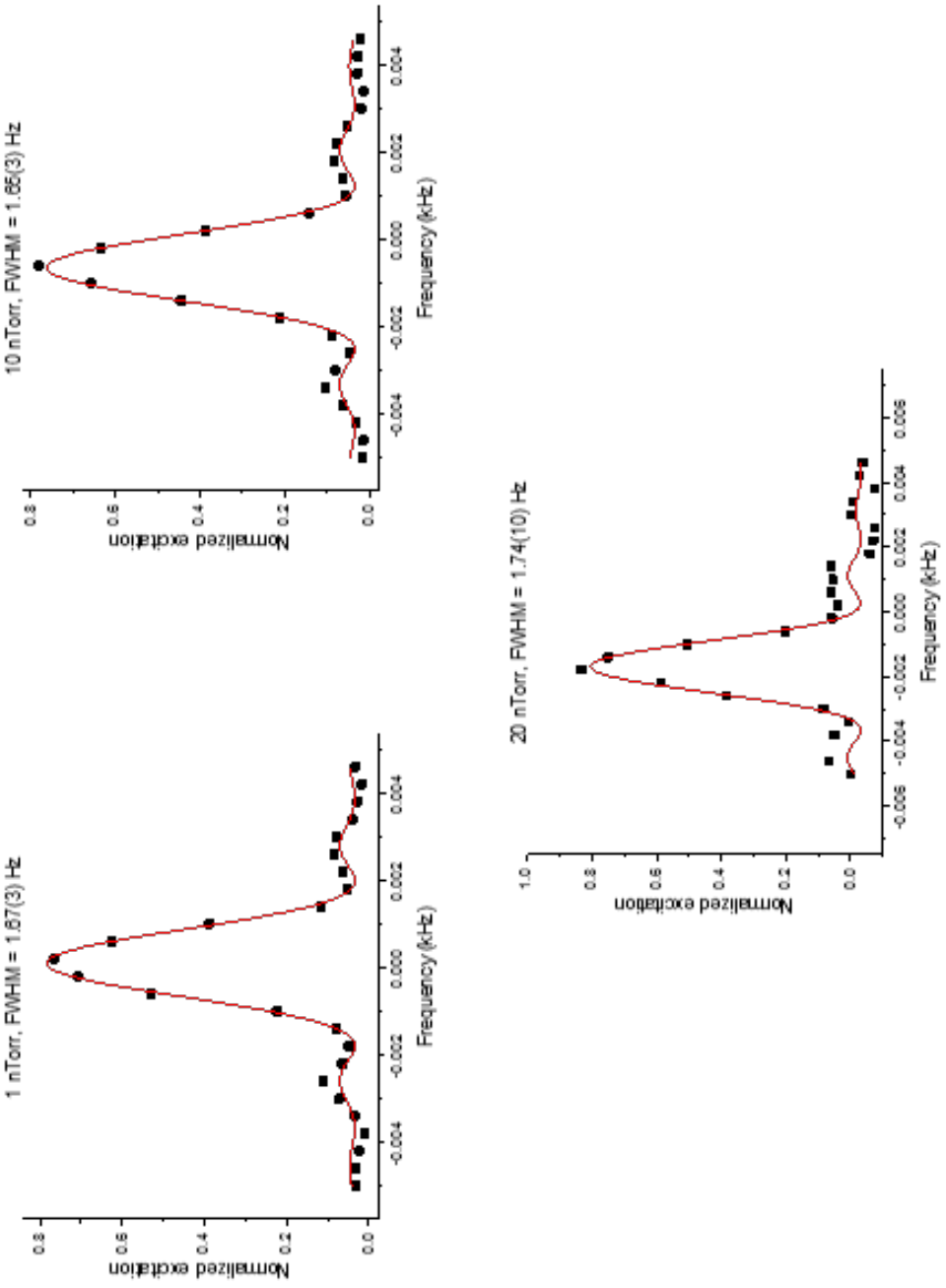

Figure 6.17: Rabi spectrum of the clock transition for 500 ms interrogation at different vacuum pressure. The shift is caused by the cavity drift. No significant line broadening can be noticed below 20 nTorr(2.7 µPa). Courtesy of NIST Yb clock group.

the atoms form the lattice but affects their energy levels instead. The equation describing the shift in function of the loss rate from the trap $(1/\tau)$ is:

$$\Delta\nu = \frac{1}{13.8\pi}\frac{\Delta C_6^{\mathrm{Yb-X}}}{C_6^{\mathrm{Yb-X}}}\frac{1}{\tau} \tag{6.6}$$

where C_6 is the long-range interatomic van der Waals coefficient between ground state Yb and particle X and $\Delta C_6^{\mathrm{Yb-X}}$ is the differential coefficient between ground and excited Yb and particle X. Calculation of these coefficients for Yb can be found in [120]. However, in the case of $\mathrm{Yb} - \mathrm{H_2}$ no a priori coefficients calculations are available so far, thus we considered[4] $C_6^{\mathrm{Yb-H_2}} \approx \sqrt{C_6^{\mathrm{Yb-Yb}} C_6^{\mathrm{H_2-H_2}}}$.

Given eq.(6.6), the focus is on the factor $\frac{\Delta C_6}{C_6}$. As a consequence of that the actual C_6 coefficient of hydrogen cancels between the numerator and the denominator. Using the Yb coefficients from [99] $C_6^g = 1929(39)$ and $C_6^e = 2561(95)$, the resulting equation is:

$$\left(\frac{\Delta\nu}{\nu}\right)_{\mathrm{teo}} = -(1.46(25)\times 10^{-17})\frac{1}{\tau}. \tag{6.7}$$

This is consistent with the experimental result of the background gas scattering of $\left(\frac{\Delta\nu}{\nu}\right)_{\mathrm{Yb-H_2}} = -(1.64(12)\times 10^{-17})\frac{1}{\tau}$. In the case of scattering from the atomic beam, $\left(\frac{\Delta\nu}{\nu_0}\right)_{\mathrm{Yb-Yb}} = -(9.2(2)\times 10^{-18})\frac{1}{\tau}$, the accordance is slightly less than 1σ.

6.2.4 Residual Doppler

Atoms tightly confined in an optical lattice are free of any recoil effect during spectroscopy. Despite that, relative vibrations among the lattice laser and the clock laser can give rise to a residual Doppler shift. To have an idea of this effect we took interleaved measures varying the delay time of the spectroscopy interval after the atoms are loaded in the lattice having the fiber noise cancellation system referenced to a mirror placed at the exit of the fiber. The result is in figure 6.18, we observed a relative shifts up to 5×10^{-16}. To minimize this effect, the fiber noise cancellation system is referenced to the lattice reference frame.

In order to assess the residual Doppler shift a large path length variation is induced by sweeping the clock laser light phase before it gets into the experimental chamber. This can be accomplished by using an EOM before the lattice back reflector (see fig. 6.18). The applied phase modulation was a linear ramp during spectroscopy which caused a shift of about 29 Hz (see fig. 6.19) in the case of fiber noise cancellation system not engaged. We measured the frequency difference by interleaving the clock with a positive and negative phase ramp, with and without

[4] Approximation consistent within $\approx 10\,\%$, K. Gibble private communication (2017)

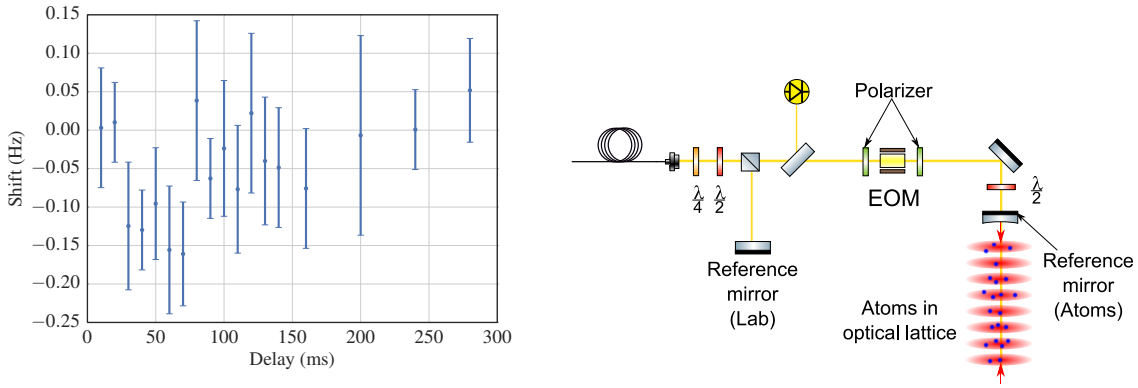

Figure 6.18: Left: Residual Doppler shift at different delay of the spectroscopy period. Right: Modified path of the yellow laser with the additional EOM together with polarizes. The fiber noise cancellation reference mirror labelled Lab is placed close to the optical fiber output while in the case of the mirror labelled Atom it is the outer face of the lattice back-reflector.

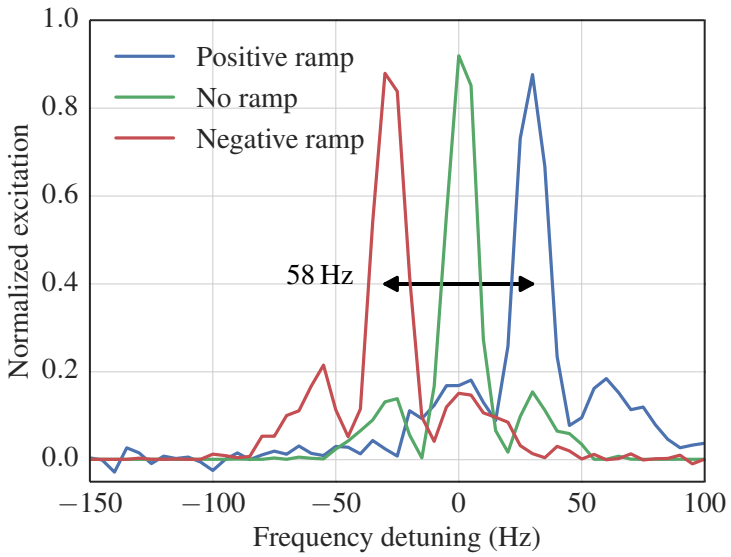

Figure 6.19: Effect of the induced variation of the optical path applied by the EOM using a positive or negative phase ramp.

the fiber noise compensation system. The suppression of the Doppler shift by the compensation system was $> 99.98\,\%$. Considering the residual Doppler shift we experienced, this suppression factor leads to a fractional frequency uncertainty of $<0.1 \times 10^{-18}$.

6.3 Zero Dead Time Clock - Stability measure

In chapter 2.6.1 a basic treatment of the Dick effect has been presented. Starting from eq. (2.44), different approaches can be followed in order to control the aliasing process: reducing the laser frequency noise S_ν or working on the sensitivity function $g(t)$. The former is addressed by improving the local oscillator performances, thus extending its coherence, allowing longer interrogation time and lower laser instability. Recent advances followed this idea [121] but, as can be seen in fig. 6.20 (red and blue traces), the effect still remains higher than the QPN and continues to limit the clock instability. Besides, in order to achieve always better performances, clock laser systems in some cases are even more complex than the atomic part, limiting their application outside the laboratory.

On the other hand, a careful optimization of the interrogation sequence can eliminate the dead time and consequently the aliasing effect nearly vanishes. To

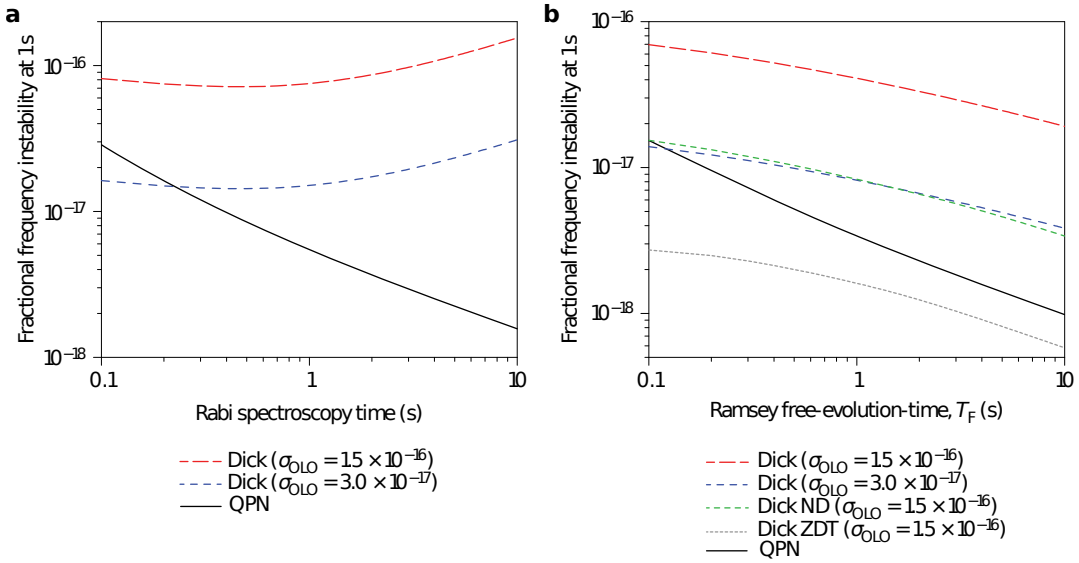

Figure 6.20: Dick effect instability contribution at 1 s vs the Rabi spectroscopy time (calculated using eq. (2.44))(a) and the Ramsey free evolution time (calculated using eq. (2.48)) (b) assuming a number of atoms of 10 000. The dead time is fixed at 240 ms. Several traces are displayed: dashed red is for the measured cavity stability, in dashed blue is for an hypothetical improved cavity, black is the QPN limit. In the Ramsey case the aliasing effect is also calculated for a non destructive (ND) detection scheme in dashed green and for the ZDT clock for a fixed duty cycle of 50 % in dashed grey. From [21].

eliminate the dead time we exploited a combination of two atomic systems and a shared local oscillator: the atoms of one system are interrogated while the other sample is prepared in the second one. Interleaving the interrogation between the

two atomic clouds, the clock laser is then always referred to the atoms, e.g. no dead time, and thus the Dick effect vanishes. We call this technique the Zero-Dead-Time clock (ZDT).

The experimental apparatus is described in chapter 6.1. It comprises two atomic systems, namely the atomic clocks YbI and YbII in the normal configuration and a single clock laser provides the light for both systems.Each clock is operated following the sequence presented in section 6.1.2, in particular typical operating parameters are: cycle time $T_c = 530\,\text{ms}$, quality line factor $Q \approx 2.7 \times 10^{14}$, number of atoms $N \approx 5000 - 10\,000$ and photons collected per atom $n >> 1$ yielding to a potential clock instability of $1 \times 10^{-17}/\sqrt{\tau}$ (from eq.(6.2)), limited only by the QPN. However, the clock stability is degraded by different effects like the technical fluctuations of the detected atoms, the phase noise coming from length fluctuations of the optical path travelled by the clock laser light reaching the atoms as well as the Dick effect. Technical detection noise is evaluated to be $\delta_{\text{det}} \approx 3\,\%$, giving in an instability of $\sigma_{\text{technical}} = 3 \times 10^{-17}/\sqrt{\tau}$, phase noise is actively compensated at a level of $\sigma_{\text{phase}} = 2 \times 10^{-17}/\sqrt{\tau}$, measured using a Mach–Zehnder interferometer. The Dick instability for one system is computed using eq. (2.48) with $T_d = 240\,\text{ms}$, $t_p = 25\,\text{ms}$ and it is plotted versus interrogation time (or free evolution time) in fig. 6.20 for different cases. As mentioned previously, it can be clearly seen that for longer spectroscopy time the Ramsey technique gives a lower Dick contribution than the Rabi one. It is worth to remember that the longest interrogation times reported in fig. 6.20 demands a clock laser stability not yet achieved by the current generation of oscillators but it can be reached using the technique described in section 6.3.4. The resulting value for a Ramsey free evolution time $T = 240\,\text{ms}$ is $\sigma_{\text{Dick}} = 7 \times 10^{-17}/\sqrt{\tau}$.

When the system is operated as ZDT clock a second system with similar performance is required to directly measure the frequency instability. However, since this additional clock is not available, the frequency instability has been assessed using a different approach namely a synchronized interrogations of the two atomic systems which can cancel out the Dick noise contribution [122]. Thus, to characterize the ZDT clock performance we made three different type of measurements: anti-synchronous, synchronous and the actual ZDT clock. The former allow us to enhance the Dick effect and compute the single clock instability while the synchronous suppresses it. When the clock run as ZDT only the frequency corrections can be measured.

The instability budget for a single clock is reported in tab 6.3 for the three different measures.

6.3.1 Anti-synchronous interrogation

In this case the two systems operate as independent clocks, synchronized in such a way that the clock laser alternately interrogates the two atomic clouds without

Table 6.3: Instability budget of the different operational configurations. All values are in units of $10^{-17}/\sqrt{\tau}$. From [21].

	Anti-synch.	Synch.	ZDT
σ_{QPN}	1	1	$1/\sqrt{2}$
$\sigma_{\text{technical}}$	3	3	$3/\sqrt{2}$
σ_{phase}	2	2	2
σ_{Dick}	$7\sqrt{2}$	common-mode rejected	<0.3
Estimated σ_{Total}	11	4	3
Experimental σ_{Total}	14	8	6

overlaps (see fig.6.21). In particular, the first $\pi/2$ pulse on YBI corresponds to the second pulse on YBII, while the frequency corrections applied to lock the clock laser are independent $\Big(f_1(t) \neq f_2(t)\Big)$.

This interrogation scheme gives the highest sensitivity to the Dick effect because the frequency difference between the two clocks retains the laser noise contribution from both systems.

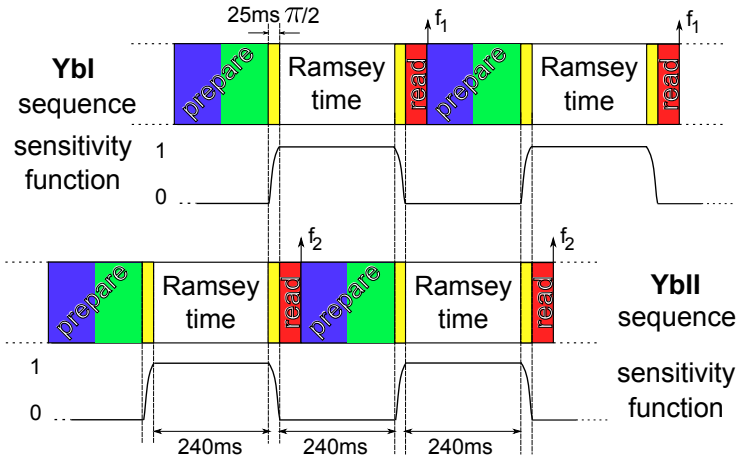

Figure 6.21: Anti-synchronous interrogation sequence with the sensitivity functions of the two clocks.

We computed the fractional frequency instability using the frequency difference $\Big(\Delta f(t) = f_1(t) - f_2(t)\Big)$ between the two clocks and then dividing it by $\sqrt{2}$ in order to assess the single clock estimate. This is applicable only for noise processes uncorrelated between the two systems. Nevertheless, the aliasing noise in the anti-synchronous case is correlated between the two systems, thus requiring a linear sum. This detail introduces subtle complication in the evaluation of the single clock instability contribution in a measure. In order to conservatively take into account the correlation of the Dick effect in the anti-synchronized case, the value obtained

from eq. (2.48) is multiplied by $\sqrt{2}$ (see Tab 6.3). The computed Allan deviation of $\Delta f(t)$ results in a combined instability of the two clocks of $2.0 \times 10^{-16}/\sqrt{\tau}$, which gives a single clock instability of $\sigma_{\mathrm{Tot}} = 1.4 \times 10^{-16}/\sqrt{\tau}$ (see fig. 6.22) and it represents an upper limit.

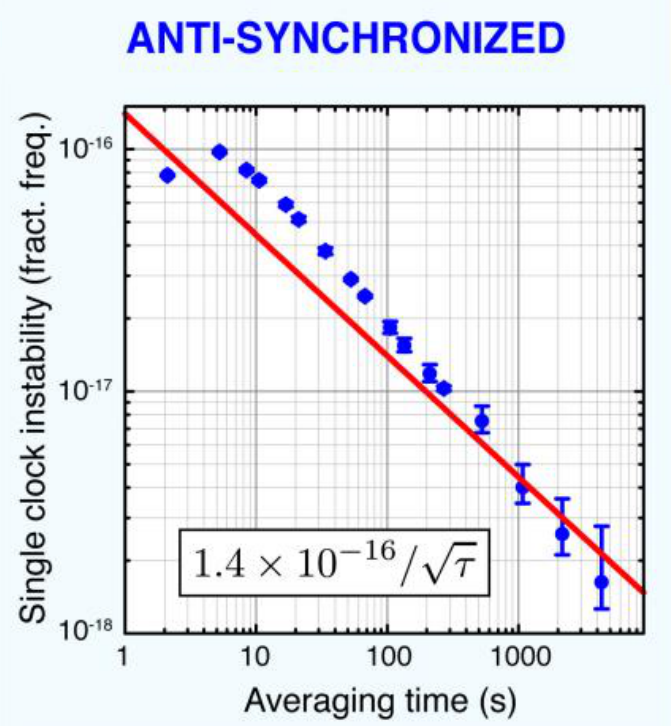

Figure 6.22: Single clock fractional frequency instability in the anti-synchronous interrogation

6.3.2 ZDT clock operation

When the two systems operate in a combined fashion the time synchronization is not different from the anti-synchronous case, that is the first $\pi/2$ pulse on one system coincides with the second in the other system (see fig. 6.23) or, in other words, one system is interrogated while the other prepares the atoms in the right quantum state. However, in this case a substantial difference is present: only a single frequency correction is computed and shared by both systems. This means that a single clock laser is locked to two separate atomic systems without dead time, thus realizing the aforementioned ZDT clock.

In the ZDT clock the local oscillator is quasi-continuously referred to the atoms, strongly suppressing the aliasing effect. It can be seen in fig. 6.23 that the combined sensitivity function remains almost constantly equal to unity except for small variations during the short Ramsey pulses, meaning that the atomic susceptibility

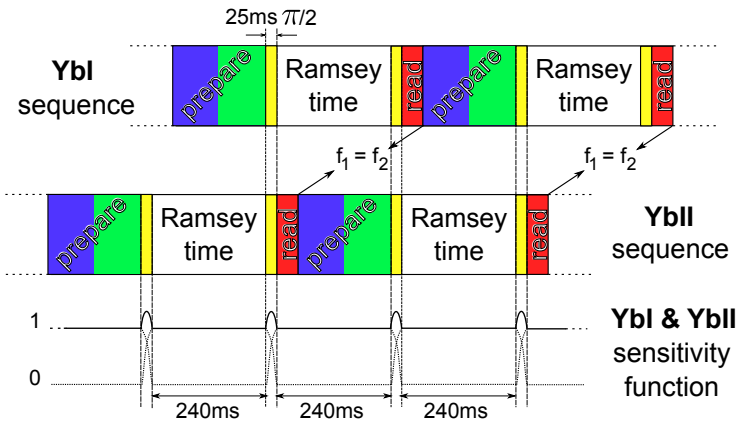

Figure 6.23: Zero-dead-time clock operation sequence and combined sensitivity function.

to the clock laser frequency noise at harmonics of the inverse of the cycle time $1/T_c$ is greatly reduced.

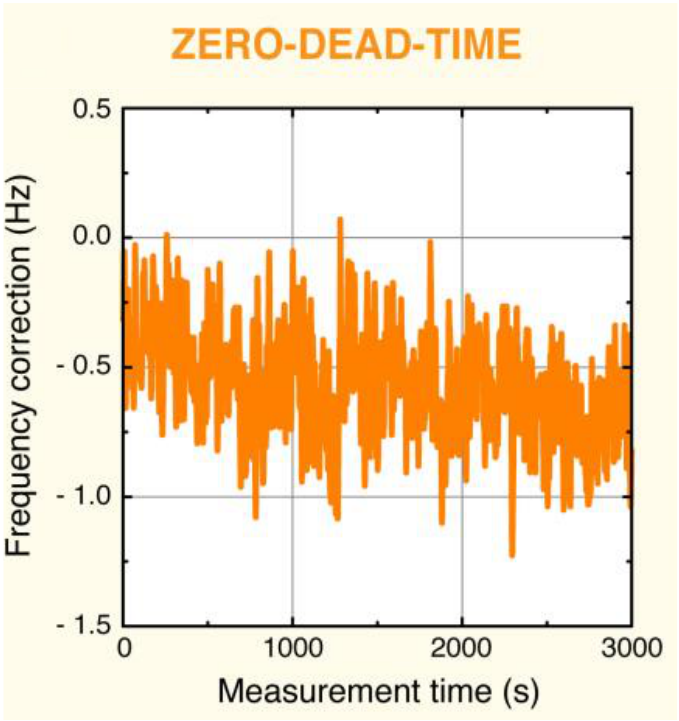

Figure 6.24: Shared frequency corrections applied every half of the cycle time to the composite YbI and YbII system, thus realizing the so called zero-dead-time clock. Lacking of an additional clock with similar performances to be used as external reference, the instability cannot be directly measured, but it is inferred using synchronous interrogations instead (see section 6.3.3 for details).

In particular, in the time domain, each system forming the ZDT clock is still sensitive to the Dick noise but, since the same clock laser pulse plays the role of first Ramsey pulse in one system and second in the other, the resulting effect has the same magnitude and opposite sign [123]. As a consequence, when the frequency correction is computed, the noise of the two systems is ruled out. To have an adequate rejection, the noise has to be correlated between the two atomic systems, meaning that each noise source not shared and related to a single system has to be controlled and compensated. Therefore, phase noise deriving from mechanical fluctuations of the optical fiber that delivers the light to the atoms is actively compensated by an AOM as described in 6.1. Moreover, the Ramsey pulses on the two systems are synchronized to be overlapped within 1 μs and are matched in shape at the 0.1 % level. Another detail to be taken into account is the magnetic field sensitivity of each atomic system. The clock operates interrogating the two Zeeman components of the clock feature (see sec. 2.3) and thus it is sensitive to differential magnetic field variations between the two systems. These variations are kept below the milligauss.

Since another comparable system to measure the stability is not available, in fig. 6.24 we can only report the shared frequency corrections of the clock laser in the ZDT stabilization process. Given the experimental conditions above, the evaluated Dick noise instability is $< 3 \times 10^{-18}/\sqrt{\tau}$, significantly below QPN (see fig. 6.20). An improved reduction can be made by a fine adjustment of the Ramsey pulses in order to obtain an even more uniform composite sensitivity function.

6.3.3 Synchronous interrogation

In this configuration the clocks run independently $\left(f_1(t) \neq f_2(t)\right)$ and are synchronized in order to perform the spectroscopic interrogation at the same time on both systems. As a consequence the frequency noise coming from the clock laser is common for the two systems and it is eliminated when the frequency difference is computed. The common-mode rejection of the aliasing noise allows an evaluation of a "Dick free" frequency stability which can be thus related to the ZDT performance as an experimental evaluation of its stability. The time sequence adopted for this measurement is shown in fig. 6.25 together with the sensitivity functions of the two clocks. Also in this case to have and effective noise rejection all the precautions described in the ZDT clock case are required.

The measured frequency instability reported in fig. 6.26 shows a white frequency noise slope which averages down as $8 \times 10^{-17}\sqrt{\tau}$. When we consider the ZDT clock for the same white noise process it averages down faster by a factor $\sqrt{2}$ because it accumulates, in the same time interval, twice the frequency corrections and atomic measures compared with the synchronous interrogation, giving a ZDT instability of $6 \times 10^{-17}/\sqrt{\tau}$. This result allows to reach a stability at the 10^{-18} level in few thousand seconds, which is an order of magnitude faster than previous reported

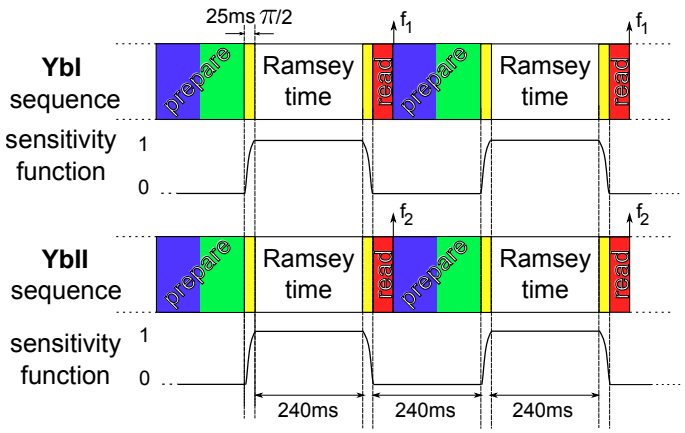

Figure 6.25: Synchronous interrogation sequence and clock sensitivity functions.

optical lattice clock stability [27, 124, 121, 125].

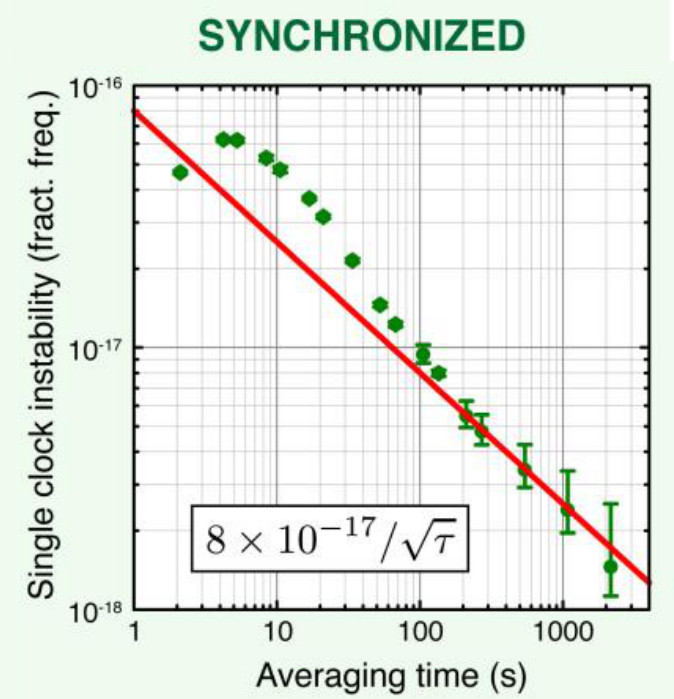

Figure 6.26: Single clock fractional frequency instability for the synchronous interrogation scheme. From [21].

To observe the quality of the suppression of the aliasing noise, an additional measurement was taken by intentionally injecting white frequency noise in the local oscillator while keeping the other experimental parameters unchanged. The noise was generated by a commercial synthesiser featuring a noise output port which was

plugged into the FM port of the synthesiser driving the frequency offset to the ultra-stable optical cavity. The additional noise is injected before the duplication crystal and before splitting the light in two branches for the two clocks, thus providing a correlated noise source for the two systems.

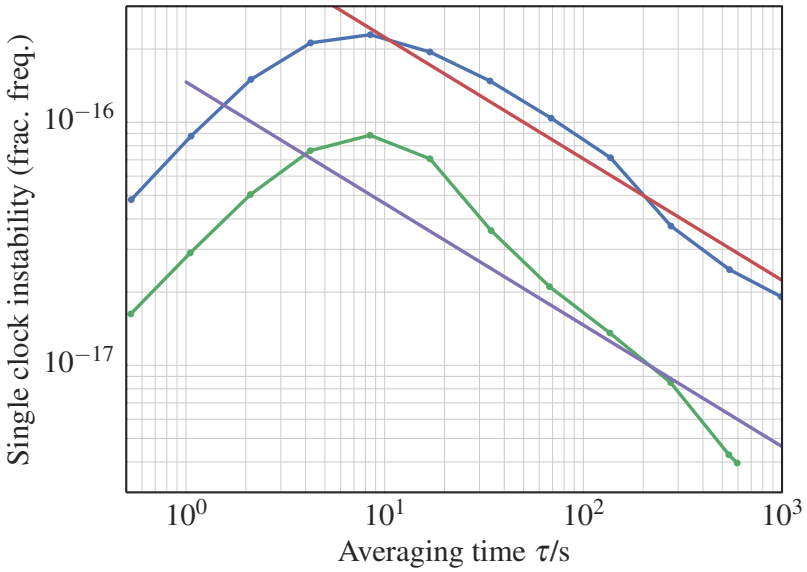

Figure 6.27: Fracional frequency stability for the anti-synchronized (blue) and synchronized (green) interrogation when an additional white frequency noise is added to the local oscillator. The Two lines represent the white noise at $7 \times 10^{-16}/\sqrt{\tau}$ (red) and $1.5 \times 10^{-16}/\sqrt{\tau}$ (purple) for the anti-synchronous and synchronous case respectively.

The resulting synchronized and anti-synchronized instability measurements are reported in fig. 6.27. The noise amplitude was enough to increase the instability of the anti-synchronized interrogation to $7 \times 10^{-16}/\sqrt{\tau}$. The synchronized instability, in this case was $1.5 \times 10^{-16}/\sqrt{\tau}$ showing an effective suppression of the additional noise. According to this reduction factor the level of rejection of the aliasing noise in the ZDT clock can be estimated to be $\sigma_{\text{Dick}} < 0.3 \times 10^{-17}/\sqrt{\tau}$ (see Tab. 6.3).

6.3.4 Two atomic system extended interrogation time

Besides addressing the Dick noise, two atomic systems can be used to increase the interrogation time beyond what the local oscillator coherence would permit and thus reducing the QPN. The idea is to make fast interrogations on one system to pre-stabilize the clock laser and, at the same time, perform a longer interrogation on the second atomic cloud.

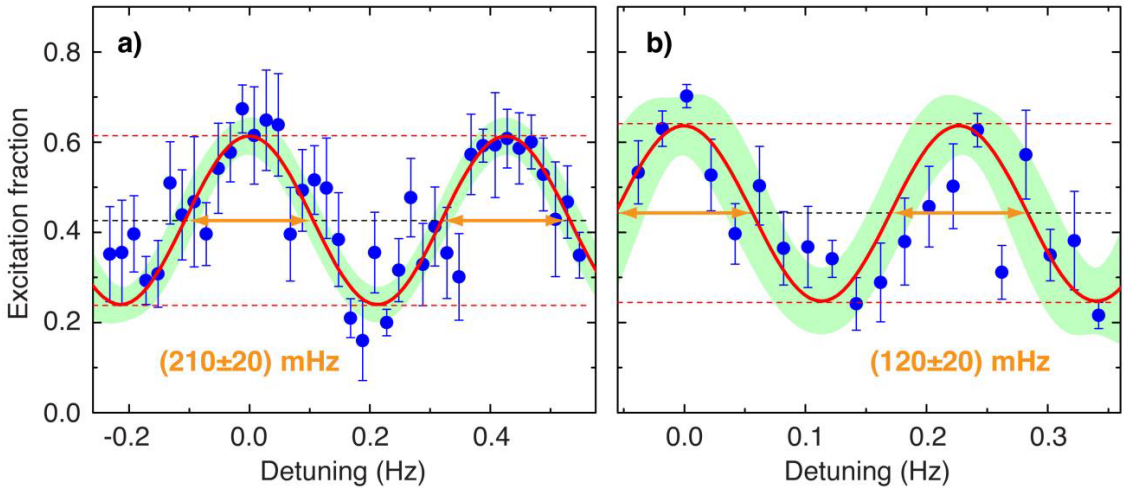

Figure 6.28: Ramsey fringes resulting from extended interrogation with a pre-stabilized clock laser. From [21]

Figure 6.28 shows the average of seven consecutive frequency sweeps over the Ramsey features when the clock laser is pre stabilized on YbI while YbII is probed up to 2.4 s and 4 s. For YbI the total cycle duration is 240 ms with a free evolution time of 110 ms, corresponding to 10 and 17 cycles per 2.4 s and 4 s long interrogation on YbII respectively. The linewidths of the obtained Fourier-limited fringes are 210(20) mHz and 120(20) mHz respectively, maintaining a contrast of 40 %. The narrow linewidth corresponds to a quality line factor of $Q > 4 \times 10^{15}$ which is one of the highest recorded in an optical lattice clock so far.

Inserting the factor Q in eq. (6.2), with the same experimental parameters mentioned earlier, the resulting QPN-limited fractional frequency stability is reduced to $5 \times 10^{-18}/\sqrt{\tau}$. It has to be noticed that the features shown in fig 6.28 are not enough reproducible from shot to shot and a frequency lock to them it is still not possible. This approach also retains a fraction of dead time, therefore the Dick noise suppression is moderate. In principle the system can be optimized to run as ZDT or with long interrogations depending on the relative amplitude of the QPN and Dick noise contributions. However, this exercise represent an experimental demonstration of the possibility of reducing QPN, the ultimate stability limit of the optical lattice clock, by the use of a composite atomic system.

6.4 Crystalline mirrors ring-down measure

In section 2.5 we saw how Brownian thermal noise affects the ultimate stability of ultra-stable cavities and the ways to reduce its impact. Among other approach, the improvement of the coating thermal properties could lead to a straightforward

increment in the cavity performances without the use of cryostatic techniques which are inconvenient from an experimental point of view.

Crystalline mirrors (CM) are recently emerging as candidate substitutes of dielectric mirrors which represent the present gold standard process technology for ultra-low loss (parts per million, ppm) reflectors in the visible and near-infrared region. This new technology, in particular, exhibits the highest thermal conductivity and the lowest Brownian thermal noise, which currently limits the best optical cavities in the world [64, 63]. However, given the novelty of the fabrication process, the candidate mirrors have to be carefully characterized in order to check the quality and uniformity of the coating in terms of optical losses.

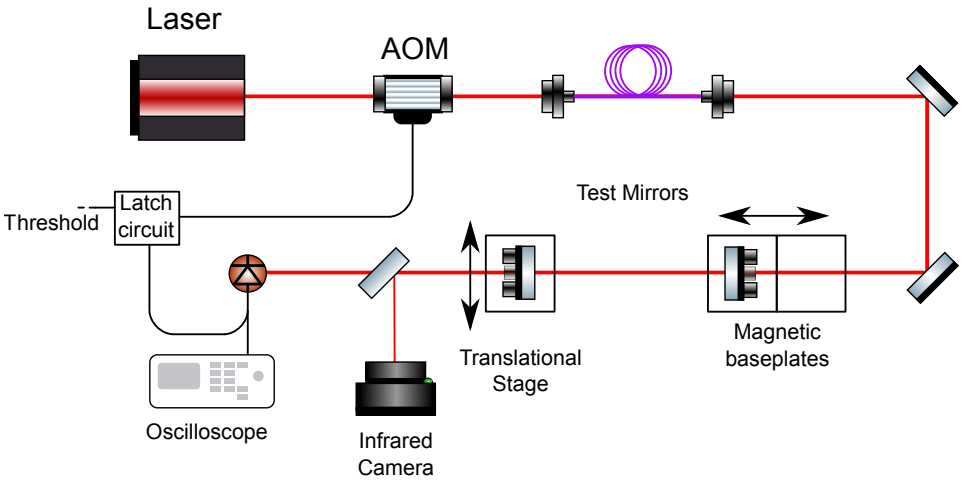

Figure 6.29: Experimental layout for the crystalline mirrors characterization using the cavity ring-down method.

The clock laser used in the Yb experiment at NIST is stabilized on an Ultra-Low Expansion (ULE) cavity equipped with dielectric mirrors. It has a total optical loss of about 7 ppm and its medium-term stability is limited by the Brownian thermal noise of the coating. A new optical cavity featuring crystalline mirrors is under development. I dealt with the optical performance measurement of some candidate mirrors.

We used the ring-down technique to estimate the extinction rate of laser light in the optical cavity. The set up features the 1156 nm light coming from the clock laser optical system via optical fiber. The beam passes through the optical cavity made by the test mirrors and the transmitted light is collected by a photo-diode which generates the measured signal. The cavity mirrors are mounted on magnetic base plates which allow to change easily the cavity length, while the output coupler mirror is mounted on a translational stage. The optical modes of the laser inside the cavity are monitored using In-Ga-As infra-red camera (see. fig. 6.29). The laser frequency is swept across a free spectral range using its piezo transducer. To

avoid the convolution of the frequency sweep with the ring-down measure a latching circuit was adopted to rapidly switch off the laser light (through an AOM) when the photodiode signal surpasses a certain threshold. The exponential decay is measured using an oscilloscope connected to the photodiode.

From the decay time of the transmitted light signal we want to estimate the optical losses of the cavity mirrors. At every passage of the light across the cavity the mode intensity is reduced by scattering and absorption taking place both on the mirrors and in the intracavity medium. At the i^{th} round trip the intensity is:

$$I_{i+1} = R_1 R_2 e^{-2\alpha L} I_i \tag{6.8}$$

where $R_{1(2)}$ is the reflectivity of the cavity mirror, α is the absorption coefficient of the intracavity medium per unit of length (ppm/cm) and L is the cavity length. In the limit of large number of round trips $N = \frac{ct}{2L} >> 1$, we have the well known exponential decay:

$$\frac{I(t)}{I_0} = \Big(\frac{I_{i+1}}{I_i}\Big)^N = (R_1 R_2)^{ct/2L} e^{-\alpha ct} = e^{-t/\tau} \tag{6.9}$$

in which we have the ring-down time

$$\tau = \frac{2L/c}{2\alpha L - \log R_1 R_2} \approx \frac{2L/c}{M_1 + M_2 + 2\alpha L} \tag{6.10}$$

where $M_{1(2)} = 1 - R_{1(2)}$ is the mirror loss and the denominator represents the total round-trip optical loss.

Since the cavity under test was in air, special care was given to the water vapour absorption. We operated the laser near 1156.74 nm where the absorption is minimized[5]. We validated the experimental procedure using three known dielectric coated mirrors (Layertec) and carefully evaluating the water absorption coefficient α by taking several measures at different cavity length and using:

$$\alpha = \frac{\eta_L - \eta_S}{2(L_L - l_S)} \tag{6.11}$$

where $\eta_{L(S)}$ is the measured optical loss and $L_{L(S)}$ is the cavity length in the case of long (short) mirrors distance. We measured two couples of mirrors (#1-#2 and #2-#3) obtaining consistent results for both $\alpha = 0.69(5)$ ppm/cm and mirror losses $M_1 \simeq M_2 \simeq M_3 = 5.3(10)$ ppm.

We then probed CM mirrors at different points across the surface in order to test the homogeneity of the coating. The CM mirror was mounted as output coupler on the translational stage and a dielectric test mirror as input coupler.

[5]HITRAN 2004 data

The mirror is horizontally moved and per each position a series of long-short ring down measurement were taken. An example of the result obtained for one test mirror is reported in table 6.4. The calibration run is in agreement with previous measurements obtained with Layertec mirrors. For crystalline mirrors, besides an α coefficient slightly lower to what expected, we obtained mirror losses in agreement to each other but too large to be acceptable, indicating a cavity finesse below 150 000. We suspect that position 0.0 mm indicates bad alignment, which prevents to hit the same spot on one of the two mirrors yielding to an anomalously large water absorption.

Table 6.4: Crystalline mirror losses and water absorption coefficient taken sweeping across the CMS mirror surface using a dielectric coated mirror as input coupler. The first row reports the calibration run with two dielectric coated mirrors (Layertec), in this case the mirror loss is related to the dielectric test mirror.

Position mm	α (ppm/cm)	mirror loss (ppm)
Cal. (Layertec)	0.66(2)	5.1(3)
−0.5	0.59(2)	25.6(4)
0.0	1.67(4)	14.1(6)
0.5	0.56(2)	22.0(4)
1.5	0.61(3)	24.0(5)

We repeated the same measurements using a different type of dielectric coated mirrors, produced by Advanced Thin Films (ATF). These mirrors were tested against the Layertec one and confirmed to have similar performances. The results with crystalline mirrors are reported in table 6.5. These measurements suffered from non-repeatability. We tried to repeat measures at a certain position at different times, without changing beam position or wavelength, obtaining a variation in ring-down times up to 100 %. Many subtle effects were not well understood like a strong dependency of the decay time on alignment and the cleaning technique.

Several attempts were made to achieve an optimal reliable procedure like using vacuum to avoid water absorption. We tried to make ring-down measurements using mirrors suction-mounted to a rigid ULE spacer with vacuum pump at $\sim$ 0.4 mbar intracavity pressure. This has the advantage of removing several degrees of freedom from the alignment, as well as reducing water absorption. However, due to the narrow 5 mm borehole (relative to the $\sim$ 1 mm incident beam), very careful centring must be done to avoid clipping the cavity mode with the spacer. A small misalignment ($\sim$ 1 mm) would result in a loss of more than $\sim$ 1 ppm. Due to the inability to consistently center the mirrors and the non reliable results,the idea was temporarily abandoned.

To improve the quality and reliability of the measurements are several measures can be taken like working under vacuum, improve the cleaning method of the

Table 6.5: Crystalline mirror losses and water absorption coefficient taken sweeping across the CMS mirror surface using a dielectric coated mirror (ATF). The first row reports the calibration run with two dielectric coated mirrors (ATF), in this case the mirror loss is related to the dielectric test mirror.

Position mm	α (ppm/cm)	mirror loss (ppm)
Cal. (ATF)	0.62(7)	5.7(3)
-1.0	0.81(40)	50.7(60)
0.0	1.42(2)	33.5(10)
1.0	$-1.83(200)$	115.0(460)

mirrors or using motorized optical mounts. The implementation of such solutions took place after my work period in the lab.

Chapter 7

Conclusions

The research carried out during my PhD has been devoted to the development and characterization of Ytterbium optical lattice frequency standards. Several achievements have been reached working in the laboratories of the Istituto Nazionale di Ricerca Metrologica (INRIM) and also at the National Institute of Standard and Technology (NIST), where I have been guest researcher in 2016.

My work on the INRIM Yb clock started when the spectroscopic line of the clock transition was fist observed on this system. Then, I focused my activities on the development and optimization of the 'atomic' part of the system, the one responsible to the preparation of the atomic ensemble before the spectroscopy. In particular, the laser power stabilization and the fiber noise cancellation system have been installed and tested (see sec. 3). At the same time, all lasers have been daily optimized and realigned to perform at their best during the measurements. The clock was then fully operative on daily basis and the complete the characterization of the clock systematic effects started. The result gave a total shift of 12.02(8) Hz that, in fractional units, correspond to $2320(15) \times 10^{-17}$ (sec. 5 and Tab. 5.1).

After the characterization, the absolute frequency measurement against the Italian primary frequency standard (ITCsF2) has been performed. The reference clock consists in a cryogenic Caesium atomic fountain which represents the best realization of the SI second in Italy and contributes also to the generation of national and international time scales. The frequency of the ^{171}Yb clock transition was measured to be $f_{^{171}\mathrm{Yb}} = 518\,295\,836\,590\,863.59(31)$ Hz. The detailed uncertainty budget (see sec. 5.4 and 5.2) shows that Yb clock outperforms the primary frequency standard which is indeed the major limit of the measurement. When this result is compared with the international context, it is in a very good agreement with the other measurements (see fig. 5.14). Notably, this is the first absolute frequency measurement of ^{171}Yb ever performed in Europe and the second ever performed against a primary frequency standard. This important scientific and metrological accomplishment contributed to the CIPM recommended frequency for Yb in 2017 and also resulted in a publication on Metrologia [25].

The activities on the INRIM clock continued upgrading the system in many different parts. In particular, stabilization of the MOT and lattice lasers has been completely revised with the design and implementation of the multi-wavelength cavity (sec. 4). This new system allows to frequency lock the three lasers on the same optical cavity at the same time using the same locking technique resulting in a reliable and easy to use tool for the lab activities. A thoroughly characterization of the locking system pointed out an anomalous optical absorption when 399 nm light is present inside the cavity which resulted in a degraded frequency drift. However, the presence of the 399 nm light is avoided by locking the 798 nm laser before being doubled. The performances of the system proved to be much better than the experimental requirements. In particular, the most stringent requirements were on the 556 nm laser which showed a linewidth below 300 Hz and a stability of 3×10^{-14} at 1 s. The measured drift when the three lasers were locked at the same time is below 20 kHz after 10 h at 759 nm which is compatible to a lattice light shift uncertainty below 10^{-18}. Moreover, the reliability of the clock improved reaching an entire day of continuous operation without any laser unlocks. This work was also published on Optics Letter in 2017 [79]

Among the different system changes reported in chapter 3, of particular importance is the upgrade of the clock laser which was the limiting factor of the clock instability. Indeed, a new measurement taken during the spring of 2017 showed a promising instability of $4 \times 10^{-15}/\sqrt{\tau}$ that paves the way for the forthcoming re-characterization of the clock at the 10^{-17} level.

As far as the activities carried out at NIST is concerned, they covered several different topics. Part of my work was dedicated to perform instability measurements using the two Yb optical lattice clocks present in the experiment (see sec. 6.3). This allowed to realize the so called zero-dead-time (ZDT) clock where the two clocks are merged to form a single, composite, system where the clock laser alternatively interrogates the two atomic samples. The interrogations are regulated in such a way that the dead time present in the single clock operation cycle is removed. Without dead time the Dick effect, which is the major clock instability source, vanishes, leading to an unprecedented instability of $6 \times 10^{-17}/\sqrt{\tau}$. Even if this technique have already been studied on microwave clocks, this represent the first implementation with optical lattice clocks. A further application of the two cold-atom ensembles is based on the pre-stabilization of the clock laser on one system running with fast cycles and an extended interrogation time on the second one. We demonstrated that is possible to extend the clock laser coherence and perform longer interrogation thus reducing the QPN limit. We also observed spectroscopy features with a quality factor of $Q > 4 \times 10^{15}$ (see fig. 6.28). These results were reported on an article on Nature Photonics in 2016 [21].

I have also dealt with the characterization of the two clocks at the level of 1.6×10^{-18} fractional uncertainty (see sec. 6.2 and Tab. 6.1). In particular, I worked

on the lattice light shift measurement taking into account non-linear effects like hyperpolarizability and the temperature of the atomic sample (see sec. 6.2.2). Results underlined the importance of a thoroughly characterization of higher order effects and temperature when accuracy approaches the 10^{-18} level and also provided a model that can be used to to control lattice shifts at the 10^{-19} level. Furthermore, it has been studied an interesting metrological regime called opperational magic wavelength where the combined effects of linear and quadratic lattice shifts result in a reduced sensitivity to trap depth fluctuations. This work on lattice light shift was worth the publication on Physical Review Letters [44].

The careful characterization of the clock required a meticulous evaluation of minor effects like background gas collisions and residual Doppler noise. Collisions among the Yb sample atoms and the background gas (H_2) have been measured confirming the theoretical expectations. This effect contributes for 8×10^{-19} of fractional uncertainty and constitutes the first evaluation of C_6 coefficients in the case of Yb−H collisions. Residual Doppler effects arise from phase noise seen by the atoms held in the lattice when probed by the clock laser. By making the lattice retro-reflector the reference mirror for the fiber noise cancellation system the impact of this effect has been evaluated to be lower than 10^{-19} level.

I also had the opportunity to test some of the crystalline mirrors which are one of the most promising technologies for next generation ultra-stable optical cavities. Unfortunately, the measurements suffered of a poor reproducibility probably caused by experimental conditions. Results indicate, even if not clearly, that the reflectivity of the mirrors under test was much worse than the dielectric reference mirrors used, with a non uniform performance across the mirror surface.

Bibliography

[1] L. D. Landau and E. M. Lifshitz. *Quantum mechanics - Non-relativistic theory*. 3rd. Vol. 3. Course of Theoretical Physics. Pergamon Press, 1977.

[2] L. Essen and J. V. L. Parry. "An Atomic Standard of Frequency and Time Interval: A Caesium Resonator". In: *Nature* 176.4476 (Aug. 1955), pp. 280–282. URL: http://dx.doi.org/10.1038/176280a0.

[3] W. Markowitz et al. "Frequency of Cesium in Terms of Ephemeris Time". In: *Phys. Rev. Lett.* 1 (3 Aug. 1958), pp. 105–107. DOI: 10.1103/PhysRevLett.1.105. URL: http://link.aps.org/doi/10.1103/PhysRevLett.1.105.

[4] BIPM. *The International System of Units (SI)*. 8th. BIPM, 2006.

[5] D.W. Allan. "Statistics of atomic frequency standards". In: *Proc. IEEE* 54.2 (Feb. 1966), pp. 221–230. ISSN: 0018-9219. DOI: 10.1109/PROC.1966.4634.

[6] W. M. Itano et al. "Quantum projection noise: Population fluctuations in two-level systems". In: *Phys. Rev. A* 47 (5 May 1993), pp. 3554–3570. DOI: 10.1103/PhysRevA.47.3554. URL: http://link.aps.org/doi/10.1103/PhysRevA.47.3554.

[7] Andrew D. Ludlow et al. "Optical atomic clocks". In: *Rev. Mod. Phys.* 87 (2 June 2015), pp. 637–701. DOI: 10.1103/RevModPhys.87.637. URL: http://link.aps.org/doi/10.1103/RevModPhys.87.637.

[8] Harold J. Metcalf and Peter van der Straten. *Laser cooling and trapping*. New York: Springer, 2002. ISBN: 0-387-98728-2.

[9] Norman F. Ramsey. "A Molecular Beam Resonance Method with Separated Oscillating Fields". In: *Phys. Rev.* 78 (6 June 1950), pp. 695–699. DOI: 10.1103/PhysRev.78.695. URL: http://link.aps.org/doi/10.1103/PhysRev.78.695.

[10] Jon H Shirley, WD Lee, and Robert E Drullinger. "Accuracy evaluation of the primary frequency standard NIST-7". In: *Metrologia* 38.5 (2001), p. 427.

[11] D. Kleppner et al. "Hydrogen-Maser Principles and Techniques". In: *Phys. Rev.* 138 (4A May 1965), A972–A983. DOI: 10.1103/PhysRev.138.A972. URL: https://link.aps.org/doi/10.1103/PhysRev.138.A972.

[12] R. J. Carpenter et al. “A Prototype Rubidium Vapor Frequency Standard”. In: *IRE Transactions on Instrumentation* I-9.2 (Sept. 1960), pp. 132–135. ISSN: 0096-2260. DOI: 10.1109/IRE-I.1960.5006903.

[13] Filippo Levi et al. “Accuracy evaluation of ITCsF2: a nitrogen cooled caesium fountain”. In: *Metrologia* 51.3 (2014), p. 270. URL: http://stacks.iop.org/0026-1394/51/i=3/a=270.

[14] N. Huntemann et al. “Single-Ion Atomic Clock with 3×10^{-18} Systematic Uncertainty”. In: *Phys. Rev. Lett.* 116 (6 Feb. 2016), p. 063001. DOI: 10.1103/PhysRevLett.116.063001. URL: https://link.aps.org/doi/10.1103/PhysRevLett.116.063001.

[15] Pierre Dubé et al. “High-Accuracy Measurement of the Differential Scalar Polarizability of a $^{88}Sr^{+}$ Clock Using the Time-Dilation Effect”. In: *Phys. Rev. Lett.* 112 (17 Apr. 2014), p. 173002. DOI: 10.1103/PhysRevLett.112.173002. URL: http://link.aps.org/doi/10.1103/PhysRevLett.112.173002.

[16] C. W. Chou et al. “Frequency Comparison of Two High-Accuracy Al^{+} Optical Clocks”. In: *Phys. Rev. Lett.* 104 (7 Feb. 2010), p. 070802. DOI: 10.1103/PhysRevLett.104.070802. URL: http://link.aps.org/doi/10.1103/PhysRevLett.104.070802.

[17] W. H. Oskay et al. “Single-Atom Optical Clock with High Accuracy”. In: *Phys. Rev. Lett.* 97 (2 July 2006), p. 020801. DOI: 10.1103/PhysRevLett.97.020801. URL: http://link.aps.org/doi/10.1103/PhysRevLett.97.020801.

[18] Wolfgang Paul. “Electromagnetic traps for charged and neutral particles”. In: *Rev. Mod. Phys.* 62 (3 July 1990), pp. 531–540. DOI: 10.1103/RevModPhys.62.531. URL: https://link.aps.org/doi/10.1103/RevModPhys.62.531.

[19] David J. Wineland. “Nobel Lecture: Superposition, entanglement, and raising Schrödinger’s cat”. In: *Rev. Mod. Phys.* 85 (3 July 2013), pp. 1103–1114. DOI: 10.1103/RevModPhys.85.1103. URL: https://link.aps.org/doi/10.1103/RevModPhys.85.1103.

[20] Hidetoshi Katori et al. “Ultrastable Optical Clock with Neutral Atoms in an Engineered Light Shift Trap”. In: *Phys. Rev. Lett.* 91 (17 Oct. 2003), p. 173005. DOI: 10.1103/PhysRevLett.91.173005. URL: http://link.aps.org/doi/10.1103/PhysRevLett.91.173005.

[21] M. Schioppo et al. “Ultra-stable optical clock with two cold-atom ensembles”. In: *Nat. Photon.* 11.1 (Jan. 2017), pp. 48–52. URL: http://dx.doi.org/10.1038/nphoton.2016.231.

[22] K. M. Evenson et al. "Speed of Light from Direct Frequency and Wavelength Measurements of the Methane-Stabilized Laser". In: *Phys. Rev. Lett.* 29 (19 Nov. 1972), pp. 1346–1349. DOI: 10.1103/PhysRevLett.29.1346. URL: http://link.aps.org/doi/10.1103/PhysRevLett.29.1346.

[23] Th. Udem et al. "Phase-Coherent Measurement of the Hydrogen $1S - 2S$ Transition Frequency with an Optical Frequency Interval Divider Chain". In: *Phys. Rev. Lett.* 79 (14 Oct. 1997), pp. 2646–2649. DOI: 10.1103/PhysRevLett.79.2646. URL: https://link.aps.org/doi/10.1103/PhysRevLett.79.2646.

[24] John L. Hall. "Nobel Lecture: Defining and measuring optical frequencies". In: *Rev. Mod. Phys.* 78 (4 Nov. 2006), pp. 1279–1295. DOI: 10.1103/RevModPhys.78.1279. URL: https://link.aps.org/doi/10.1103/RevModPhys.78.1279.

[25] M. Pizzocaro et al. "Absolute frequency measurement of the $^1S_0 - {}^3P_0$ transition of ^{171}Yb". In: *Metrologia* 54 (Feb. 2017), p. 102. arXiv: 1609.01610 [physics.atom-ph].

[26] Sergey G. Porsev, Andrei Derevianko, and E. N. Fortson. "Possibility of an optical clock using the 6 ^{1}S$_0$ $\rightarrow$ 6 ^{3}P$_0{}^o$ transition in ^{171,173}Yb atoms held in an optical lattice". In: *Phys. Rev. A* 69.2 (Feb. 2004), p. 021403. DOI: 10.1103/PhysRevA.69.021403. URL: http://pra.aps.org/abstract/PRA/v69/i2/e021403.

[27] N. Hinkley et al. "An Atomic Clock with 10^{-18} Instability". In: *Science* 341.6151 (2013), pp. 1215–1218. DOI: 10.1126/science.1240420. URL: http://www.sciencemag.org/content/341/6151/1215.abstract.

[28] Nils Nemitz et al. "Frequency ratio of Yb and Sr clocks with 5×10^{-17} uncertainty at 150 seconds averaging time". In: *Nat Photon* advance online publication (Feb. 2016), pp. –. ISSN: 1749-4893. URL: http://dx.doi.org/10.1038/nphoton.2016.20.

[29] Chang Yong Park et al. "Absolute frequency measurement of ^{1}S$_0$ ($F = 1/2$) - ^{3}P$_0$ ($F = 1/2$) transition of ^{171}Yb atoms in a one-dimensional optical lattice at KRISS". In: *Metrologia* 50.2 (2013), p. 119. URL: http://stacks.iop.org/0026-1394/50/i=2/a=119.

[30] CIPM. *CIPM Reccomendation 2 - Updated list of standard frequencies*. 2015. URL: http://www.bipm.org/utils/en/pdf/CIPMOutcomes/CI-2015-Recommendation-2.pdf.

[31] C. W. Chou et al. "Optical Clocks and Relativity". In: *Science* 329.5999 (2010), pp. 1630–1633. ISSN: 0036-8075. DOI: 10.1126/science.1192720. eprint: http://science.sciencemag.org/content/329/5999/1630.full.pdf. URL: http://science.sciencemag.org/content/329/5999/1630.

[32] Jacopo Grotti et al. "Geodesy and metrology with a transportable optical clock". In: *arXiv preprint arXiv:1705.04089* (2017).

[33] N. Huntemann et al. "Improved Limit on a Temporal Variation of m_p/m_e from Comparisons of Yb^+ and Cs Atomic Clocks". In: *Phys. Rev. Lett.* 113 (21 Nov. 2014), p. 210802. DOI: 10.1103/PhysRevLett.113.210802. URL: http://link.aps.org/doi/10.1103/PhysRevLett.113.210802.

[34] Cédric Delaunay and Yotam Soreq. "Probing new physics with isotope shift spectroscopy". In: *arXiv preprint arXiv:1602.04838* (2016).

[35] Cecilia Clivati et al. "A VLBI experiment using a remote atomic clock via a coherent fibre link". In: *Scientific Reports* 7 (2017), p. 40992.

[36] John D Prestage et al. "Progress on small mercury ion clock for space applications". In: *Frequency Control Symposium, 2009 Joint with the 22nd European Frequency and Time forum. IEEE International*. IEEE. 2009, pp. 54–57.

[37] R. Le Targat et al. "Experimental realization of an optical second with strontium lattice clocks". In: *Nat Commun* 4 (July 2013), p. 2109. URL: http://dx.doi.org/10.1038/ncomms3109.

[38] Massimo Inguscio and Leonardo Fallani. *Atomic Physics: Precise Measurements and Ultracold Matter*. 2nd. Oxford University Press, 2015.

[39] C. C. Tannoudj and D. Guéry-Odlein. *Advances in atomic physics: an overview*. World Scientific, 2011. ISBN: 978-981-227-497-2.

[40] Steven Chu. "Nobel Lecture: The manipulation of neutral particles". In: *Rev. Mod. Phys.* 70 (3 July 1998), pp. 685–706. DOI: 10.1103/RevModPhys.70.685. URL: https://link.aps.org/doi/10.1103/RevModPhys.70.685.

[41] Claude N. Cohen-Tannoudji. "Nobel Lecture: Manipulating atoms with photons". In: *Rev. Mod. Phys.* 70 (3 July 1998), pp. 707–719. DOI: 10.1103/RevModPhys.70.707. URL: https://link.aps.org/doi/10.1103/RevModPhys.70.707.

[42] William D. Phillips. "Nobel Lecture: Laser cooling and trapping of neutral atoms". In: *Rev. Mod. Phys.* 70 (3 July 1998), pp. 721–741. DOI: 10.1103/RevModPhys.70.721. URL: https://link.aps.org/doi/10.1103/RevModPhys.70.721.

[43] N. D. Leme. "Optical lattice clockwith spin 1/2 Yb atoms". PhD thesis. University of Colorado, 2012.

[44] R. C. Brown et al. "Hyperpolarizability and operational magic wavelength in an optical lattice clock". In: (2017). eprint: arXiv:1708.08829.

[45] H. Katori. "Spectroscopy of Strontium Atoms in the Lamb-Dicke Confinement". In: *Frequency Standards and Metrology*. Ed. by P. Gill. Apr. 2002, pp. 323–330. DOI: 10.1142/9789812777713_0036.

[46] A. V. Taichenachev et al. "Frequency Shifts in an Optical Lattice Clock Due to Magnetic-Dipole and Electric-Quadrupole Transitions". In: *Phys. Rev. Lett.* 101 (19 Nov. 2008), p. 193601. DOI: 10.1103/PhysRevLett.101.193601. URL: https://link.aps.org/doi/10.1103/PhysRevLett.101.193601.

[47] Z. W. Barber et al. "Optical Lattice Induced Light Shifts in an Yb Atomic Clock". In: *Phys. Rev. Lett.* 100 (10 Mar. 2008), p. 103002. DOI: 10.1103/PhysRevLett.100.103002. URL: http://link.aps.org/doi/10.1103/PhysRevLett.100.103002.

[48] Hidetoshi Katori et al. "Strategies for reducing the light shift in atomic clocks". In: *Phys. Rev. A* 91 (5 May 2015), p. 052503. DOI: 10.1103/PhysRevA.91.052503. URL: http://link.aps.org/doi/10.1103/PhysRevA.91.052503.

[49] Martin M. Boyd et al. "Nuclear spin effects in optical lattice clocks". In: *Phys. Rev. A* 76 (2 Aug. 2007), p. 022510. DOI: 10.1103/PhysRevA.76.022510. URL: https://link.aps.org/doi/10.1103/PhysRevA.76.022510.

[50] N. D. Lemke et al. "p-Wave Cold Collisions in an Optical Lattice Clock". In: *Phys. Rev. Lett.* 107 (10 Aug. 2011), p. 103902. DOI: 10.1103/PhysRevLett.107.103902. URL: http://link.aps.org/doi/10.1103/PhysRevLett.107.103902.

[51] Jacques Vanier and Claude Audoin. *The Quantum Physics of Atomic Frequency Standards*. Ed. by A. E. Bailey. Bristol, England: Adam Hilger, 1989.

[52] R. W. P. Drever et al. "Laser phase and frequency stabilization using an optical resonator". In: *Appl. Phys. B* 31.2 (June 1983), pp. 97–105. DOI: 10.1007/BF00702605. URL: http://www.springerlink.com/content/rgg2823656435593/.

[53] T.W. Hänsch and B. Couillaud. "Laser frequency stabilization by polarization spectroscopy of a reflecting reference cavity". In: *Opt. Commun.* 35.3 (1980), pp. 441–444. ISSN: 0030-4018. DOI: 10.1016/0030-4018(80)90069-3. URL: http://www.sciencedirect.com/science/article/B6TVF-46FR1KK-TC/2/18877ced11006bcbf37db8288bcafd7f.

[54] Wolfgang Demtröder. *Laser spectroscopy: basic concepts and instrumentation*. Third. Springer, 2003.

[55] Michael J. Thorpe et al. "Frequency stabilization to 6×10^{-16} via spectral-hole burning". In: *Nat Photon* 5.11 (Nov. 2011), pp. 688–693. ISSN: 1749-4885. URL: http://dx.doi.org/10.1038/nphoton.2011.215.

[56] Nur Ismail et al. "Fabry-Perot resonator: spectral line shapes, generic and related Airy distributions, linewidths, finesses, and performance at low or frequency-dependent reflectivity". In: *Opt. Express* 24.15 (July 2016), pp. 16366–16389. DOI: 10.1364/OE.24.016366. URL: http://www.opticsexpress.org/abstract.cfm?URI=oe-24-15-16366.

[57] Jan Haisma and G.A.C.M. Spierings. "Contact bonding, including direct-bonding in a historical and recent context of materials science and technology, physics and chemistry: Historical review in a broader scope and comparative outlook". In: *Materials Science and Engineering: R: Reports* 37.1 (2002), pp. 1–60. ISSN: 0927-796X. DOI: https://doi.org/10.1016/S0927-796X(02)00003-7. URL: http://www.sciencedirect.com/science/article/pii/S0927796X02000037.

[58] T. Nazarova, F. Riehle, and U. Sterr. "Vibration-insensitive reference cavity for an ultra-narrow-linewidth laser". English. In: *Appl. Phys. B* 83 (4 2006), pp. 531–536. ISSN: 0946-2171. DOI: 10.1007/s00340-006-2225-y. URL: http://dx.doi.org/10.1007/s00340-006-2225-y.

[59] M. Pizzocaro et al. "Realization of an ultrastable 578-nm laser for an Yb lattice clock". In: *IEEE Trans. Ultrason., Ferroelect., Freq. Cont.* 59.3 (Mar. 2012), pp. 426–431. ISSN: 0885-3010. DOI: 10.1109/TUFFC.2012.2211.

[60] Kenji Numata, Amy Kemery, and Jordan Camp. "Thermal-Noise Limit in the Frequency Stabilization of Lasers with Rigid Cavities". In: *Phys. Rev. Lett.* 93.25 (Dec. 2004), p. 250602. DOI: 10.1103/PhysRevLett.93.250602.

[61] Thomas Legero et al. "1.5 μm Lasers with Sub10 mHz Linewidth". In: *Conference on Lasers and Electro-Optics*. Optical Society of America, 2017, SW1J.1. DOI: 10.1364/CLEO_SI.2017.SW1J.1. URL: http://www.osapublishing.org/abstract.cfm?URI=CLEO_SI-2017-SW1J.1.

[62] T. Kessler et al. "A sub-40-mHz-linewidth laser based on a silicon single-crystal optical cavity". In: *Nat. Photon.* 6.10 (Oct. 2012), pp. 687–692. ISSN: 1749-4885. URL: http://dx.doi.org/10.1038/nphoton.2012.217.

[63] Garrett D. Cole et al. "High-performance near- and mid-infrared crystalline coatings". In: *Optica* 3.6 (June 2016), pp. 647–656. DOI: 10.1364/OPTICA.3.000647. URL: http://www.osapublishing.org/optica/abstract.cfm?URI=optica-3-6-647.

[64] Garrett D. Cole et al. "Tenfold reduction of Brownian noise in high-reflectivity optical coatings". In: *Nat Photon* 7.8 (Aug. 2013), pp. 644–650. ISSN: 1749-4885. URL: http://dx.doi.org/10.1038/nphoton.2013.174.

[65] Eric D. Black. "An introduction to Pound-Drever-Hall laser frequency stabilization". In: *Amer. J. Phys.* 69.1 (2001), pp. 79–87. DOI: 10.1119/1.1286663. URL: http://link.aip.org/link/?AJP/69/79/1.

[66] J. I. Thorpe, K. Numata, and J. Livas. "Laser frequency stabilization and control through offset sideband locking to optical cavities". In: *Opt. Express* 16.20 (Sept. 2008), pp. 15980–15990. DOI: 10.1364/OE.16.015980. URL: http://www.opticsexpress.org/abstract.cfm?URI=oe-16-20-15980.

[67] Pierre Lemonde et al. "Cold-atom clocks on Earth and in space". In: *Frequency measurement and control*. Springer, 2001, pp. 131–153.

[68] G.J. Dick. *Local oscillator induced instabilities in trapped ion frequency standards*. Tech. rep. DTIC Document, 1987.

[69] G. Santarelli et al. "Frequency stability degradation of an oscillator slaved to a periodically interrogated atomic resonator". In: *IEEE Trans. Ultrason., Ferroelect., Freq. Cont.* 45.4 (July 1998), pp. 887–894. ISSN: 0885-3010. DOI: 10.1109/58.710548.

[70] Andrew D. Ludlow. "The Strontium Optical Lattice Clock: Optical Spectroscopy with Sub-Hertz Accuracy". PhD thesis. University of Colorado, 2008.

[71] P. G. Westergaard, J. Lodewyck, and P. Lemonde. "Minimizing the dick effect in an optical lattice clock". In: *IEEE Transactions on Ultrasonics, Ferroelectrics, and Frequency Control* 57.3 (Mar. 2010), pp. 623–628. ISSN: 0885-3010. DOI: 10.1109/TUFFC.2010.1457.

[72] Marco Pizzocaro. "Realization and characterization of optical frequency standards". PhD thesis. Politecnico di Torino, Feb. 2013. DOI: 10.6092/polito/porto/2506152. URL: http://porto.polito.it/2506152/.

[73] William D. Phillips and Harold Metcalf. "Laser Deceleration of an Atomic Beam". In: *Phys. Rev. Lett.* 48 (9 Mar. 1982), pp. 596–599. DOI: 10.1103/PhysRevLett.48.596. URL: http://link.aps.org/doi/10.1103/PhysRevLett.48.596.

[74] W. P. Risk, T. R. Gosnell, and A. V. Nurmikko. *Compact Blue-Green Lasers*. New York: Cambridge University Press, 2003. URL: www.cambridge.org/9780521623186.

[75] Marco Pizzocaro et al. "Efficient frequency doubling at 399 nm". In: *Appl. Opt.* 53.16 (June 2014), pp. 3388–3392. DOI: 10.1364/AO.53.003388. URL: http://ao.osa.org/abstract.cfm?URI=ao-53-16-3388.

[76] Filippo Bregolin. "Operation of the ^{171}Yb optical lattice clock". Tesi di Laurea Specialistica. Università degli Studi di Torino, 2015.

[77] E. A. Donley et al. "Double-pass acousto-optic modulator system". In: *Rev. Sci. Inst.* 76.6, 063112 (2005), p. 063112. DOI: 10.1063/1.1930095. URL: http://link.aip.org/link/?RSI/76/063112/1.

[78] M. Pizzocaro et al. "Active disturbance rejection control of temperature for ultrastable optical cavities". In: *IEEE Trans. Ultrason., Ferroelect., Freq. Cont.* 60.2 (Feb. 2013), pp. 273–280. ISSN: 0885-3010. DOI: 10.1109/TUFFC.2013.2563.

[79] Gianmaria Milani et al. "Multiple wavelength stabilization on a single optical cavity using the offset sideband locking technique". In: *Opt. Lett.* 42.10 (May 2017), pp. 1970–1973. DOI: 10.1364/OL.42.001970. URL: http://ol.osa.org/abstract.cfm?URI=ol-42-10-1970.

[80] M. Pizzocaro et al. "Active disturbance rejection control of temperature for ultrastable optical cavities". In: vol. 60. 2. Feb. 2013, pp. 273–280. DOI: 10.1109/TUFFC.2013.2563.

[81] Gianni Di Domenico, Stéphane Schilt, and Pierre Thomann. "Simple approach to the relation between laser frequency noise and laser line shape". In: *Appl. Opt.* 49.25 (Sept. 2010), pp. 4801–4807. DOI: 10.1364/AO.49.004801. URL: http://ao.osa.org/abstract.cfm?URI=ao-49-25-4801.

[82] T. M. Brzozowski et al. "Time-of-flight measurement of the temperature of cold atoms for short trap-probe beam distances". In: *Journal of Optics B: Quantum and Semiclassical Optics* 4.1 (2002), p. 62.

[83] H. G. Dehmelt. "Monoion oscillator as potential ultimate laser frequency standard". In: *IEEE Transactions on Instrumentation and Measurement* IM-31.2 (June 1982), pp. 83–87. ISSN: 0018-9456. DOI: 10.1109/TIM.1982.6312526.

[84] Zeb W. Barber. "Ytterbium Optical Lattice Clock". PhD thesis. University of Colorado, 2007.

[85] S. Blatt et al. "Rabi spectroscopy and excitation inhomogeneity in a one-dimensional optical lattice clock". In: *Phys. Rev. A* 80 (5 Nov. 2009), p. 052703. DOI: 10.1103/PhysRevA.80.052703. URL: http://link.aps.org/doi/10.1103/PhysRevA.80.052703.

[86] Z. W. Barber et al. "Direct Excitation of the Forbidden Clock Transition in Neutral ^{174}Yb Atoms Confined to an Optical Lattice". In: *Phys. Rev. Lett.* 96.8 (Mar. 2006), p. 083002. DOI: 10.1103/PhysRevLett.96.083002.

[87] N. D. Lemke et al. "Spin-1/2 Optical Lattice Clock". In: *Phys. Rev. Lett.* 103.6 (Aug. 2009), p. 063001. DOI: 10.1103/PhysRevLett.103.063001.

[88] A. D. Ludlow et al. "Cold-collision-shift cancellation and inelastic scattering in a Yb optical lattice clock". In: *Phys. Rev. A* 84 (5 Nov. 2011), p. 052724. DOI: 10.1103/PhysRevA.84.052724. URL: http://link.aps.org/doi/10.1103/PhysRevA.84.052724.

[89] J. A. Sherman et al. "High-Accuracy Measurement of Atomic Polarizability in an Optical Lattice Clock". In: *Phys. Rev. Lett.* 108 (15 Apr. 2012), p. 153002. DOI: 10.1103/PhysRevLett.108.153002. URL: http://link.aps.org/doi/10.1103/PhysRevLett.108.153002.

[90] K. Beloy et al. "Atomic Clock with 1×10^{-18} Room-Temperature Blackbody Stark Uncertainty". In: *Phys. Rev. Lett.* 113 (26 Dec. 2014), p. 260801. DOI: 10.1103/PhysRevLett.113.260801. URL: http://link.aps.org/doi/10.1103/PhysRevLett.113.260801.

[91] BIPM et al. *Evaluation of measurement data - Guide to the expression of uncertainty in measurement*. Ed. by Joint Committee for Guides in Metrology. Joint Committee for Guides in Metrology, JCGM 100. 2008. URL: http://www.bipm.org/en/publications/guides/gum.html.

[92] R. F. C. Vessot et al. "Test of Relativistic Gravitation with a Space-Borne Hydrogen Maser". In: *Phys. Rev. Lett.* 45 (26 Dec. 1980), pp. 2081–2084. DOI: 10.1103/PhysRevLett.45.2081. URL: https://link.aps.org/doi/10.1103/PhysRevLett.45.2081.

[93] H.S. Margolis et al. "International timescales with optical clocks (ITOC)". In: *European Frequency and Time Forum International Frequency Control Symposium (EFTF/IFC), 2013 Joint*. July 2013, pp. 908–911. DOI: 10.1109/EFTF-IFC.2013.6702183.

[94] H Denker, L Timmen, and C Voigt. "Gravity field modelling with regard to optical clock comparisons". In: *XXVI General Assembly of the International Union of Geodesy and Geophysics (IUGG), Earth and Environmental Sciences for Future Generations (Prague, Czech Republic, 22 June–02 July 2015)* (2015).

[95] D Calonico et al. "Gravitational redshift at INRIM". In: *Metrologia* 44.5 (2007), p. L44. URL: http://stacks.iop.org/0026-1394/44/i=5/a=N03.

[96] S. Falke et al. "Delivering pulsed and phase stable light to atoms of an optical clock". In: *Applied Physics B* 107.2 (May 2012), pp. 301–311. ISSN: 1432-0649. DOI: 10.1007/s00340-012-4952-6. URL: https://doi.org/10.1007/s00340-012-4952-6.

[97] J. Lodewyck et al. "Observation and cancellation of a perturbing dc stark shift in strontium optical lattice clocks". In: *IEEE Trans. Ultrason., Ferroelect., Freq. Cont.* 59.3 (Mar. 2012), pp. 411–415. ISSN: 0885-3010. DOI: 10.1109/TUFFC.2012.2209.

[98] Kurt Gibble. "Scattering of Cold-Atom Coherences by Hot Atoms: Frequency Shifts from Background-Gas Collisions". In: *Phys. Rev. Lett.* 110 (18 May 2013), p. 180802. DOI: 10.1103/PhysRevLett.110.180802. URL: https://link.aps.org/doi/10.1103/PhysRevLett.110.180802.

[99] S. G. Porsev et al. "Long-range interaction coefficients for ytterbium dimers". In: *Phys. Rev. A* 89 (1 Jan. 2014), p. 012711. DOI: 10.1103/PhysRevA.89.012711. URL: https://link.aps.org/doi/10.1103/PhysRevA.89.012711.

[100] Pierre Lemonde and Peter Wolf. "Optical lattice clock with atoms confined in a shallow trap". In: *Phys. Rev. A* 72 (3 Sept. 2005), p. 033409. DOI: 10.1103/PhysRevA.72.033409. URL: https://link.aps.org/doi/10.1103/PhysRevA.72.033409.

[101] Philip G. Westergaard. "Horloge à rèseau optique au Strontium: en quête de la performance ultime". PhD thesis. Edite De Paris, 2010.

[102] HS Margolis and P Gill. "Least-squares analysis of clock frequency comparison data to deduce optimized frequency and frequency ratio values". In: *Metrologia* 52.5 (2015), p. 628.

[103] David G Luenberger. *Optimization by vector space methods*. John Wiley & Sons, 1997.

[104] MG Cox et al. "The generalized weighted mean of correlated quantities". In: *Metrologia* 43.4 (2006), S268.

[105] Daisuke Akamatsu et al. "Frequency ratio measurement of 171Yb and 87Sr optical lattice clocks". In: *Opt. Express* 22.7 (Apr. 2014), pp. 7898–7905. DOI: 10.1364/OE.22.007898. URL: http://www.opticsexpress.org/abstract.cfm?URI=oe-22-7-7898.

[106] Masao Takamoto et al. "Frequency ratios of Sr, Yb, and Hg based optical lattice clocks and their applications". In: *Comptes Rendus Physique* 16.5 (2015). The measurement of time / La mesure du temps, pp. 489–498. ISSN: 1631-0705. DOI: http://dx.doi.org/10.1016/j.crhy.2015.04.003. URL: http://www.sciencedirect.com/science/article/pii/S1631070515000730.

[107] Takuya Kohno et al. "One-Dimensional Optical Lattice Clock with a Fermionic ^{171}Yb Isotope". In: *Applied Physics Express* 2.7 (2009), p. 072501. DOI: 10.1143/APEX.2.072501. URL: http://apex.jsap.jp/link?APEX/2/072501/.

[108] Masami Yasuda et al. "Improved Absolute Frequency Measurement of the ^{171}Yb Optical Lattice Clock towards a Candidate for the Redefinition of the Second". In: *Applied Physics Express* 5.10 (2012), p. 102401. DOI: 10.1143/APEX.5.102401. URL: http://apex.jsap.jp/link?APEX/5/102401/.

[109] Huidong Kim et al. "Improved absolute frequency measurement of the 171Yb optical lattice clock at KRISS relative to the SI second". In: *Japanese Journal of Applied Physics* 56.5 (2017), p. 050302.

[110] R. W. Fox et al. "A high stability optical frequency reference based on thermal calcium atoms". In: *2012 IEEE International Frequency Control Symposium Proceedings*. May 2012, pp. 1–3. DOI: 10.1109/FCS.2012.6243750.

[111] T. M. Fortier et al. "Generation of ultrastable microwaves via optical frequency division". In: *Nat. Photon.* 5 (7 July 2011), pp. 425–429. URL: http://dx.doi.org/10.1038/nphoton.2011.121.

[112] Scott A. Diddams, Leo Hollberg, and Vela Mbele. "Molecular fingerprinting with the resolved modes of a femtosecond laser frequency comb". In: *Nature* 445 (7128 2007), pp. 627–630. URL: http://dx.doi.org/10.1038/nature05524.

[113] Y. Y. Jiang et al. "Making optical atomic clocks more stable with 10-16-level laser stabilization". In: *Nat. Photon.* 5.3 (Mar. 2011), pp. 158–161. ISSN: 1749-4885. URL: http://dx.doi.org/10.1038/nphoton.2010.313.

[114] C. W. Hoyt et al. "Observation and Absolute Frequency Measurements of the $^1S_0$-$^3P_0$ Optical Clock Transition in Neutral Ytterbium". In: *Phys. Rev. Lett.* 95 (8 Aug. 2005), p. 083003. DOI: 10.1103/PhysRevLett.95.083003. URL: http://link.aps.org/doi/10.1103/PhysRevLett.95.083003.

[115] N. Hinkley. "An atomic clock for 10^{-18} timekeeping". PhD thesis. University of Colorado, 2016.

[116] J. L. Hall et al. "Optical heterodyne saturation spectroscopy". In: *Appl. Phys. Lett.* 39.9 (1981), pp. 680–682. DOI: 10.1063/1.92867. URL: http://link.aip.org/link/?APL/39/680/1.

[117] Jon H. Shirley. "Modulation transfer processes in optical heterodyne saturation spectroscopy". In: *Opt. Lett.* 7.11 (Nov. 1982), pp. 537–539. DOI: 10.1364/OL.7.000537. URL: http://ol.osa.org/abstract.cfm?URI=ol-7-11-537.

[118] D.C. Allan et al. *Photonic crystal fiber*. US Patent 6,243,522. June 2001. URL: https://www.google.com/patents/US6243522.

[119] Hidetoshi Katori et al. "Magic Wavelength to Make Optical Lattice Clocks Insensitive to Atomic Motion". In: *Phys. Rev. Lett.* 103 (15 Oct. 2009), p. 153004. DOI: 10.1103/PhysRevLett.103.153004. URL: https://link.aps.org/doi/10.1103/PhysRevLett.103.153004.

[120] V. A. Dzuba and A. Derevianko. "Dynamic polarizabilities and related properties of clock states of the ytterbium atom". In: *J. Phys. B: At. Mol. Opt. Phys.* 43.7 (2010).

[121] Sebastian Häfner et al. "8×10^{-17} fractional laser frequency instability with a long room-temperature cavity". In: *Opt. Lett.* 40.9 (May 2015), pp. 2112–2115. DOI: 10.1364/OL.40.002112. URL: http://ol.osa.org/abstract.cfm?URI=ol-40-9-2112.

[122] Masao Takamoto, Tetsushi Takano, and Hidetoshi Katori. "Frequency comparison of optical lattice clocks beyond the Dick limit". In: *Nat. Photon.* 5.5 (May 2011), pp. 288–292. ISSN: 1749-4885. URL: http://dx.doi.org/10.1038/nphoton.2011.34.

[123] M. Meunier et al. "Stability enhancement by joint phase measurements in a single cold atomic fountain". In: *Phys. Rev. A* 90 (6 Dec. 2014), p. 063633. DOI: 10.1103/PhysRevA.90.063633. URL: https://link.aps.org/doi/10.1103/PhysRevA.90.063633.

[124] T.L. Nicholson et al. "Systematic evaluation of an atomic clock at 2 [times] 10-18 total uncertainty". In: *Nat Commun* 6 (Apr. 2015), pp. –. URL: http://dx.doi.org/10.1038/ncomms7896.

[125] Ali Al-Masoudi et al. "Noise and instability of an optical lattice clock". In: *Phys. Rev. A* 92 (6 Dec. 2015), p. 063814. DOI: 10.1103/PhysRevA.92.063814. URL: https://link.aps.org/doi/10.1103/PhysRevA.92.063814.

This Ph.D. thesis has been typeset by means of the TEX-system facilities. The typesetting engine was pdfLATEX. The document class was `toptesi`, by Claudio Beccari, with option `tipotesi=scudo`. This class is available in every up-to-date and complete TEX-system installation.